

# **Investigating Graphene-Based Systems: Interaction Effects, Localization, and Finite-Temperature Dynamics**

Dissertation  
zur  
Erlangung des Doktorgrades (Dr. rer. nat.)  
der  
Mathematisch-Naturwissenschaftlichen Fakultät  
der  
Rheinischen Friedrich-Wilhelms-Universität Bonn

von  
**Lado Razmadze**  
aus  
Tiflis

Bonn, 27.01.2025

Angefertigt mit Genehmigung der Mathematisch-Naturwissenschaftlichen Fakultät der Rheinischen  
Friedrich-Wilhelms-Universität Bonn

Gutachter/Betreuer: Prof. Thomas Luu, Ph.D.  
Gutachter: Prof. Dr. Dr. h. c. Ulf-G. Meißner

Tag der Promotion: 19.02.2025  
Erscheinungsjahr: 2025

---

## Acknowledgements

---

I would like to express my deepest gratitude to my supervisor, Prof. Thomas Luu, Ph.D., for his invaluable guidance, support, and encouragement throughout the course of my thesis. His patience and insights have been instrumental in shaping my academic journey.

Moreover, I would like to thank Prof. Dr. Dr. h.c. Ulf-G. Meißner, for his support as my second supervisor.

I am also sincerely thankful to my friend, PD Dr. Akaki Rusetski, for providing me with the opportunity to embark on my academic path at the University of Bonn. His support has been a cornerstone of my progress.

Finally, I would like to extend my heartfelt appreciation to my friends and family for their unwavering support, encouragement, and understanding during my studies. Their belief in me has been a source of strength throughout this journey.



---

# Contents

---

<b>1</b>	<b>Introduction</b>	<b>3</b>
1.1	Graphene geometries	4
1.2	Hubbard Model	7
1.3	Thermal Field Theory	12
1.3.1	Time dependence	12
1.3.2	Propagator	13
1.3.3	Frequency propagator	14
1.3.4	Interaction picture	15
1.3.5	Correlator	16
1.3.6	Wick's theorem	17
1.3.7	Feynman Rules	17
1.3.8	Self-energy	18
1.3.9	Solving the quantization condition	21
1.4	Numerical Methods	21
1.4.1	Hybrid Monte Carlo	21
1.4.2	Leapfrog Integration	23
1.4.3	Fitting Correlators	23
<b>2</b>	<b>Topology and symmetry in carbon nanoribbons</b>	<b>27</b>
2.1	Introduction	29
2.1.1	Topology in condensed matter	29
2.2	Kitaev Chain	30
2.3	BCS-Hubbard Model	31
2.3.1	Hamiltonian	31
2.3.2	Composite fermions	31
2.4	Carbon Nanoribbons	32
2.4.1	Zigzag Nanoribbon(ZNR)	32
2.4.2	Armchair Nanoribbon(ANR)	33
2.5	Effective Hamiltonian	36
<b>3</b>	<b>Localization of electronic states in hybrid nanoribbons in the nonperturbative regime</b>	<b>37</b>
3.1	Introduction	39
3.2	Geometry of the periodic hybrid nanoribbon	40
3.3	QMC calculations of the Hubbard Model	43
3.3.1	Energy of the localized states	45

3.3.2	Wavefunction densities of the localized state	45
3.4	The symmetric-line limit	48
3.4.1	Ferromagnetic configuration	50
3.4.2	Antiferromagnetic configuration	52
3.4.3	Random configuration	52
3.5	Analogy with Domain-wall fermions	54
3.6	Conclusions	57
<b>4</b>	<b>Effective theory for graphene nanoribbons with junctions</b>	<b>59</b>
4.1	Introduction	61
4.2	Hybrids Ribbons and Junctions	64
4.3	Effective 1-D Tight-binding model	69
4.3.1	Formulation	69
4.3.2	Determination of the Low-Energy Constants	70
4.3.3	Application of our effective theory	71
4.3.4	Incorporating Interactions	72
4.3.5	Misaligned Hybrid Ribbons	75
4.4	Conclusions	77
<b>5</b>	<b>Hubbard interaction at finite <math>T</math> on a hexagonal lattice</b>	<b>79</b>
5.1	Introduction	81
5.1.1	System	81
5.2	Thermal Field Theory	83
5.3	Solution	84
5.4	Results	86
5.4.1	$T = 0$	86
5.4.2	$T \neq 0$	86
5.5	Summary and Outlook	87
<b>6</b>	<b>Conclusion</b>	<b>89</b>
<b>A</b>	<b>Useful information</b>	<b>93</b>
A.1	Commutator/Anticommutators	93
A.2	Matsubara sums	93
<b>B</b>	<b>Detailed calculations</b>	<b>95</b>
<b>C</b>	<b>Localization of electronic states in hybrid nanoribbons in the nonperturbative regime</b>	<b>103</b>
C.1	Extracting site densities from QMC simulations	103
<b>D</b>	<b>Hubbard interaction at finite <math>T</math> on a hexagonal lattice</b>	<b>107</b>
D.1	Results for $3 \times 3$ ribbons	107
	<b>Bibliography</b>	<b>109</b>

## List of publications

During the course of this thesis the following articles have been published:

- [1] **Topology and symmetry in carbon nanoribbons**, L. Razmadze, PoS **Regio2021** 031 (2022)
- [2] **\*Localization of electronic states in hybrid nanoribbons in the nonperturbative regime**  
T. Luu, U. Meißner and L. Razmadze, Phys. Rev. B **106**, 195422 (2022) [[arXiv:cond-mat/2204.02742](#)]
- [3] **\*Effective theory for graphene nanoribbons with junctions** J. Ostmeyer, L. Razmadze, E. Berkowitz, T. Luu and U. Meißner, Phys. Rev. B **109**, 195135 (2024) [[arXiv:cond-mat/2401.04715](#)]
- [4] **Hubbard interaction at finite  $T$  on a hexagonal lattice**, L. Razmadze and T. Luu, PoS **LATTICE2024** 071 (2024) [[arXiv:cond-mat/2411.03196](#)]

\* L.Razmadze is a significant contributor



---

## Introduction

---

Materials science, as an interdisciplinary field, plays an essential role in advancing scientific and technological innovation. The development of advanced materials—such as high-strength steel and long-lasting concrete—has enabled the construction of taller and more resilient structures. Yet, the 21st century presents new demands that drive innovation at the nanoscale. The evolution of semiconductor technology exemplifies this shift, having revolutionized modern life through profound technological transformations. Since the 1970s, the number of transistors on integrated circuits has doubled approximately every two years—a phenomenon known as Moore’s Law—demonstrating the relentless progress in materials science.

The trajectory of computing advancements has been closely intertwined with breakthroughs in materials science. Early computers relied on vacuum tubes, which were eventually replaced by silicon-based transistors and integrated circuits due to their superior efficiency and scalability. Silicon’s distinctive properties—such as its natural abundance, thermal stability, and tunable semiconductor behavior via doping—have made it the ideal backbone for modern electronics. However, as silicon-based systems near their physical and practical limitations, researchers are actively investigating alternative materials and paradigms to sustain innovation.

One of the most promising frontiers in this pursuit is quantum computing. Unlike classical computing systems, which process binary digits, quantum computers leverage quantum states to encode information in qubits. In this framework, computation involves initializing quantum states, evolving them according to quantum mechanical principles, and measuring the resulting states. By carefully designing and sequencing these transformations, quantum computers can address complex computational problems, such as cryptographic challenges and chemical simulations, that are intractable for classical computers.

Despite significant theoretical advancements, building practical quantum computers remains a formidable scientific challenge. A central obstacle is the identification of materials capable of maintaining quantum coherence long enough to perform meaningful computations while remaining controllable enough to implement quantum gates. Qubits are highly sensitive to environmental factors, such as thermal fluctuations and material imperfections, which lead to decoherence. Among the candidate materials, graphene stands out due to its exceptional electronic and structural properties. This two-dimensional carbon lattice can adopt diverse geometries—from flat sheets to ribbons and complex three-dimensional structures—each offering unique advantages for implementing qubits. Graphene’s high electron mobility and low spin-orbit coupling make it particularly promising for

preserving quantum coherence. Moreover, its compatibility with existing semiconductor fabrication techniques presents a practical pathway for integrating quantum components into existing technological ecosystems. However, significant challenges remain, including extending quantum coherence times and developing precise methods to manipulate quantum states in graphene-based architectures.

In this thesis, I investigate the electronic behavior of low-dimensional nanoribbons and graphene sheets to advance our understanding of their potential applications in quantum technologies, particularly quantum computing. Specifically, this research examines the localization of edge states in junction ribbons, the temperature dependence of quasi-particle energies, and the resilience of quantum states under thermal and interaction perturbations within Hubbard-type models. This study is inherently exploratory, with no immediate practical applications, emphasizing the necessity for continued theoretical and experimental research. The findings contribute to the broader goal of identifying physical systems capable of supporting coherent quantum states or exhibiting other valuable quantum properties. The subsequent sections provide the necessary theoretical background and formal framework for analyzing these materials, setting the stage for assessing their potential role in future quantum technologies.

## 1.1 Graphene geometries

The physical systems of interest are graphene sheets, ribbons, and junction ribbons where two or more different ribbons are joined together. Graphene is a bipartite lattice, meaning it is composed of two identical triangular sublattices, commonly referred to as **A** and **B**. Alternatively, it can be described as a tessellation by unit cells, each containing two sites.

### Sheets

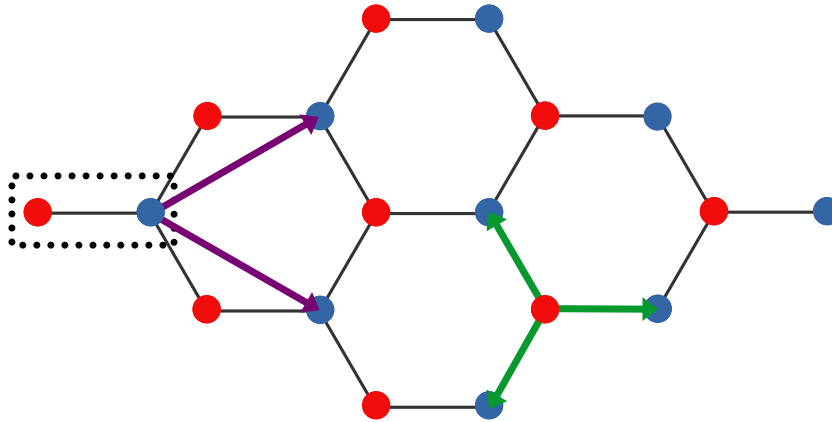


Figure 1.1:  $3 \times 3$  Graphene sheet. Graphene forms a hexagonal bipartite lattice with two sites **A** and **B** in each unit cell (dotted rectangle), located at  $\xi_A = (0, 0)$  and  $\xi_B = (1, 0)$  respectively. The lattice translation vectors, shown in purple, are  $\mathbf{a}_{1,2} = (3/2, \pm\sqrt{3}/2)$ , and the nearest-neighbor vectors are marked by green arrows.

Graphene sheets are the simplest of these geometries characterized by translation vectors:

$$\mathbf{a}_{1,2} = a \left( \frac{3}{2} \pm \frac{\sqrt{3}}{2} \right). \quad (1.1)$$

Here  $a$  is the *lattice constant*. Notice that these vectors are not orthogonal:

$$\mathbf{a}_i \cdot \mathbf{a}_i = \sqrt{3}a, \quad \mathbf{a}_1 \cdot \mathbf{a}_2 = \frac{\sqrt{3}}{2}a. \quad (1.2)$$

Translation vectors specify the location of the unit cells. Each unit cell contains 2 sites, **A/B**, which are located at:

$$\xi_A = (0 \ 0) \quad \text{and} \quad \xi_B = (1 \ 0). \quad (1.3)$$

inside relative to the cell. Graphene sheets are classified by two numbers  $L_x \times L_y$ , where  $L_x$  is the number of unit cells in the direction of  $\mathbf{a}_1$  and  $L_y$  in the direction of  $\mathbf{a}_2$ . In [Figure 1.1](#) we show the  $3 \times 3$  graphene system. For mathematical simplicity periodic boundary conditions are assumed in both directions and only in the *thermodynamic limit*, as  $L_x, L_y \rightarrow \infty$  is the system meant to describe a physical sheet. The reciprocal vectors satisfy  $\mathbf{b}_i \cdot \mathbf{a}_j = 2\pi\delta_{ij}$ . It is straightforward to see that this is satisfied by

$$\mathbf{b}_{1,2} = \frac{2\pi}{a} \left( \frac{1}{3} \pm \frac{1}{3\sqrt{3}} \right). \quad (1.4)$$

The vectors  $\mathbf{b}_{1,2}$  span the reciprocal space. The unit cell in the reciprocal space defines the *Brillouin Zone (BZ)*. Graphene has a well defined BZ. Size of the BZ is the number of momentum points  $\Lambda = L_x L_y$ . In [Figure 1.2](#) the BZ for several graphene geometries are given. Within the graphene BZ

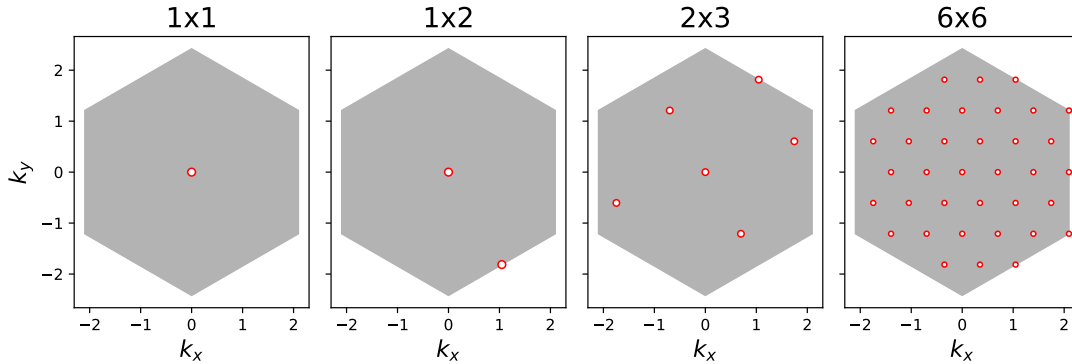


Figure 1.2: Brillouin zones for various lattice sizes in graphene. As lattice size increases, momentum points increasingly populate the hexagonal Brillouin zone. Of particular importance are the momentum points at the center ( $\Gamma$ -point), at the midpoint of the edges ( $M$ -point), and at the vertices ( $K$ -points). In the thermodynamic limit when  $L_x, L_y \rightarrow \infty$ , the BZ forms a hexagon.

there are special points of ‘high-symmetry’: the center of the hexagon -  $\Gamma$ , the midpoint of the edges -  $M$  and the vertices of the hexagon -  $K = \left( \pm \frac{2\pi}{3}, \frac{2\pi}{3\sqrt{3}} \right)$ , also known as *Dirac points* where, under the tight-binding approximation (to be discussed later), the dispersion relation vanishes.

## Carbon nanoribbons

Ribbons possess a similar geometry to the sheets as they are also comprised of two identical sublattices, but they differ based on their edge geometry. In Figure 1.3 two most common types of ribbons are given, armchair Figure 1.3(a) and zigzag Figure 1.3(b). The unit cell is shown by two vertical dashed lines. The width of the ribbon, i.e. number of sites across the ribbon is denoted by  $N$ , whereas the length, i.e. the number of unit cells is taken to be  $L$ . Periodic boundary conditions are assumed along the  $\hat{y}$ -axis and open boundaries are taken across the ribbon in the direction of  $\hat{x}$ -axis. Because we no longer have translational symmetry across the ribbon its BZ is 1D as opposed to the sheets. Armchair

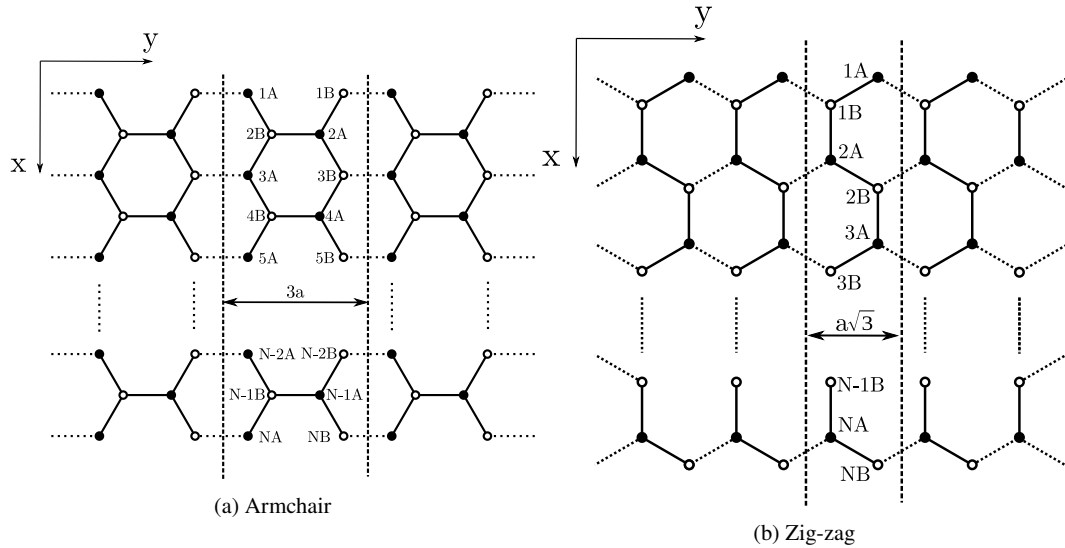


Figure 1.3: Nanoribbon lattices. Unit cell is shown by two vertical dashed lines. Width of the ribbon is given by  $N$ . Length of the ribbon is taken to be  $L$ . Periodic boundary conditions are assumed along  $\hat{y}$ -axis and open boundaries are taken across the  $\hat{x}$ -axis.

ribbons behave as semi-metals at widths  $N = 3m + 2 \quad \forall m \in \mathbb{Z}_+$  and like insulators otherwise. Zigzag ribbons on the other hand behave like semi-metals irrespective of the width.

## Hybrid ribbons

Hybrid ribbons – also known as junction ribbons – are formed by joining any number of ribbons with different widths and geometries together. For this task, the focus is on armchair ribbons, particularly those with widths differing by 2. These structures can either consist of two infinitely long ribbons or a chain of shorter ribbons with alternating widths. The lattices are classified based on the widths and lengths of the two constituent ribbons. As illustrated in Figure 1.4, the junction ribbon under consideration consists of two armchair configurations with widths of 7 and 9 and corresponding lengths of 3 and 5, respectively.

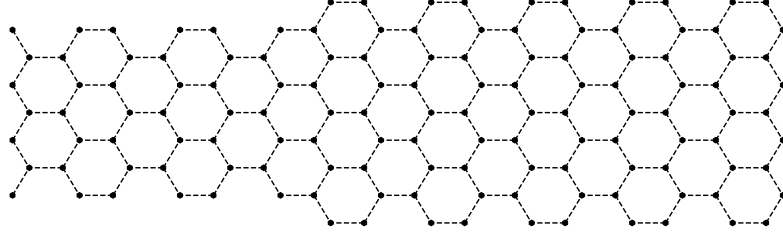


Figure 1.4: Junction ribbon of two armchairs with widths of 7 and 9 and lengths of 3 and 5. Periodic boundary conditions are assumed along the ribbons.

## 1.2 Hubbard Model

The simple tight-binding Hamiltonian  $H$  with Hubbard interaction term is defined at half-filling with hopping strength  $t$ , chemical potential  $\mu$ , and Hubbard interaction strength  $U$ , as:

$$H = -t \sum_{\langle x,y \rangle s} (c_{xs}^\dagger c_{ys} + H.c.) - \frac{U}{2} \sum_x (n_{x\uparrow} - n_{x\downarrow})^2 - \mu \sum_{xs} n_{xs}. \quad (1.5)$$

Here,  $\langle x, y \rangle$  means a sum over nearest neighbors,  $c^\dagger/c$  is the fermion creation/annihilation operator, and  $n_x = c_x^\dagger c_x$  is the corresponding number operator. Operators satisfy the *anti-commutation* relation:

$$\{c_{xs}, c_{ys'}^\dagger\} = \delta_{xy} \delta_{ss'}. \quad (1.6)$$

To expand the square, keep in mind that we can only have 0 or 1 fermion in the same state, meaning  $n_x$  only has eigenvalues 0 and 1; therefore,  $n_x^2 = n_x$ . We can therefore write:

$$\begin{aligned} H &= -t \sum_{\langle x,y \rangle s} (c_{xs}^\dagger c_{ys} + H.c.) - \frac{U}{2} \sum_{xs} n_{xs}^2 + U \sum_{xs} n_{x\uparrow} n_{x\downarrow} - \mu \sum_{xs} n_{xs} \\ &= -t \sum_{\langle x,y \rangle s} (c_{xs}^\dagger c_{ys} + H.c.) - \left( \mu + \frac{U}{2} \right) \sum_{xs} n_{xs} + U \sum_x c_{x\uparrow}^\dagger c_{x\uparrow} c_{x\downarrow}^\dagger c_{x\downarrow} \\ &\equiv H_0 + H_1 + H_2. \end{aligned}$$

We can also write the Hamiltonian explicitly using A/B sublattices:

$$\begin{aligned} H &= -t \sum_{xs} c_{xAs}^\dagger (c_{xBs} + c_{x-a_1Bs} + c_{x-a_2Bs}) + H.c. \\ &\quad - \left( \mu + \frac{U}{2} \right) \sum_{xs} n_{xAs} + n_{xBs} \\ &\quad + U \sum_x c_{xA\uparrow}^\dagger c_{xA\downarrow}^\dagger c_{xA\downarrow} c_{xA\uparrow} + c_{xB\uparrow}^\dagger c_{xB\downarrow}^\dagger c_{xB\downarrow} c_{xB\uparrow}. \end{aligned}$$

Here,  $x$  goes over a single sublattice. We have also normal-ordered the operators (i.e., all annihilation operators are ‘to the right’).

## Diagonalization

In order to diagonalize the Hamiltonian, we introduce the Fourier transform as a sum over the momenta in the BZ:

$$c_{x\lambda s} = \frac{1}{\sqrt{\Lambda}} \sum_k e^{ik(x+\xi_\lambda)} c_{k\lambda s}, \quad (1.7)$$

$\Lambda$  being the size of the Brillouin zone. Insert this back into the expression for  $H_0$ :

$$\begin{aligned} H_0 &= -\frac{1}{\Lambda} \sum_{xs} \sum_{kk'} e^{i(k-k')x} (e^{ik\xi_B} + e^{ik(-a_1+\xi_B)} + e^{ik(-a_2+\xi_B)}) c_{k'As}^\dagger c_{kB_s} + H.c. \\ &= -\sum_s \sum_{kk'} \delta_{kk'} f(k) c_{k'As}^\dagger c_{kB_s} + H.c. \\ &= -\sum_{ks} f(k) c_{kAs}^\dagger c_{kB_s} + H.c. \\ &= \sum_{ks} \begin{pmatrix} c_{kAs}^\dagger & c_{kB_s}^\dagger \end{pmatrix} \begin{pmatrix} 0 & -f(k) \\ -f^*(k) & 0 \end{pmatrix} \begin{pmatrix} c_{kAs} \\ c_{kB_s} \end{pmatrix}, \end{aligned}$$

where we have defined:

$$f(k) = \sum_{i=1}^3 e^{ika_i} = e^{ik_x} + 2e^{-ik_x/2} \cos(\sqrt{3}k_y/2). \quad (1.8)$$

To continue we diagonalize the matrix in sublattice space as

$$0 = \begin{vmatrix} -\mathcal{E} & f(k) \\ f^*(k) & -\mathcal{E} \end{vmatrix} = \mathcal{E}^2 - |f(k)|^2,$$

resulting in eigenvalues  $\mathcal{E}_k^\sigma = \sigma \mathcal{E}_k = \sigma |f(k)|$  with  $\sigma = \pm 1$ . Eigenvectors are found by

$$\begin{pmatrix} -\sigma |f(k)| & -f(k) \\ -f^*(k) & -\sigma |f(k)| \end{pmatrix} \begin{pmatrix} \alpha \\ \beta \end{pmatrix} = 0 \quad \implies \quad \beta = -\sigma e^{-i\theta_k} \alpha,$$

where

$$e^{i\theta_k} = \frac{f(k)}{|f(k)|}. \quad (1.9)$$

After normalizing we arrive at

$$\phi_{k\sigma s} = \frac{1}{\sqrt{2}} \begin{pmatrix} 1 \\ -\sigma e^{-i\theta_k} \end{pmatrix} = \frac{1}{\sqrt{2}} (c_{kAs} - \sigma e^{-i\theta_k} c_{kB_s}). \quad (1.10)$$

One can easily see that anti-commutation is preserved

$$\begin{aligned}
 \{\phi_{k\sigma s}, \phi_{k'\sigma's'}^\dagger\} &= \frac{1}{2}\{c_{kAs}, c_{k'As'}^\dagger\} + \frac{\sigma\sigma'e^{-i(\theta_{k'}-\theta_k)}}{2}\{c_{kB_s}, c_{k'B_s'}^\dagger\} \\
 &= \frac{1+\sigma\sigma'}{2}\delta_{kk'}\delta_{ss'} \\
 &= \delta_{\sigma\sigma'}\delta_{kk'}\delta_{ss'}.
 \end{aligned} \tag{1.11}$$

Note that for  $\sigma, \sigma' \in \{\pm 1\}$ ,  $1 + \sigma\sigma' = 0$  if  $\sigma = \sigma'$  and zero otherwise which can be written using a Kronecker  $\delta$ . After diagonalizing we can write

$$\begin{aligned}
 H_0 &= \sum_{ks} \begin{pmatrix} c_{kAs}^\dagger & c_{kB_s}^\dagger \end{pmatrix} \begin{pmatrix} 0 & -f(k) \\ -f^*(k) & 0 \end{pmatrix} \begin{pmatrix} c_{kAs} \\ c_{kB_s} \end{pmatrix} \\
 &= \sum_{ks} \begin{pmatrix} \phi_{k+s}^\dagger & \phi_{k-s}^\dagger \end{pmatrix} \begin{pmatrix} \mathcal{E}_k^+ & 0 \\ 0 & \mathcal{E}_k^- \end{pmatrix} \begin{pmatrix} \phi_{k+s} \\ \phi_{k-s} \end{pmatrix} \\
 &= \sum_{k\sigma s} \mathcal{E}_k^\sigma \phi_{k\sigma s}^\dagger \phi_{k\sigma s}.
 \end{aligned}$$

The chemical potential term is also diagonal in  $\phi$  basis. First note that

$$\begin{aligned}
 H_1 &= -\left(\mu + \frac{U}{2}\right) \sum_{xs} c_{xA_s}^\dagger c_{xA_s} + c_{xB_s}^\dagger c_{xB_s} \\
 &= -\left(\mu + \frac{U}{2}\right) \sum_{xs} \frac{1}{\Lambda} \sum_{kk'} e^{-ik'x} e^{ikx} \left( c_{k'As}^\dagger c_{kAs} + e^{-ik'\xi_A} e^{ik\xi_B} c_{k'B_s}^\dagger c_{kB_s} \right) \\
 &= -\left(\mu + \frac{U}{2}\right) \sum_s \sum_{kk'} \delta_{kk'} \left( c_{k'As}^\dagger c_{kAs} + e^{-ik'\xi_B} e^{ik\xi_B} c_{k'B_s}^\dagger c_{kB_s} \right) \\
 &= -\left(\mu + \frac{U}{2}\right) \sum_{ks} c_{kAs}^\dagger c_{kAs} + c_{kB_s}^\dagger c_{kB_s}.
 \end{aligned}$$

Now we invert the definition of  $\phi_{k\sigma s}$

$$c_{kAs} = \frac{1}{\sqrt{2}}(\phi_{k+s} + \phi_{k-s}) = \frac{1}{\sqrt{2}} \sum_{\sigma} \phi_{k\sigma s}, \tag{1.12}$$

$$c_{kB_s} = -\frac{e^{i\theta_k}}{\sqrt{2}}(\phi_{k+s} - \phi_{k-s}) = -\frac{e^{i\theta_k}}{\sqrt{2}} \sum_{\sigma'} \sigma' \phi_{k\sigma's}. \tag{1.13}$$

Putting it all together gives

$$\begin{aligned}
 H_1 &= -\left(\mu + \frac{U}{2}\right) \frac{1}{2} \sum_{k\sigma\sigma's} \phi_{k\sigma s}^\dagger \phi_{k\sigma's} + \sigma\sigma' \phi_{k\sigma s}^\dagger \phi_{k\sigma's} \\
 &= -\left(\mu + \frac{U}{2}\right) \sum_{k\sigma\sigma's} \frac{1+\sigma\sigma'}{2} \phi_{k\sigma s}^\dagger \phi_{k\sigma's} \\
 &= -\left(\mu + \frac{U}{2}\right) \sum_{k\sigma\sigma's} \delta_{\sigma\sigma'} \phi_{k\sigma s}^\dagger \phi_{k\sigma's} \\
 &= -\left(\mu + \frac{U}{2}\right) \sum_{k\sigma s} \phi_{k\sigma s}^\dagger \phi_{k\sigma s}.
 \end{aligned}$$

In order to express quartic term in  $\phi$  basis we first need to Fourier transform it

$$\begin{aligned}
 H_2 &= U \sum_x c_{xA\uparrow}^\dagger c_{xA\downarrow}^\dagger c_{xA\downarrow} c_{xA\uparrow} + c_{xB\uparrow}^\dagger c_{xB\downarrow}^\dagger c_{xB\downarrow} c_{xB\uparrow} \\
 &= \frac{U}{\Lambda^2} \sum_x \sum_{k'l'kl} e^{-i(k'+l'-k-l)x} \left( c_{k'A\uparrow}^\dagger c_{l'A\downarrow}^\dagger c_{kA\downarrow} c_{lA\uparrow} + e^{-i(k'+l'-k-l)a_1} c_{k'B\uparrow}^\dagger c_{l'B\downarrow}^\dagger c_{kB\downarrow} c_{lB\uparrow} \right).
 \end{aligned}$$

We observe that

$$\frac{1}{\Lambda} \sum_x e^{-i(k'+l'-k-l)x} = \begin{cases} 1 & k' + l' - k - l = m\mathbf{G}_1 + n\mathbf{G}_2, \quad m, n \in \mathbb{Z} \\ 0 & \text{otherwise} \end{cases}.$$

In order to not get overwhelmed by notation we will use  $\delta_{k'+l',k+l}$  and implicitly assume the equality to be modulo the BZ, i.e.  $k' + l' - k - l = m\mathbf{G}_1 + n\mathbf{G}_2$ . With this we get

$$\begin{aligned}
 H_2 &= \frac{U}{\Lambda} \sum_{k'l'kl} \delta_{k'+l',k+l} \left( c_{k'A\uparrow}^\dagger c_{l'A\downarrow}^\dagger c_{kA\downarrow} c_{lA\uparrow} + e^{-i(m\mathbf{G}_1+n\mathbf{G}_2)a_1} c_{k'B\uparrow}^\dagger c_{l'B\downarrow}^\dagger c_{kB\downarrow} c_{lB\uparrow} \right) \\
 &= \frac{U}{\Lambda} \sum_{k'l'kl} \delta_{k'+l',k+l} \left( c_{k'A\uparrow}^\dagger c_{l'A\downarrow}^\dagger c_{kA\downarrow} c_{lA\uparrow} + e^{-i\frac{2\pi}{3}(m+n)} c_{k'B\uparrow}^\dagger c_{l'B\downarrow}^\dagger c_{kB\downarrow} c_{lB\uparrow} \right).
 \end{aligned}$$

To make the calculations simpler we can write the relations between  $a, b$  and  $\phi, \varphi$  as follows:

$$\begin{aligned}
 c_{kAs} &= \frac{1}{\sqrt{2}} \sum_{\sigma} \phi_{l\sigma s} & c_{k'As}^\dagger &= \frac{1}{\sqrt{2}} \sum_{\sigma'} \phi_{l'\sigma's}^\dagger \\
 c_{lBs} &= -\frac{e^{i\theta_l}}{\sqrt{2}} \sum_{\sigma} \sigma \phi_{l\sigma s} & c_{l'Bs}^\dagger &= -\frac{e^{-i\theta_{l'}}}{\sqrt{2}} \sum_{\sigma'} \sigma' \phi_{l'\sigma's}^\dagger.
 \end{aligned} \tag{1.14}$$

The first term gives

$$\frac{U}{4\Lambda} \sum_{k'l'kl} \delta_{k'+l',k+l} c_{k'A\uparrow}^\dagger c_{l'A\downarrow}^\dagger c_{kA\downarrow} c_{lA\uparrow} = \frac{U}{\Lambda} \sum_{\substack{k',l',k,l \\ \rho',\sigma',\rho,\sigma'}} \delta_{k'+l',k+l} \phi_{k'\rho'\uparrow}^\dagger \phi_{l'\sigma'\downarrow}^\dagger \phi_{k\rho\downarrow} \phi_{l\sigma\uparrow},$$

While the second results in

$$\begin{aligned} & \frac{U}{\Lambda} \sum_{k',l',k,l} \delta_{k'+l',k+l} e^{-i\frac{2\pi}{3}(m+n)} c_{k'B\uparrow}^\dagger c_{l'B\downarrow}^\dagger c_{kB\downarrow} c_{lB\uparrow} \\ &= \frac{U}{4\Lambda} \sum_{\substack{k',l',k,l \\ \rho',\sigma',\rho,\sigma'}} \delta_{k'+l',k+l} \rho' \sigma' \rho \sigma e^{-i\frac{2\pi}{3}(m+n)} e^{i(\theta_k - \theta_{k'} + \theta_l - \theta_{l'})} \phi_{k'\rho'\uparrow}^\dagger \phi_{l'\sigma'\downarrow}^\dagger \phi_{k\rho\downarrow} \phi_{l\sigma\uparrow}. \end{aligned}$$

We now introduce the following notation

$$\begin{aligned} \mathbf{k} &= (k, \rho), & \mathbf{k}' &= (k', \rho'), \\ \mathbf{l} &= (l, \sigma), & \mathbf{l}' &= (l', \sigma'). \end{aligned}$$

Combining the two gives the final expression for  $H_2$

$$H_2 = \frac{U}{4\Lambda} \sum_{k'l'kl} \delta_{k'+l',k+l} \left( 1 + \rho' \sigma' \rho \sigma e^{i(\theta_k - \theta_{k'} + \theta_l - \theta_{l'})} e^{-i\frac{2\pi}{3}(m+n)} \right) \phi_{k'\uparrow}^\dagger \phi_{l'\downarrow}^\dagger \phi_{k\downarrow} \phi_{l\uparrow}. \quad (1.15)$$

Combining (1.12), (1.14) and (1.15) results in the following expression of the Hamiltonian:

$$H = \sum_{ks} \left( \mathcal{E}_{\mathbf{k}} - \mu - \frac{U}{2} \right) \phi_{ks}^\dagger \phi_{ks} + \sum_{k'l'kl} V_{k'l'kl} \phi_{k'\uparrow}^\dagger \phi_{l'\downarrow}^\dagger \phi_{k\downarrow} \phi_{l\uparrow}, \quad (1.16)$$

where we have defined  $\mathcal{E}_{\mathbf{k}} \stackrel{\dagger}{=} \mathcal{E}_k^\rho$  as well as

$$V_{k'l'kl} = \frac{U}{4\Lambda} \delta_{k'+l',k+l} \left( 1 + \rho' \sigma' \rho \sigma e^{i(\theta_k - \theta_{k'} + \theta_l - \theta_{l'})} e^{-i\frac{2\pi}{3}(m+n)} \right). \quad (1.17)$$

From this point on in the manuscript, in order to improve readability we will use bold multi-index notation  $\mathbf{k} = (k, \rho)$  wherever possible, unless sublattice indices are explicitly required.

### Canonical transformation

We define the *Fermi Energy*  $\mathcal{E}_F$  such that all states with  $\mathcal{E}_{\mathbf{k}} \leq \mathcal{E}_F$  are filled [5].

$$\phi_{k\rho s} = a_{ks} \theta(\mathcal{E}_k^\rho - \mathcal{E}_F) + b_{-ks}^\dagger \theta(\mathcal{E}_F - \mathcal{E}_k^\rho), \quad (1.18)$$

where

$$\theta(x) = \begin{cases} 1 & x > 0 \\ \frac{1}{2} & x = 0 \\ 0 & x < 0 \end{cases}. \quad (1.19)$$

The  $x = 0$  behavior is defined in a way that is consistent with  $\lim_{\beta \rightarrow \infty} n_{\mathbf{k}}$ . Now, in our case  $\mathcal{E}_F = 0$  which reduces the expression to

$$\phi_{k\rho s} = a_{ks} \theta(\mathcal{E}_k^\rho) + b_{-ks}^\dagger \theta(-\mathcal{E}_k^\rho) = \begin{cases} a_{ks} & \rho = + \text{ "particle" } \\ b_{-ks}^\dagger & \rho = - \text{ "hole" } \end{cases}. \quad (1.20)$$

One can see that since  $\forall k \mathcal{E}_k > 0$

$$\theta(\mathcal{E}_k^\rho) = \theta(\rho \mathcal{E}_k) = \theta(\rho).$$

We can do a quick check and see that the anti-commutation relation is preserved

$$\begin{aligned} \{\phi_{k\rho s}, \phi_{k'\rho's'}^\dagger\} &= \{a_{ks}, a_{k's'}^\dagger\}\theta(\rho)\delta_{\rho\rho'} + \{b_{-ks}^\dagger, b_{-k's'}\}\theta(-\rho)\delta_{\rho\rho'} \\ &= \delta_{kk'}\delta_{ss'}\theta(\rho)\delta_{\rho\rho'} + \delta_{kk'}\delta_{ss'}\theta(-\rho)\delta_{\rho\rho'} \\ &= \delta_{kk'}\delta_{ss'}\delta_{\rho\rho'}(\theta(\rho) + \theta(-\rho)) \\ &= \delta_{kk'}\delta_{ss'}\delta_{\rho\rho'}. \end{aligned}$$

The above discussion is meant to illustrate the meaning behind the quantum number  $\rho$ . In the following manuscript we will not perform the transformation and instead will work in the  $\phi$ -basis, while referring to  $\phi_{k,+s}$  states as particles and  $\phi_{k,-s}$  as holes.

## 1.3 Thermal Field Theory

### 1.3.1 Time dependence

From [5] the time evolution of an operator in free theory i.e.  $U = 0$  is

$$O(\tau) = e^{\tau H_0} O e^{-\tau H_0} = O + \tau [H_0, O] + \frac{\tau^2}{2!} [H_0 [H_0, O]] + \dots \quad (1.21)$$

To apply this to  $\phi_{k_s}$  we first need  $[H_0, \phi_{k_s}]$ :

$$\begin{aligned} [H_0, \phi_{k_s}] &= \sum_{k's'} (\mathcal{E}_{k'} - \mu) [\phi_{k's'}^\dagger \phi_{k's'}, \phi_{k_s}] \\ &= - \sum_{k's'} (\mathcal{E}_{k'} - \mu) \{\phi_{k's'}^\dagger, \phi_{k_s}\} \phi_{k's'} \\ &= - \sum_{k's'} (\mathcal{E}_{k'} - \mu) \delta_{kk'} \delta_{ss'} \phi_{k's'} \\ &= -(\mathcal{E}_k - \mu) \phi_{k_s}. \end{aligned} \quad (1.22)$$

Similarly

$$[H_0, \phi_{k_s}^\dagger] = (\mathcal{E}_k - \mu) \phi_{k_s}^\dagger.$$

Which gives

$$\phi_{k_s}(\tau) = \phi_{k_s} - \tau(\mathcal{E}_k - \mu)\phi_{k_s} + \frac{\tau^2(\mathcal{E}_k - \mu)^2}{2!}\phi_{k_s} + \dots = e^{-\tau(\mathcal{E}_k - \mu)} \phi_{k_s}, \quad (1.23)$$

and

$$\phi_{k_s}^\dagger(\tau) = \phi_{k_s}^\dagger + \tau(\mathcal{E}_k - \mu)\phi_{k_s}^\dagger + \frac{\tau^2(\mathcal{E}_k - \mu)^2}{2!}\phi_{k_s}^\dagger + \dots = e^{\tau(\mathcal{E}_k - \mu)} \phi_{k_s}^\dagger. \quad (1.24)$$

### 1.3.2 Propagator

The free propagator is defined as

$$G_{\mathbf{k}s}^0(\tau_1, \tau_2) = -Z_0^{-1} \text{Tr} \left[ e^{-\beta H_0} T_\tau [\phi_{\mathbf{k}s}(\tau_1) \phi_{\mathbf{k}s}^\dagger(\tau_2)] \right], \quad (1.25)$$

with

$$Z_0 = \text{Tr} \left[ e^{-\beta H_0} \right], \quad (1.26)$$

and  $T_\tau$  is a *time ordering* operator. It arranges  $\tau$ 's in decreasing order from left to right and multiplies the result by parity of the rearrangement. It is important to note that the propagator only depends on  $\tau = \tau_1 - \tau_2$ . We can easily show this. First assume that  $\tau_1 > \tau_2$

$$\begin{aligned} G_{\mathbf{k}s}^0(\tau_1, \tau_2) &= -Z_0^{-1} \text{Tr} \left[ e^{-\beta H_0} \phi_{\mathbf{k}s}(\tau_1) \phi_{\mathbf{k}s}^\dagger(\tau_2) \right] \\ &= -Z_0^{-1} \text{Tr} \left[ e^{-\beta H_0} e^{\tau_1 H_0} \phi_{\mathbf{k}s} e^{(-\tau_1 + \tau_2) H_0} \phi_{\mathbf{k}s}^\dagger e^{-\tau_2 H_0} \right] \\ &= -Z_0^{-1} \text{Tr} \left[ e^{-\beta H_0} \phi_{\mathbf{k}s}(\tau_1 - \tau_2) \phi_{\mathbf{k}s}^\dagger \right]. \end{aligned}$$

In the case when  $\tau_2 > \tau_1$

$$\begin{aligned} G_{\mathbf{k}s}^0(\tau_1, \tau_2) &= Z_0^{-1} \text{Tr} \left[ e^{-\beta H_0} \phi_{\mathbf{k}s}^\dagger(\tau_2) \phi_{\mathbf{k}s}(\tau_1) \right] \\ &= Z_0^{-1} \text{Tr} \left[ e^{-\beta H_0} \phi_{\mathbf{k}s}^\dagger \phi_{\mathbf{k}s}(\tau_1 - \tau_2) \right]. \end{aligned}$$

So we can define

$$G_{\mathbf{k}s}^0(\tau) = -Z_0^{-1} \text{Tr} \left[ e^{-\beta H_0} T_\tau [\phi_{\mathbf{k}s}(\tau) \phi_{\mathbf{k}s}^\dagger] \right]. \quad (1.27)$$

We also define  $G_{\mathbf{k}s}^0(0^-) \stackrel{!}{=} n_{\mathbf{k}}$ . Using [Equation 1.11](#), [Equation 1.21](#), [Equation 1.23](#), as well as the cyclic property of the trace we write

$$\begin{aligned} n_{\mathbf{k}} &= Z_0^{-1} \text{Tr} \left[ e^{-\beta H_0} \phi_{\mathbf{k}s}^\dagger \phi_{\mathbf{k}s} \right] \\ &= Z_0^{-1} \text{Tr} \left[ e^{-\beta H_0} \phi_{\mathbf{k}s}^\dagger e^{-\beta H_0} e^{\beta H_0} \phi_{\mathbf{k}s} \right] \\ &= Z_0^{-1} \text{Tr} \left[ e^{-\beta H_0} \phi_{\mathbf{k}s} \phi_{\mathbf{k}s}^\dagger \right] e^{-\beta(\mathcal{E}_{\mathbf{k}} - \mu)} \\ &= Z_0^{-1} \text{Tr} \left[ e^{-\beta H_0} (1 - \phi_{\mathbf{k}s}^\dagger \phi_{\mathbf{k}s}) \right] e^{-\beta(\mathcal{E}_{\mathbf{k}} - \mu)} \\ &= (1 - n_{\mathbf{k}}) e^{-\beta(\mathcal{E}_{\mathbf{k}} - \mu)}, \end{aligned}$$

which gives a familiar *Fermi-Dirac distribution*

$$n_{\mathbf{k}} = \frac{1}{e^{\beta(\mathcal{E}_{\mathbf{k}} - \mu)} + 1}. \quad (1.28)$$

Now the explicit time-dependent propagator becomes

$$G_{ks}^0(\tau) = e^{-\tau(\mathcal{E}_k - \mu)} \begin{cases} -(1 - n_k) & \tau > 0 \\ n_k & \tau \leq 0 \end{cases}. \quad (1.29)$$

One can also see that the propagator is anti-periodic

$$\begin{aligned} G_{ks}^0(-\beta < \tau < 0) &= e^{-\tau(\mathcal{E}_k - \mu)} n_k \\ &= e^{-\tau(\mathcal{E}_k - \mu)} (1 - n_k) e^{-\beta \mathcal{E}_k} \\ &= e^{-(\tau + \beta)(\mathcal{E}_k - \mu)} (1 - n_k) \\ &= -G_{ks}^0(0 < \tau + \beta < \beta), \end{aligned}$$

which results in

$$G_{ks}^0(\tau) = -G_{ks}^0(\tau + \beta). \quad (1.30)$$

### 1.3.3 Frequency propagator

We define the Fourier transform in  $\tau$  as

$$\tilde{G}_{ks}^0(\omega) = \frac{1}{2} \int_{-\beta}^{\beta} d\tau G_{ks}^0(\tau) e^{i\omega\tau}, \quad (1.31)$$

with  $\omega = \frac{\pi}{\beta}n$ . A very neat simplification follows when we use the periodicity property of the propagator.

$$\begin{aligned} \tilde{G}_{ks}^0(\omega) &= \frac{1}{2} \int_{-\beta}^{\beta} d\tau G_{ks}^0(\tau) e^{i\omega\tau} \\ &= \frac{1}{2} \int_0^{\beta} d\tau G_{ks}^0(\tau) e^{i\omega\tau} + \frac{1}{2} \int_{-\beta}^0 d\tau G_{ks}^0(\tau) e^{i\omega\tau} \\ &= \frac{1}{2} \int_0^{\beta} d\tau G_{ks}^0(\tau) e^{i\omega\tau} + e^{i\omega\beta} \frac{1}{2} \int_0^{\beta} d\tau G_{ks}^0(\tau + \beta) e^{i\omega\tau} \\ &= \frac{1 - e^{i\omega\beta}}{2} \int_0^{\beta} d\tau G_{ks}^0(\tau) e^{i\omega\tau}. \end{aligned}$$

Now

$$\frac{1 - e^{i\omega\beta}}{2} = \begin{cases} 1 & \omega = \frac{\pi}{\beta}(2n + 1) \\ 0 & \omega = \frac{\pi}{\beta}2n \end{cases}.$$

So we can rewrite

$$\tilde{G}_{ks}^0(\omega) = \int_0^{\beta} d\tau G_{ks}^0(\tau) e^{i\omega\tau}, \quad \omega = \frac{\pi}{\beta}(2n + 1). \quad (1.32)$$

Similarly an inverse transform is defined as the *Matsubara sum*

$$G_{ks}^0(\tau) = \frac{1}{\beta} \sum_{\omega} \tilde{G}_{ks}^0(\omega) e^{-i\omega\tau}. \quad (1.33)$$

With this we can find the exact expression

$$\begin{aligned} \tilde{G}_{ks}^0(\omega) &= - \int_0^{\beta} d\tau e^{-\tau(\mathcal{E}_k - \mu)} (1 - n_k) e^{i\omega\tau} \\ &= - \frac{e^{\beta(i\omega - \mathcal{E}_k + \mu)} - 1}{i\omega - \mathcal{E}_k + \mu} (1 - n_k). \end{aligned}$$

Since  $\omega$  is odd  $e^{i\beta\omega} = -1$

$$\begin{aligned} \tilde{G}_{ks}^0(\omega) &= - \frac{-e^{-\beta(\mathcal{E}_k - \mu)} - 1}{i\omega - \mathcal{E}_k + \mu} (1 - n_k) \\ &= \frac{e^{-\beta(\mathcal{E}_k - \mu)} + 1}{i\omega - \mathcal{E}_k + \mu} (1 + e^{-\beta(\mathcal{E}_k - \mu)})^{-1} \\ &= \frac{1}{i\omega - \mathcal{E}_k + \mu}. \end{aligned} \quad (1.34)$$

### 1.3.4 Interaction picture

We will consider  $H|_{U=0} \stackrel{!}{=} H_0$  to be the free part of the Hamiltonian and the rest as the interaction  $H_I$ . Then we define something analogous to the  $S$ -matrix [6]

$$e^{-\tau H} = e^{-\tau(H_0 + H_I)} = e^{-\tau H_0} S(\tau). \quad (1.35)$$

The time dependence of the states is still defined via free Hamiltonian (1.21). It is easy to solve for  $S(\tau)$  by differentiating both sides of (1.35).

$$-H e^{-\tau H} = e^{-\tau H_0} \frac{\partial S(\tau)}{\partial \tau} - H_0 e^{-\tau H_0} S(\tau).$$

Multiply both sides by  $e^{\tau H_0}$  gives an ordinary differential equation (ODE)

$$-H_I(\tau) S(\tau) = \frac{\partial S(\tau)}{\partial \tau}.$$

With the condition  $S(0) = 1$  this ODE has the solution

$$S(\tau) = T_{\tau} \exp \left\{ - \int_0^{\tau} H_I(\tau') d\tau' \right\} \quad (1.36)$$

$$= \sum_{n=0}^{\infty} \frac{(-)^n}{n!} \int_0^{\tau} d\tau_1 \cdots \int_0^{\tau} d\tau_n T_{\tau} [H_I(\tau_1) \cdots H_I(\tau_n)]. \quad (1.37)$$

Here  $T_\tau$  is again a time ordering operator. One important corollary comes from  $H_I$  being made up of two parts  $H_I = H_{I1} + H_{I2}$ . Then the expansion reads

$$S(\tau) = \sum_{n=0}^{\infty} \frac{(-)^n C_n^p}{n!} \int_0^\tau d\tau_1 \cdots \int_0^\tau d\tau_n T_\tau [H_{I1}(\tau_1) \cdots H_{I1}(\tau_p) H_{I2}(\tau_{p+1}) \cdots H_{I2}(\tau_n)]. \quad (1.38)$$

### 1.3.5 Correlator

Now we can define the full thermal *correlator* and denote with capital  $C$

$$C_{ks}(\tau) = - \frac{\text{Tr} \left[ e^{-\beta H} T_\tau [\phi_{ks}(\tau) \phi_{ks}^\dagger] \right]}{\text{Tr} \left[ e^{-\beta H} \right]}. \quad (1.39)$$

In literature this quantity is sometimes referred to as full propagator or dressed propagator and is denoted with  $\mathcal{G}$ . If we insert a complete set of states we can write the trace explicitly

$$\begin{aligned} C_{ks}(\tau > 0) &\propto \sum_{m,n,r} \langle m | e^{-(\beta-\tau)H} | n \rangle \langle n | \phi_{ks} e^{-\tau H} | r \rangle \langle r | \phi_{ks}^\dagger | m \rangle \\ &\propto \sum_{n,r} e^{-(\beta-\tau)E_n} \langle n | \phi_{ks} | r \rangle e^{-\tau E_r} \langle r | \phi_{ks}^\dagger | n \rangle \\ &\propto \sum_{n,r} e^{-\beta E_n} e^{\tau(E_n - E_r)} |z_{ks}^{nr}|^2. \end{aligned} \quad (1.40)$$

$E_n$  is the fully interacting energy of state  $n$ . In the literature this quantity may be written as calligraphic  $\mathcal{G}$  to emphasize that it is a propagator that depends on imaginary time  $\tau$ . Using the  $S$ -matrix we rewrite this expression [6]

$$C_{ks}(\tau) = - \frac{\text{Tr} \left[ e^{-\beta H_0} T_\tau [S(\beta) \phi_{ks}(\tau) \phi_{ks}^\dagger] \right]}{\text{Tr} \left[ e^{-\beta H_0} S(\beta) \right]}. \quad (1.41)$$

To avoid clutter we introduce new notation

$$Z_0^{-1} \text{Tr} \left[ e^{-\beta H_0} T_\tau [\cdots] \right] \doteq \langle T_\tau [\cdots] \rangle_0. \quad (1.42)$$

We can now write the correlator as

$$C_{ks}(\tau) = - \frac{\langle T_\tau [S(\beta) \phi_{ks}(\tau) \phi_{ks}^\dagger] \rangle_0}{\langle S(\beta) \rangle_0}. \quad (1.43)$$

This quantity is used in [4] to study the perturbative effects of Hubbard interaction on graphene sheets. This analysis can be extended to ribbons, giving similar qualitative results.

### 1.3.6 Wick's theorem

As we can anticipate, our calculations require the evaluation of quantities of the form  $\langle T_\tau [\Phi_1 \Phi_2 \Phi_3 \cdots] \rangle_0$ , where  $\Phi \in \{\phi, \phi^\dagger\}$ . We can calculate such quantities using Wick's theorem. First note that this expression can only be nonzero if there are an even number of fields. *Wick contraction* is defined as

$$\Phi_1^\bullet \Phi_2^\bullet = \frac{\{\Phi_1, \Phi_2\}}{1 + e^{\lambda_1 \beta \varepsilon_1}} = \langle \Phi_1 \Phi_2 \rangle_0 = \langle T_\tau [\Phi_1 \Phi_2] \rangle_0, \quad (1.44)$$

where

$$\lambda_i = \begin{cases} 1 & \Phi_i = \phi_i^\dagger \\ -1 & \Phi_i = \phi_i \end{cases}. \quad (1.45)$$

Assuming  $\tau_1 > \tau_2$ , explicit calculation shows that there are two options for the contraction

$$\phi_1^\dagger \bullet \phi_2^\bullet = \delta_{1,2} n_1, \quad (1.46)$$

$$\phi_1^\bullet \phi_2^\dagger \bullet = \delta_{1,2} (1 - n_1). \quad (1.47)$$

Now we can write the time ordered thermal average as a sum of all possible wick contractions [5]

$$\langle \Phi_1 \Phi_2 \Phi_3 \cdots \rangle_0 = [\Phi_1^\bullet \Phi_2^\bullet \Phi_3^\circ \Phi_4^\circ \cdots] - [\Phi_1^\bullet \Phi_2^\circ \Phi_3^\bullet \Phi_4^\circ \cdots] + \cdots. \quad (1.48)$$

This result is known as Wick's theorem.

### 1.3.7 Feynman Rules

We can diagrammatically express the interaction vertices and propagators/correlators of our system. This defines a set of Feynman rules,

$$\begin{aligned} G_{ks}^0 & \quad \longrightarrow \blacktriangleright \quad \sim \quad \frac{1}{i\omega - \varepsilon_k + \mu} \\ m^2 & \quad \text{---} \blacksquare \text{---} \quad \sim \quad -\frac{U}{2} \\ & \quad \begin{array}{ccc} l \downarrow & & l' \downarrow \\ & \searrow \quad \nearrow & \\ & \bullet & \\ & \nearrow \quad \searrow & \\ k \uparrow & & k' \uparrow \end{array} \quad \sim \quad V_{k'l'kl} \end{aligned} \quad (1.49)$$



interaction

$$\begin{aligned}
 & G_{\mathbf{p}\uparrow}^0(\omega) \Sigma_V^{\dagger} G_{\mathbf{p}\uparrow}^0(\omega) \\
 &= \int_{\tau_1, \tau} e^{i\omega\tau_1} \sum_{\mathbf{k}', \mathbf{l}', \mathbf{k}, \mathbf{l}} V_{\mathbf{k}'\mathbf{l}'\mathbf{k}\mathbf{l}} \langle T_{\tau} [\phi_{\mathbf{k}'\uparrow}^{\dagger}(\tau) \phi_{\mathbf{l}'\downarrow}^{\dagger}(\tau) \phi_{\mathbf{k}\downarrow}(\tau) \phi_{\mathbf{l}\uparrow}(\tau) \phi_{\mathbf{p}\uparrow}(\tau_1) \phi_{\mathbf{p}\uparrow}^{\dagger}] \rangle_0 \\
 &= - \int_{\tau_1, \tau} e^{i\omega\tau_1} \sum_{\mathbf{k}', \mathbf{l}', \mathbf{k}, \mathbf{l}} V_{\mathbf{k}'\mathbf{l}'\mathbf{k}\mathbf{l}} \left( -G_{\mathbf{p}\uparrow}^0(\tau_1 - \tau) \delta_{\mathbf{p}\mathbf{k}'} \right) \left( -G_{\mathbf{k}\downarrow}^0(0^-) \delta_{\mathbf{k}\mathbf{l}'} \right) \left( -G_{\mathbf{p}\uparrow}^0(\tau) \delta_{\mathbf{p}\mathbf{l}} \right) \\
 &= - \int_{\tau_1, \tau} e^{i\omega\tau_1} \sum_{\mathbf{k}} V_{\mathbf{p}\mathbf{k}\mathbf{k}\mathbf{p}} G_{\mathbf{p}\uparrow}^0(\tau_1 - \tau) G_{\mathbf{k}\downarrow}^0(0^-) G_{\mathbf{p}\uparrow}^0(\tau) \\
 &= G_{\mathbf{p}\uparrow}^0(\omega) G_{\mathbf{p}\uparrow}^0(\omega) \sum_{\mathbf{k}} n_{\mathbf{k}} V_{\mathbf{p}\mathbf{k}\mathbf{k}\mathbf{p}} \\
 &= G_{\mathbf{p}\uparrow}^0(\omega) G_{\mathbf{p}\uparrow}^0(\omega) \frac{U}{2\Lambda} \sum_{\mathbf{k}} n_{\mathbf{k}} \\
 &= \frac{U}{2} G_{\mathbf{p}\uparrow}^0(\omega) G_{\mathbf{p}\uparrow}^0(\omega).
 \end{aligned}$$

A similar calculation can be done for all possible incoming and outgoing particle/hole and up/down spin combinations. We'll find that the only terms surviving are  $\mathbf{p}s \rightarrow \mathbf{p}s$ , which means that up to the first order in  $U$  contributions from the mass term and quartic interaction cancel and leading order contribution is  $\sim \mathcal{O}(U^2)$ . Diagrammatically this cancellation is given as

The diagram shows a horizontal line with an arrow pointing right. On the left end, there is a dot. A circular loop with two arrows (one clockwise, one counter-clockwise) is attached to the dot. This diagram is followed by a plus sign and another horizontal line with an arrow pointing right, but with a square on the line. This is followed by an equals sign and a zero.

The leading order contribution therefore occurs at  $\mathcal{O}(U^2)$ . At this order we can use the previous result to deduce that the contributions with mass terms and tadpoles cancel. By direct inspection we get the following contributions

$$\begin{aligned}
 2 \times \text{---} \rightarrow \blacksquare \rightarrow \bullet \rightarrow \text{---} &= -\frac{U^2}{2} \int_{1,2} G_{\mathbf{p}\uparrow}^0(\tau_3 - \tau_1) G_{\mathbf{p}\uparrow}^0(\tau_2) G_{\mathbf{p}\uparrow}^0(\tau_1 - \tau_2), \\
 \text{---} \rightarrow \blacksquare \rightarrow \blacksquare \rightarrow \text{---} &= \frac{U^2}{4} \int_{1,2} G_{\mathbf{p}\uparrow}^0(\tau_1 - \tau_2) G_{\mathbf{p}\uparrow}^0(\tau_3 - \tau_1) G_{\mathbf{p}\uparrow}^0(\tau_2), \\
 \text{---} \rightarrow \bullet \rightarrow \bullet \rightarrow \text{---} &= \frac{U^2}{4} \int_{1,2} G_{\mathbf{p}\uparrow}^0(\tau_1 - \tau_2) G_{\mathbf{p}\uparrow}^0(\tau_3 - \tau_1) G_{\mathbf{p}\uparrow}^0(\tau_2),
 \end{aligned}$$

$$2 \times \text{---} \bullet \begin{array}{c} \square \\ \circlearrowleft \\ \circlearrowright \end{array} \text{---} = -\frac{U^2}{4\Lambda} \sum_l \int_{1,2} G_{p\uparrow}^0(\tau_3 - \tau_2) G_{p\uparrow}^0(\tau_2) G_{l\downarrow}^0(\tau_2 - \tau_1) G_{l\downarrow}^0(\tau_1 - \tau_2),$$

$$\text{---} \bullet \begin{array}{c} \circlearrowleft \\ \bullet \\ \circlearrowright \\ \bullet \\ \circlearrowleft \\ \circlearrowright \end{array} \text{---} = \frac{U^2}{4\Lambda} \sum_l \int_{1,2} G_{l\downarrow}^0(\tau_2 - \tau_1) G_{l\downarrow}^0(\tau_1 - \tau_2) G_{p\uparrow}^0(\tau_3 - \tau_2) G_{p\uparrow}^0(\tau_2).$$

As expected we observe

$$2 \times \text{---} \square \text{---} + \text{---} \bullet \begin{array}{c} \circlearrowleft \\ \circlearrowright \end{array} \text{---} + \text{---} \bullet \begin{array}{c} \circlearrowleft \\ \circlearrowright \\ \circlearrowleft \\ \circlearrowright \end{array} \text{---} = 0,$$

as well as

$$2 \times \text{---} \bullet \begin{array}{c} \square \\ \circlearrowleft \\ \circlearrowright \end{array} \text{---} + \text{---} \bullet \begin{array}{c} \circlearrowleft \\ \bullet \\ \circlearrowright \\ \bullet \\ \circlearrowleft \\ \circlearrowright \end{array} \text{---} = 0,$$

which leaves only so called “sunset diagram”

$$\text{---} \bullet \begin{array}{c} \circlearrowleft \\ \circlearrowright \end{array} \text{---}.$$

It is evaluated as

$$-\sum_{l'kl} V_{pl'kl} V_{klpl'} \int_{1,2,3} e^{i\omega\tau_3} G_{k\uparrow}^0(\tau_1 - \tau_2) G_{l\downarrow}^0(\tau_1 - \tau_2) G_{l'\downarrow}^0(\tau_2 - \tau_1) G_{p\uparrow}^0(\tau_3 - \tau_1) G_{p\uparrow}^0(\tau_2).$$

From here we can take the integral by going to frequency space and performing Matsubara sums [Equation B.7](#). After we amputate the outgoing legs [Equation B.8](#), we arrive at the final expression for the leading order contribution to the self-energy

$$\text{---} \bullet \begin{array}{c} \circlearrowleft \\ \circlearrowright \end{array} \text{---} = \sum_{l'kl} |V_{pl'kl}|^2 \frac{n_{-l'} n_k + (n_{l'} - n_k) n_{-l}}{i\omega - (\mathcal{E}_k^\rho - \mathcal{E}_{l'}^{\sigma'} + \mathcal{E}_l^\sigma) + \mu}.$$

We have defined  $-\mathbf{k} = (k, -\rho)$ . For 2-sites  $\mathcal{E}_k^\rho = \rho\mathcal{E}$  and  $|V_{pl'kl}|^2 = \frac{U^2}{4} \delta_{\pi\sigma',\rho\sigma}$ . If we denote

$$n_\pm = \frac{1}{1 + e^{\pm\beta\mathcal{E}}}, \quad (1.53)$$

we can write

$$\Sigma_{\pi s}^2(\omega) = \frac{U^2}{4} \left[ \frac{3n_- n_+}{i\omega - \pi\mathcal{E}} + \frac{1 - 3n_- n_+}{i\omega + \pi 3\mathcal{E}} \right].$$

### 1.3.9 Solving the quantization condition

It is apparent that the corrections to  $\Sigma$  are of the form

$$\sum_n \frac{C_n}{i\omega - R_n}. \quad (1.54)$$

This implies that the frequency dependent correlator is a rational function of  $\omega$ :

$$C_{ks}(i\omega) = \frac{1}{i\omega - \mathcal{E} - \sum_n \frac{C_n}{i\omega - R_n}} = \frac{P(i\omega)}{Q(i\omega)}, \quad (1.55)$$

where  $P, Q$  are polynomials. Finding residues of a rational function is very simple on a computer, so we are able to evaluate [Equation 1.52](#) numerically.

## 1.4 Numerical Methods

Large part of this work involves comparing and contrasting theoretical calculations with results from numerical simulations. Therefore, in this section, we provide a cursory description of the numerical formalisms that have been used.

### 1.4.1 Hybrid Monte Carlo

Thermal averages encountered in [section 1.3](#) can be estimated using computers, by sampling values from the *probability distribution* of the possible field configurations for given values of the system parameters, i.e.  $\beta, U, \mu$  etc. and using sampled field values to calculate the thermal averages [7]. This is a difficult task as the distribution is not known beforehand and must itself be estimated. Stochastic methods used to sample field values are collectively known as *Monte Carlo (MC)* methods (after the Monte Carlo Casino in Monaco). Monte Carlo methods are very general methods of sampling from the distributions using computers. The specific class of these methods used here are known as *Markov chain Monte Carlo (MCMC)*, where the aim is to start from some initial (and presumably random) configuration and construct the Markov chain of configurations that reach equilibrium and approximate the desired distribution,

$$\Phi_0 \rightarrow \Phi_1 \rightarrow \Phi_2 \rightarrow \dots \rightarrow \Phi. \quad (1.56)$$

We can start from any  $\Phi_0$  and if all configurations are reachable, that is to say we have *strong ergodicity*, then after a sufficient amount of time we will converge to the same distribution.

A Markov process only depends on the previous state of the system and transition amplitude  $T(\Phi_n|\Phi_{n-1})$  which is the probability of reaching configuration  $\Phi_n$  starting from the configuration

$\Phi_{n-1}$ . In equilibrium the probability of hopping in and out of any configuration must be the same. This can be accomplished under the condition of *detailed balance*

$$T(\Phi|\Phi')P(\Phi') = T(\Phi'|\Phi)P(\Phi). \quad (1.57)$$

Here  $P(\Phi)$  is the probability of the system being in configuration  $\Phi$ , usually one uses *Boltzmann factor* -  $e^{-\beta E_\Phi}$  for this. If we sum over all  $\Phi$ 's we get the desired equilibrium property

$$\sum_{\Phi} T(\Phi|\Phi')P(\Phi') = \sum_{\Phi} T(\Phi'|\Phi)P(\Phi), \quad (1.58)$$

where RHS is the probability of leaving configuration  $\Phi'$  and LHS is the probability of reaching it. When doing MCMC the first  $N_{therm}$  configurations are discarded to allow the system to equilibrate or *thermalize*. Subsequent configurations are saved with some chosen frequency and can be used for estimation of the observable quantities.

### Metropolis-Hastings Algorithm

The oldest and simplest MCMC algorithm is the Metropolis-Hastings:

1. Starting from  $\Phi_{n-1}$  choose  $\Phi_n$  using some predetermined method.
2. Accept the new configuration with a probability

$$\min\left(1, e^{-\beta\Delta E}\right), \quad \Delta E = E_n - E_{n-1}. \quad (1.59)$$

3. Go to 1.

Every MCMC algorithm builds on this. HMC specifically introduces a deterministic method of generating configurations based on the time evolution of the system. Since the Hamiltonian defines the flow on the phase space, it can be numerically integrated to evolve the system from  $\Phi_{n-1}$  to  $\Phi_n$ . This is referred to as *molecular dynamics*. In order to satisfy detailed balance molecular dynamics have to be reversible and area preserving in phase space, in other words the transformation  $\Phi_{n-1} \rightarrow \Phi_n$  must be canonical.

HMC also requires us to generate initial momenta  $\Pi_{n-1}$ . This is simply done by sampling the momenta from the Gaussian distribution  $\sim \mathcal{N}(0, 1)$  and letting the time evolution equilibrate the distributions. With this in mind we can write down the algorithm for HMC

1. Starting from  $\Phi_{n-1}$  sample  $\Pi_{n-1}$ .
2. Use molecular evolution to go from  $(\Phi_{n-1}, \Pi_{n-1})$  to  $(\Phi_n, \Pi_n)$ .
3. Accept the new configuration with probability

$$\min\left(1, \frac{e^{-\frac{\Pi_n^2}{2} - E_n}}{e^{-\frac{\Pi_{n-1}^2}{2} - E_{n-1}}}\right). \quad (1.60)$$

### 1.4.2 Leapfrog Integration

As mentioned in the previous section molecular dynamics must be area preserving in phase space and since we are dealing with finite precision calculations we must carefully choose the integration procedure in order to satisfy this requirement. The simplest one is known as the *Leapfrog*. It is a specific case of the more general class of Omelyan integrators [8]. Given an initial  $(\Phi(0), \Pi(0))$  and timestep  $h$  we first advance momenta by a half step

$$\Pi\left(\frac{h}{2}\right) = \Pi(0) - \left.\frac{\partial H}{\partial \Phi}\right|_0 \frac{h}{2}. \quad (1.61)$$

Then we apply Euler method to  $\Phi$  and  $\Pi$  successively

$$\Phi(nh) = \Phi(nh - h) + \Pi\left(\frac{h}{2}\right) h \quad (1.62)$$

$$\Pi\left(nh + \frac{h}{2}\right) = \Pi\left(nh - \frac{h}{2}\right) - \left.\frac{\partial H}{\partial \Phi}\right|_{nh} h. \quad (1.63)$$

Finally we do last half step to get the final value of momenta

$$\Pi(nh) = \Pi\left(nh - \frac{h}{2}\right) - \left.\frac{\partial H}{\partial \Phi}\right|_{nh} \frac{h}{2}. \quad (1.64)$$

In our case  $\Phi(0) = \Phi_{n-1}$  and  $\Phi(nh) = \Phi_n$ , this is the configuration we do accept-reject step for. It is easy to see that leapfrog integration has unit Jacobian. Each individual transformation changes only  $\Phi$  or  $\Pi$  and the transformations can be written using upper triangular matrices. e.g.

$$\frac{\partial (P(h/2), Q(0))}{\partial (P(0), Q(0))} = \det \begin{pmatrix} 1 & -\left.\frac{\partial H}{\partial \Phi}\right|_0 \frac{h}{2} \\ 0 & 1 \end{pmatrix} = 1. \quad (1.65)$$

The same goes for all other transformations. The Jacobian of successive transforms is a product of individual Jacobians. Since the Jacobian is 1 the integration procedure preserves the volume in phase space.

### 1.4.3 Fitting Correlators

After generating configurations using HMC and calculating correlators, we want to fit them to a sum of exponentials to extract various interacting energy contributions as given in [Equation 1.40](#). Fitting the sum of exponentials is a notoriously hard problem. In this manuscript I'll describe one method that reformulates the problem. As we know the sum of exponentials is a solution to a linear ordinary differential equation (ODE) with constant coefficients. Let

$$C(\tau) = k_0 + \sum_{n=1}^N A_n e^{-\epsilon_n \tau}. \quad (1.66)$$

Then it must be a solution of

$$\frac{d^N}{d\tau^N}C + a_{N-1}\frac{d^{N-1}}{d\tau^{N-1}}C + \cdots + a_1\frac{d}{d\tau}C + a_0C = k_0, \quad (1.67)$$

if and only if the exponents  $\mathcal{E}$  are the roots of the characteristic polynomial,

$$\mathcal{E}^N + a_{N-1}\mathcal{E}^{N-1} + \cdots + a_1\mathcal{E} + a_0 = 0. \quad (1.68)$$

If we integrate [Equation 1.67](#)  $N$  times we get

$$C + a_{N-1} \int d\tau C + \cdots + a_1 \int^{N-1} d\tau C + a_0 \int^N d\tau C = k_N + k_{N-1}\tau + \cdots + k_0\tau^N. \quad (1.69)$$

Since the correlators are given for discrete values of  $\tau = \delta n$  the integrals are calculated via trapezoidal approximation

$$\int_0^{n\delta} d\tau f(\tau) \doteq \sum_{j=0}^{n-1} \frac{f(j\delta) + f(j\delta + \delta)}{2} \delta. \quad (1.70)$$

We denote the  $n$ 'th integral evaluated at  $j\delta$  as  $C_j^m$ . We then repeatedly apply trapezoidal integration and generate a data matrix of the shape  $N_t \times N - 1$

$$Y = \begin{pmatrix} C_0^1 & \cdots & C_0^N \\ C_1^1 & \cdots & C_1^N \\ \vdots & & \\ C_{N_t}^1 & \cdots & C_{N_t}^N \end{pmatrix}. \quad (1.71)$$

Now we construct the *Vandermonde matrix* for  $\tau$ 's

$$V = \begin{pmatrix} 1 & 0 & \cdots & 0 \\ 1 & \delta & \cdots & \delta^N \\ \vdots & & & \vdots \\ 1 & N_t\delta & \cdots & (N_t\delta)^N \end{pmatrix}. \quad (1.72)$$

We then adjoin the two matrices  $(-Y|V)$  and solve the least squares problem

$$\begin{pmatrix} -C_0^1 & \cdots & -C_0^N & 1 & 0 & \cdots & 0 \\ -C_1^1 & \cdots & -C_1^N & 1 & \delta & \cdots & \delta^N \\ \vdots & & & \vdots & & & \\ -C_{N_t}^1 & \cdots & -C_{N_t}^N & 1 & N_t\delta & \cdots & (N_t\delta)^N \end{pmatrix} \begin{pmatrix} a_{N-1} \\ a_{N-2} \\ \vdots \\ k_0 \\ k_1 \\ \vdots \end{pmatrix} = \begin{pmatrix} C_0^0 \\ C_1^0 \\ \vdots \end{pmatrix}. \quad (1.73)$$

By using the coefficients  $a_{N-1}, a_{N-2}, \dots$  we can write down the characteristic polynomial and solve it numerically to obtain the estimated  $\hat{\mathcal{E}}_n$ 's. With the exponentials known, we can estimate both the  $A_n$ 's

as well as  $k_0$  by minimizing

$$\sum_{j=0}^{N_t-1} \left| C(j\delta) - k_0 - \sum_n A_n e^{-\hat{\epsilon}_n j \delta} \right|^2. \quad (1.74)$$



## CHAPTER 2

---

# Topology and symmetry in carbon nanoribbons

---

This chapter is based on [1]

**Topology and symmetry in carbon nanoribbons**, L. Razmadze, PoS **Regio2021** 031 (2022)

In the field of *condensed matter physics*, energy gaps provide essential insights into the electronic and quantum behaviors of physical systems. As the size of a system approaches infinity, referred to as the *thermodynamic limit*, the difference between the ground state and the first excited state energy approaches at a certain value. Systems are classified as *gapped* if this energy difference remains non-zero and typically exhibit insulating behavior. Conversely, for *gapless systems* this energy difference is zero, which means creating excitations requires very little energy giving such system metallic or semi-metallic characteristics. These distinctions between gapped and gapless phases form the foundation for understanding the topological nature of different states of matter.

The behavior of a quantum system is governed by a *Hamiltonian*  $H$  that describes the total energy as a function of parameters such as hopping energies, interaction strengths, and chemical potentials. When the parameters are varied *adiabatically* the ground state of starting Hamiltonian gets mapped to the ground state of the final Hamiltonian. If this can be done without closing the energy gap, we say that the two belong to the same *equivalence class*. Topologically trivial class would be an *atomic insulator*, where electrons are tightly bound to the atomic cores. If a system is not equivalent to the atomic insulator under this definition, it signifies a potential topological phase transition. This provides a more refined definition of phases of matter, highlighting that two systems can both be classified as insulators—characterized by an energy gap—yet display fundamentally different behaviors.

An essential application of topology in condensed matter physics is the emergence of *topologically protected quantum states*, which derive their robustness from global properties rather than local perturbations. These states are remarkably resistant to noise and external disturbances, making them prime candidates for fault-tolerant quantum computing. A prototypical example of this phenomenon is the *Kitaev chain*, a one-dimensional model that exhibits a transition between trivial and non-trivial topological phases. The non-trivial phase supports *Majorana zero modes*, localized edge states with zero energy that are fundamentally distinct from the bulk states. These modes have been studied as potential physical realizations of *topological qubits* for quantum information processing due to their non-local encoding of information, which enhances their stability against local decoherence.

The model studied in this work extends the Kitaev chain framework to hexagonal carbon nanoribbons (CNRs) with both zigzag and armchair geometries. These nanoribbons, derived from graphene, possess unique electronic properties due to their quasi-one-dimensional structure and edge configurations. The system is described using the *BCS-Hubbard model*, which incorporates nearest-neighbor hopping  $t$ , Hubbard interaction  $U$ , and superconducting pairing  $\Delta$ . Superconducting pairs can be experimentally introduced by placing the nanoribbons on a superconductive substrate. Importantly, the model is *exactly solvable* when the hopping and pairing strengths are equal ( $t = \Delta$ ), allowing for a detailed analysis of how the system's energy gap and quantum phases depend on interaction strength  $U$ .

For  $U = 0$ , the system behaves similarly to a *gapless metal* for certain nanoribbon widths, particularly in zigzag configurations and armchair ribbons with widths  $W = 3m + 2$  (where  $m$  is an integer). As  $U$  increases, the energy gap opens, indicating a transition to a gapped state distinct from an atomic insulator. In the opposite limit, as  $U \rightarrow \infty$ , the system approaches an insulating state characterized by strong electron localization. This behavior demonstrates the intricate interplay between interactions, geometry, and superconducting pairing.

The study applies the BCS-Hubbard model to derive *effective Hamiltonians* for ZNRs and ANRs, taking into account both *ferromagnetic* ( $F$ ) and *antiferromagnetic* ( $AF$ ) orders. In the  $AF$  phase, sublattices exhibit opposite spin polarizations, leading to a doubly degenerate energy spectrum with a gap. In contrast, the  $F$  phase, where spins align uniformly, results in a splitting of energy levels. The analysis shows that both ZNRs and ANRs undergo gap-opening.

By transforming the Hamiltonian into a *Majorana fermion representation*, the study reveals a connection to a *4D Dirac equation*, enabling further exploration of the system's topological invariants and conserved quantities. For gapped ANRs as the interaction strength increases the gap closes and then opens again implying the existence of a *critical interaction strength*  $U_c$  where potential transition between topologically distinct phase occurs.

## 2.1 Introduction

Topology is an interesting mathematical field in and of itself and existing toolkit of topology can be used in condensed matter to extend classification of states of matter.

### 2.1.1 Topology in condensed matter

Key concept in topology is *continuity*. Two topological spaces are considered to be equivalent if they can be continuously mapped to each-other. In condensed matter systems we introduce the notion of *topological equivalence* on the space of gapped Hamiltonians. Hamiltonian is gapped if the difference in its ground state and first excited state energies remains finite in the limit where we take the system to be infinitely large.

Consider a space  $\Omega$  of Hamiltonians. Two Hamiltonians are defined as topologically equivalent if the two can be connected in the Hamiltonian space without closing the energy gap. Physically this corresponds to adiabatically changing the parameters to transform one Hamiltonian into another while every intermediate Hamiltonian remains gapped. In [Figure 2.1](#)  $H$  and  $H''$  are equivalent since there exists a path connecting them while satisfying this requirement. But  $H'$  is separated from  $H$  and  $H''$  by a wall of gap closing denoted in red, meaning  $H$  and  $H'$  are topologically inequivalent.

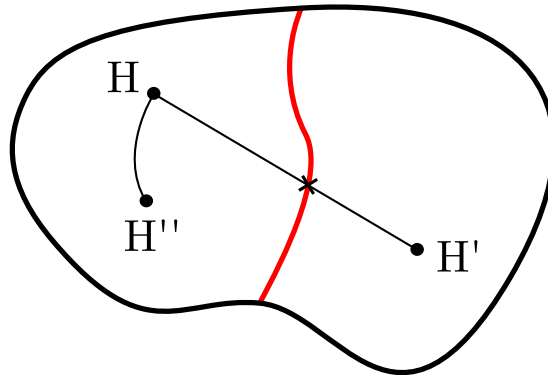


Figure 2.1: Hamiltonian space with two phases separated by wall of gap closing denoted in red.  $H$  and  $H''$  are equivalent while  $H$  and  $H'$  are not.

Having defined equivalence we have to define a *topologically trivial phase*. For this we choose *atomic insulators* which are insulating because electrons are tightly bound to the atomic cores inside the solid. If a system is not topologically equivalent to an atomic insulator then we say that it is topological.

## 2.2 Kitaev Chain

Kitaev introduced a 1D toy model [9] in order to argue that Majorana states could be created in solid state systems. His main motivation was development of Majoranas as qubits for quantum computing due to their robustness, which stems from the topological invariant that the system possesses - Parity. The chain is a 1D system with nearest neighbor hopping  $t$ , chemical potential  $\mu$  and nearest neighbor superconductive pairing  $\Delta$ . These physical properties span our parameter space. Hamiltonian is given as

$$H = -t \sum_{j=1}^{L-1} (c_j^\dagger c_{j+1} + h.c.) + \Delta \sum_{j=1}^{L-1} (c_j c_{j+1} + h.c.) - \mu \sum_{j=1}^L n_j, \quad (2.1)$$

where  $n_j = c_j^\dagger c_j$  is the number operator. Note first two sums don't include last lattice site due to *open boundary conditions*. Also note that due to the pairing term  $U(1)$  symmetry is broken down to  $\mathbb{Z}_2$ . In order to investigate this system further we assume each lattice cite to be occupied by two Majorana fermions  $c \rightarrow \gamma_a, \gamma_b$  (see [Figure 2.2\(a\)](#))

$$\gamma_{ja} = c_j + c_j^\dagger, \quad \gamma_{jb} = i(c_j - c_j^\dagger). \quad (2.2)$$

Ordinary fermion operators  $c$  are *nilpotent* meaning  $\exists n \in \mathbb{N} : c^n = 0$ . For spin-1/2 particles like we have here,  $n = 2$ . Majorana fermions  $\gamma$  are superpositions of creation and annihilation operators of ordinary fermions, because of that they are no longer nilpotent, instead  $\gamma^2 = 1$ . They do, however, still retain the anti-commutation property of ordinary fermions, that is to say  $\{\gamma_{i\lambda}, \gamma_{j\lambda'}\} = \delta_{ij} \delta_{\lambda\lambda'}$ . parity operator can be constructed by taking products of these operators

$$P = \prod_{j=1}^L (-i\gamma_{ja}\gamma_{jb}). \quad (2.3)$$

Assuming symmetric line conditions ( $\Delta = t$ ) results in

$$H = t \sum_{j=1}^{L-1} i\gamma_{jb}\gamma_{j+1a} - \frac{\mu}{2} \sum_{j=1}^L (1 + i\gamma_{ja}\gamma_{jb}). \quad (2.4)$$

This system admits two limits  $\mu \gg t$  and  $t \gg \mu$ . In first case ([Figure 2.2\(b\)](#)) majoranas become bound on the same cites and and there is no more hopping between the neighboring cites. This system has a unique ground state. In the opposite limit we end up with a 2-fold degenerate ground state. Degeneracy is due to parity -  $P = \pm 1$ . As we can see for two sets of  $(t, \Delta, \mu)$  we get two Hamiltonians with different eigensystems. If we were to smoothly vary these parameters  $(0, 0, \mu) \rightarrow (t, t, 0)$  there would be gap closing at  $(t, t, 2t)$  which, from the definition in section 2.1.1, means that these two Hamiltonians represent topologically distinct phases.

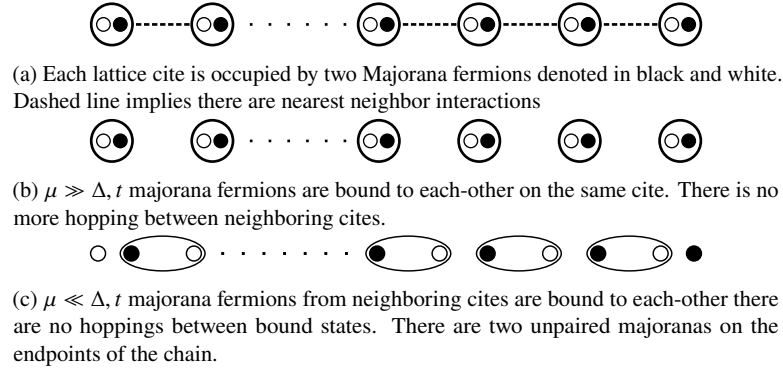


Figure 2.2: Diagrammatic representation of various phases in Kitaev chain

## 2.3 BCS-Hubbard Model

### 2.3.1 Hamiltonian

Consider an N-dimensional general bipartite lattice with nearest neighbor hopping -  $t$  and superconductive(SC) pairing -  $\Delta$ . Hopping and SC are defined only between different sublattices. Here sublattices  $A$  and  $B$  are color-coded in blue and red to make the equations more amenable to visual parsing. In this chapter  $i$  and  $j$  will be exclusively referring to cites on sublattice  $A$  and  $B$  respectively and will be color-coded accordingly as  $i \in A$  and  $j \in B$ . Nearest neighbors are denoted as  $\langle i, j \rangle$  and  $\sigma$  is a label for spin. Write Hamiltonian as in [10]

$$H_{\text{free}} = \sum_{\langle i, j \rangle \sigma} t_{ij} c_{i\sigma}^\dagger c_{j\sigma} + h.c. + \Delta_{ij} c_{i\sigma}^\dagger c_{j\sigma}^\dagger + h.c.. \quad (2.5)$$

Furthermore Hubbard interaction at half filling is defined using the spin degrees of freedom.

$$H_{\text{hubbard}} = U \sum_l \left( n_{l\uparrow} - \frac{1}{2} \right) \left( n_{l\downarrow} - \frac{1}{2} \right). \quad (2.6)$$

For a homogeneous case  $t_{ij} = t$  and  $\Delta_{ij} = \Delta$ .

### 2.3.2 Composite fermions

We go to Majorana basis similar to Kitaev model

$$c_{i\sigma} = \eta_{i\sigma} + i\beta_{i\sigma}, \quad c_{j\sigma} = \beta_{j\sigma} + i\eta_{j\sigma},$$

resulting in

$$H = \sum_{\langle i, j \rangle \sigma} 2i(t - \Delta)\eta_{i\sigma}\eta_{j\sigma} - 2i(t + \Delta)\beta_{i\sigma}\beta_{j\sigma} - U \sum_l (2i\beta_{l\uparrow}\beta_{l\downarrow})(2i\eta_{l\uparrow}\eta_{l\downarrow}). \quad (2.7)$$

At Symmetric lines  $D_l = 4i\eta_{l\uparrow}\eta_{l\downarrow}$  is conserved for each lattice cite as was shown in [11], [12].

However,  $D^1 = \sum_l 4i\beta_{l\uparrow}\beta_{l\downarrow}$  and  $D^2 = \sum_l 4i\eta_{l\uparrow}\eta_{l\downarrow}$  are conserved for all values of  $\Delta, t$ . Which is easy to show by writing  $[H, D^a]$  and using commutator-anticommutator identities.

From here we can make another change of basis to composite  $d$ -fermions.

$$\begin{aligned} d_{i1} &= \beta_{i\uparrow} - i\beta_{i\downarrow}, & d_{j1} &= \beta_{j\uparrow} + i\beta_{j\downarrow}, \\ d_{i2} &= \eta_{i\uparrow} + i\eta_{i\downarrow}, & d_{j2} &= \eta_{j\uparrow} - i\eta_{j\downarrow}. \end{aligned}$$

For  $\Delta = t$  Hamiltonian becomes quadratic for any value of  $U$ , hence diagonalizable. Moreover since  $D_l$  is conserved and  $D_l^2 = 1$  Hilbert space gets split into  $2^N$  sectors where  $N$  is the number of lattice sites. In composite fermion basis  $D_l$  measures  $\hat{y}$ -axis spin polarization.

## 2.4 Carbon Nanoribbons

Applying BCS-Hubbard model to nanoribbons we derive Bloch matrix for zigzag and armchair geometries and for both ferromagnetic and antiferromagnetic cases. In the rest of the paper  $D_{am}$  and  $D_{bm}$  are  $D_l$  for sublattices  $A$  and  $B$  respectively.  $m$  is the index of lattice sites along the width of the ribbon. Choosing a specific Hilbert space sector is tantamount to setting corresponding  $D_l$ 's to 1 or -1.

### 2.4.1 Zigzag Nanoribbon(ZNR)

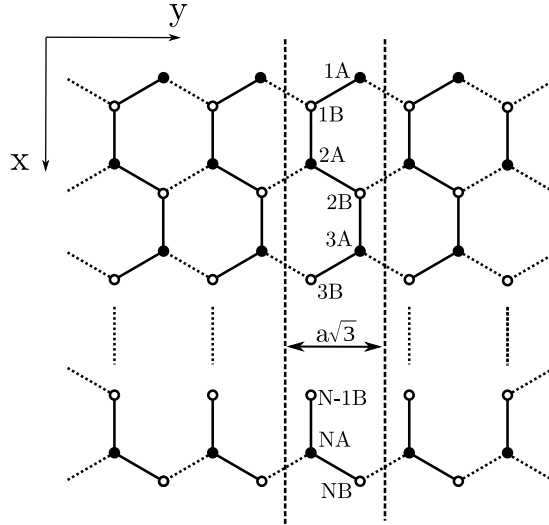


Figure 2.3: Lattice of an zigzag carbon nanoribbon, with unit cell(dashed) of size  $a\sqrt{3}$ , width  $N$  and length  $L_y$ .

#### Antiferromagnetic(AF) order

In [12] the ground state of this system is shown to belong to the sector of the Hilbert space where  $D_{am} = -D_{bm} = -1$ . This shall be referred to as *AF order*, since in this sector both sub-lattices are populated by  $d_2$ -fermions and on different sub-lattices  $d_2$  has opposite  $y$ -polarizations. This can be

verified by examining the transformations between ordinary and composite fermions bases. Now the matrix can be written as

$$H_k = \begin{pmatrix} -\frac{U}{2} & 0 & 0 & 2it(g_k\mathbb{1} + \mathbb{K}) \\ 0 & \frac{U}{2} & 2it(g_k\mathbb{1} + \mathbb{K}) & 0 \\ 0 & -2it(g_k\mathbb{1} + \mathbb{K}^\dagger) & -\frac{U}{2} & 0 \\ -2it(g_k\mathbb{1} + \mathbb{K}^\dagger) & 0 & 0 & \frac{U}{2} \end{pmatrix}. \quad (2.8)$$

$\mathbb{K} = \sum_m |m\rangle\langle m+1|$  is a unilateral shift operator with ones on the upper diagonal and  $g_k = 2 \cos(\sqrt{3}ka/2)$ . Energy levels are given in Figure 2.4(b). We observe gap opening however the degeneracy is not lifted and every level is still doubly degenerate.

### Ferromagnetic(F) order

*Ferromagnetic* in this context means we are considering the sector of Hilbert space where only one sub-lattice is populated by  $d_2$ -fermions. It corresponds to the state in which all  $d_2$  fermions are aligned. It's the same as setting  $D_l = 1$  or  $D_l = -1$ . Now the matrix looks like

$$H_k = \begin{pmatrix} \mp\frac{U}{2} & 0 & 0 & 2it(g_k\mathbb{1} + \mathbb{K}) \\ 0 & \pm\frac{U}{2} & 2it(g_k\mathbb{1} + \mathbb{K}) & 0 \\ 0 & -2it(g_k\mathbb{1} + \mathbb{K}^\dagger) & \pm\frac{U}{2} & 0 \\ -2it(g_k\mathbb{1} + \mathbb{K}^\dagger) & 0 & 0 & \mp\frac{U}{2} \end{pmatrix}. \quad (2.9)$$

Since the spectrum is symmetric around zero,  $\pm$  doesn't change anything, and after solving for the eigenvalues and plotting them w.r.t. momentum (Figure 2.4(c)) one can see energy levels splitting.

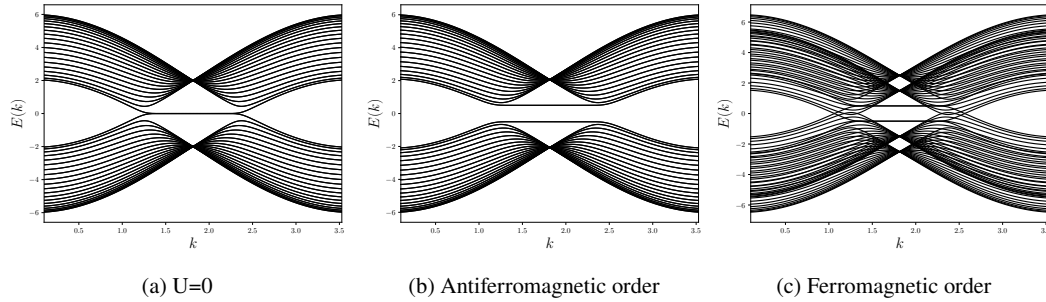


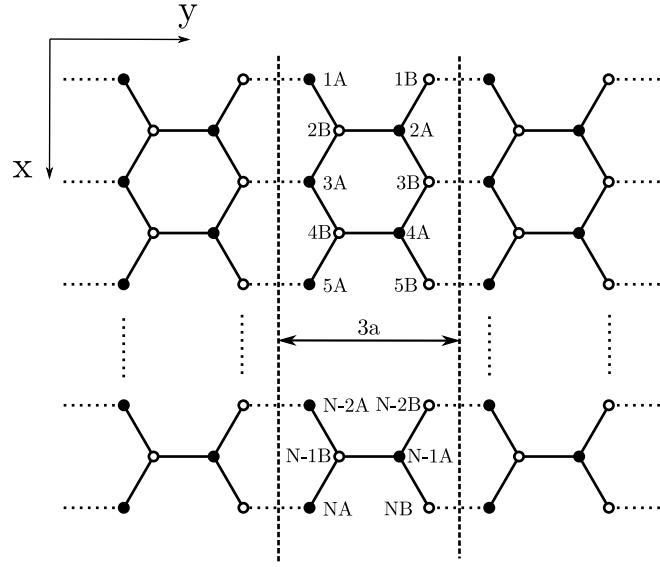
Figure 2.4: Zigzag energy levels for F and AF orders.  $E(k)$  and  $k$  are measured in units of  $t$ . Calculation is done for  $N = 20$ ,  $U = 1$

### 2.4.2 Armchair Nanoribbon(ANR)

Armchair nanoribbon behavior depends on it's width. It can be metallic or have an energy gap.

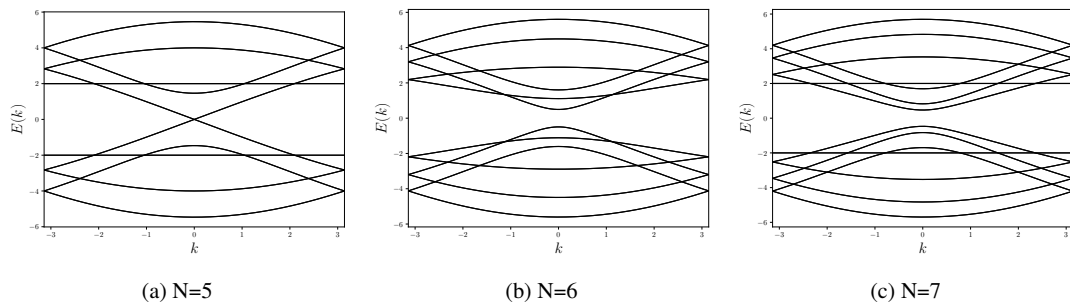
#### Antiferromagnetic(AF) order

As it was for zigzag configuration AF order here means that we are in the Hilbert space sector defined by  $D_{am} = -D_{bm} = -1$  and the matrix is rewritten as


 Figure 2.5: Lattice of an armchair carbon nanoribbon, with unit cell(dashed) of size  $3a$ , width  $N$  and length  $L_y$ 

$$H_k = \begin{pmatrix} -\frac{U}{2} & 0 & 0 & 2it(\mathbb{1} + e^{-ika_t/2} \mathbb{J}) \\ 0 & \frac{U}{2} & 2it(\mathbb{1} + e^{ika_t/2} \mathbb{J}) & 0 \\ 0 & -2it(\mathbb{1} + e^{-ika_t/2} \mathbb{J}) & -\frac{U}{2} & 0 \\ -2it(\mathbb{1} + e^{ika_t/2} \mathbb{J}) & 0 & 0 & \frac{U}{2} \end{pmatrix}. \quad (2.10)$$

$\mathbb{J} = \sum_m |m\rangle\langle m+1| + |m+1\rangle\langle m|$  is a bilateral shift operator with ones on the upper and lower diagonals. Solving for the eigenvalues for every value of  $k$  and plotting the results gives the energy band structure 2.7(a), 2.7(b), 2.7(c). As with zigzag geometry here too we observe gap opening without lifting the degeneracy.


 Figure 2.6: Energy bands for widths 5,6,7 for the case  $U = 0$ . Everything is measured in units of  $t$ .

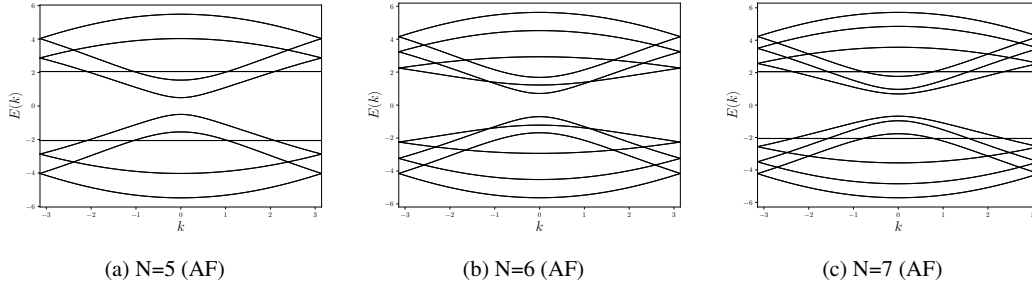


Figure 2.7: Energy bands for widths 5,6,7 in antiferromagnetic order. Everything is measured in units of  $t$ . For all calculations  $U = 1$

### Ferromagnetic(F) order

*Ferromagnetic* as it was for zigzag nanoribbon means we are considering the sector of Hilbert space where only one sub-lattice is populated by  $d_2$ -fermions, resulting in  $D_{am} = D_{bm} = \pm 1$ . Now the matrix looks like

$$H_k = \pm \begin{pmatrix} \mp \frac{U}{2} & 0 & 0 & 2it(\mathbb{1} + e^{-ika_t/2} \mathbb{J}) \\ 0 & \pm \frac{U}{2} & 2it(\mathbb{1} + e^{ika_t/2} \mathbb{J}) & 0 \\ 0 & -2it(\mathbb{1} + e^{-ika_t/2} \mathbb{J}) & \pm \frac{U}{2} & 0 \\ -2it(\mathbb{1} + e^{ika_t/2} \mathbb{J}) & 0 & 0 & \mp \frac{U}{2} \end{pmatrix}. \quad (2.11)$$

Since the spectrum is symmetric  $\pm$  doesn't change anything. Solving for the eigenvalues and plotting it w.r.t. we can see the same behavior as in zigzag case, degeneracy is lifted (Figure 2.8(a), Figure 2.8(b), Figure 2.8(c)). For some widths there exists a critical value of  $U = U_c$  where the band gap closes, but if we keep increasing  $U$  eventually gap opens again and the band structure becomes that of a trivial insulator. Since band closing is unavoidable initial state must be topologically nontrivial.

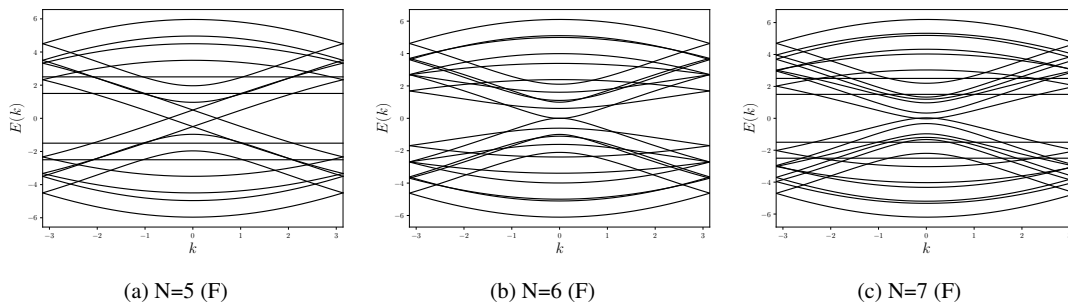


Figure 2.8: Energy bands for widths 5,6,7 in ferromagnetic order. Everything is measured in units of  $t$ . For all calculations  $U = 1$

## 2.5 Effective Hamiltonian

As we have seen the Hamiltonian can be written as

$$H_{\text{ZNR}} = -\frac{U}{2}D \otimes \sigma_z - 2t\mathbb{1} \otimes \sigma_y \otimes \sigma_x + itg_k\mathbb{K} \otimes \sigma^+ \otimes \sigma_x - itg_k\mathbb{K}^\dagger \otimes \sigma^- \otimes \sigma_x, \quad (2.12)$$

or

$$H_{\text{ANR}} = -\frac{U}{2}D \otimes \sigma_z - 2\tilde{t}(\mathbb{1} + \mathbb{J} \cos(ka_T/2)) \otimes \sigma_y \otimes \sigma_x - 2\tilde{t} \sin(ka_T/2) \mathbb{J} \otimes \sigma_y \otimes \sigma_y. \quad (2.13)$$

Matrix  $D$  depending on Hilbert space sector can take the form  $D = \mathbb{1} \otimes \mathbb{1}$  or  $D = \mathbb{1} \otimes \sigma_z$ .  $\sigma_i$  are Pauli matrices, and  $\sigma_\pm = \sigma_x \pm i\sigma_y$ . Now we diagonalize the first term in the matrix product. Let  $A \in \{\mathbb{J}, \mathbb{K}\}$  Then there exists a unitary transform such that

$$UAU^\dagger = \text{diag}(\lambda_1, \lambda_2, \dots), \quad (2.14)$$

where  $\lambda$ 's are the eigenvalues and consequently

$$U(\mathbb{1} + A)U^\dagger = \text{diag}(\lambda_1 + 1, \lambda_2 + 1, \dots). \quad (2.15)$$

For every  $\lambda$  Equation 2.12 and Equation 2.13 become 4d Dirac equations, since direct product of Pauli matrices along with  $2 \times 2$  unit matrix spans Clifford algebra. In fact we are free to choose the basis  $\{\Gamma_a\}_{a=1\dots 5}$  as long as it satisfies anti-commutation relations

$$\{\Gamma_a, \Gamma_b\} = 2\delta_{ab}, \quad [\Gamma_a, \Gamma_b] = 2i\Gamma_{ab}. \quad (2.16)$$

One possible choice is [13]

$$\{\sigma_x \otimes \mathbb{1}, \sigma_z \otimes \mathbb{1}, \sigma_y \otimes \sigma_x, \sigma_y \otimes \sigma_y, \sigma_y \otimes \sigma_z\}. \quad (2.17)$$

---

## Localization of electronic states in hybrid nanoribbons in the nonperturbative regime

---

This chapter is based on [2]

**Localization of electronic states in hybrid nanoribbons in the nonperturbative regime** T. Luu, U. Meißner and L. Razmadze, Phys. Rev. B **106**, 195422 (2022) [[arXiv:cond-mat/2204.02742](https://arxiv.org/abs/cond-mat/2204.02742)]

In this work, we investigate the localization of low-energy states in *7/9-hybrid nanoribbons* under strong interactions and within a finite volume. The primary objective is to understand how quasi-particle states behave in non-perturbative regimes, where analytical solutions are challenging, and the system's properties are dominated by strong electron-electron interactions.

Localized edge states have been extensively studied in zigzag nanoribbons [14], which are known to support zero-energy modes. In contrast, *armchair nanoribbons* do not support zero-energy edge modes but remain compelling candidates for nanoengineering due to their potential to form hybrid configurations. Hybrid armchair nanoribbons represent a more complex geometry, constructed from different-width armchair ribbons capable of supporting localized states. The existence of localized, low-energy states at the junctions of such ribbons has been demonstrated, even in the non-interacting, tight-binding scenario [15]. These states have been identified as *symmetry-protected topological* (SPT) states, with their properties determined by associated topological  $\mathbb{Z}_2$  invariant. Notably, the SPT protection of these states is strictly enforced only for infinitely long nanoribbons extending from the junctions. For finite systems or repeating lattice arrangements, a more detailed examination of their stability and low-energy nature is necessary. The topological nature of junction states makes them promising candidates for potential building blocks for quantum engineering.

Our study focuses on periodic *7/9- and 13/15-hybrid nanoribbons* to address the effects of finite volume, where finite volume refers to the periodicity-induced finite separation between junctions. Two distinct non-perturbative regimes are investigated. First, the Hubbard model at half-filling is employed, and *quantum Monte Carlo* (QMC) simulations are performed for various on-site coupling values  $U$ , including the strongly interacting regime. Second, the *symmetric line limit* of the BCS-Hubbard model is analyzed, where a nearest-neighbor superconducting pairing  $\Delta$  of equal magnitude to the hopping parameter  $t$  is introduced. In this limit, the single-particle spectrum and wavefunctions can be analytically determined for any  $U$  when expressed in the Majorana basis.

We examine hybrid nanoribbons formed by joining two armchair graphene nanoribbons (AGNRs) of different widths, focusing primarily on configurations that differ in width by 2 sites. The central question addressed is whether the edge-localized states, which are characteristic of specific ribbon geometries, persist in the presence of strong interactions and superconductivity. By extracting the *site-dependent quasi-particle wavefunction densities*, we provide a detailed analysis of the spatial distribution of electronic states across the nanoribbon junction.

A key result is that the *localization of electronic states* persists even in non-perturbative regimes under specific parameter conditions. In the case of the Hubbard model at half-filling, strong interactions  $U$  do not entirely delocalize the edge states, though they modify the wavefunction density distribution. For the superconducting case, the exact solutions at the symmetric line limit show that quasi-particle localization is robust for particular combinations of interaction strength and hopping parameters.

The finite periodicity of the hybrid nanoribbon introduces a finite separation between junctions, affecting the energy spectrum. However, our findings indicate that this does not eliminate the topological characteristics of the junction states. The energy levels of the localized states depend strongly on  $U$ , but these states consistently remain the system's lowest-energy states. Additionally, the behavior of the 13/15-hybrid ribbons mirrors that of the 7/9 system, supporting the generality of our findings.

By transforming the Hamiltonian into a *Majorana fermion representation*, we reveal a connection to a *4D Dirac equation*, enabling further exploration of the system's topological invariants and conserved quantities. We also draw parallels between these hybrid systems and *domain-wall fermions* in lattice gauge theories, highlighting similarities in the mechanisms responsible for state localization and

protection.

The exploration of hybrid nanoribbons contributes to the broader understanding of *symmetry-protected topological* (SPT) states in finite systems. By investigating these states under varying interaction strengths and geometrical configurations, we provide insights into their potential applications in quantum technologies. The robustness of the localized states, demonstrated under both non-perturbative regimes, highlights their potential for incorporation into quantum devices. Our findings suggest that these junction states could serve as robust carriers of quantum information, paving the way for further exploration of hybrid nanoribbon systems and their applications in fault-tolerant quantum computation.

### 3.1 Introduction

Recently it was shown that localized, low-energy states can occur at the junction of two nanoribbons that are topologically distinct [15]. The presence of such symmetry-protected topological (SPT) localized states depends on their junction geometry and topological invariance. The ability to engineer such hybrid ribbons [16, 17] has spurred research into the use of these systems for manufacturing quantum dots [18], potentially leading the way to novel, advanced electronic devices and an avenue for obtaining fault-tolerant quantum computing.

The existence of localized edge states has been widely explored in, for example, zigzag nanoribbons [14], where depending on the the presence of interactions and/or disorder the ribbon can change from a topological insulator to a trivial or Mott insulator [19, 20]. On the other hand, the hybrid armchair configurations we consider here are less studied despite their promise as an interesting nanoengineering candidate. In some sense they represent the next simplest ribbon geometry that can support localized states. As in the zigzag nanoribbon case, these localized states are manifest in the non-interacting, tight-binding scenario. However, SPT protection is only strictly enforced when both ribbons extend infinitely from their junction, as the topological invariants are calculated for infinite armchair graphene nanoribbons (AGNRs). The system has a very small energy gap compared to the hopping parameter. Though [15] have demonstrated the stability of such states under perturbation, the extent to which these SPT states remain low energy, as well as localized, in the strongly interacting regime is an open question, especially since any practical implementation of these hybrid systems will be finite in extent, or perhaps in a repeating lattice.

In this paper we address the question of finite volume directly by investigating the *periodic* 7/9- and 13/15-hybrid nanoribbons in two distinct non-perturbative regimes. The term *finite volume* here refers to the fact that the distance between each junction is finite in length due to the systems' periodicity. The first non-perturbative regime we consider is the standard Hubbard model applied to these systems at the electrically neutral, half-filling case. Here we perform quantum Monte Carlo (QMC) simulations for various values of the onsite coupling  $U$  that include the strongly interacting regime. In the second regime we consider the so-called symmetric line limit [19, 21], where we introduce a nearest neighbor superconducting pairing term  $\Delta$  to the Hubbard model but with equal weight as the hopping term  $t$ . In this limit the single-particle spectrum and wavefunctions, when expressed in a Majorana basis, can be determined for any value of the Hubbard onsite interaction  $U$ . In both cases we observe that the energy of the localized state depends strongly on the coupling  $U$ . However, it still remains the lowest energy state of the system. Further, we find that under certain conditions the localization of these states at the junction persists.

Our paper is organized as follows. In the Sect. 3.2 we describe our 7/9 and 13/15 hybrid lattice geometries. We explicitly show the 7/9 spectrum in the tight-binding, or non-interacting, limit; the 13/15 spectrum is very similar in nature. We then introduce a Hubbard onsite interaction  $U$  in Sect. 3.3 and show results of our QMC simulations for select values of  $U$ . In Sect. 3.4 we consider the symmetric line limit by adding a nearest neighbor superconducting term  $\Delta$  of equal magnitude to the hopping term. We demonstrate how this system can be solved directly for any value of  $U$  and show the dependence of the energy and wavefunction of the localized state on  $U$  for the 7/9 case. These localized states on opposing sublattices, or chiralities, have a potential connection to domain-wall fermions formulated in lattice gauge theories in 4+1 dimensions [22, 23]. We comment on this potential connection in Sect. 3.5. We recapitulate in Sect. 3.6.

### 3.2 Geometry of the periodic hybrid nanoribbon

Unit cells in such AGNRs are defined by their terminations i.e. shapes of their edges. In [15] four distinct types of unit cells were defined. Based on inversion and mirror symmetries, as well as the width of ribbons, it was been shown that such systems have an associated conserved quantity, the so-called  $Z_2$  topological invariant, that can take the values 0 or 1. The interface of two materials with distinct topological invariants can support surface modes [24]. Since the existence of these modes depend solely on the topological factors, they should remain even under the presence of interactions, given that these interactions do not change the invariants themselves. The two examples used in this paper are the 7/9- and 13/15-hybrid nanoribbons, where parts of the ribbons with lesser width have topological invariant  $Z_2 = 0$ , while the parts with greater width have invariant  $Z_2 = 1$  [15]. The 7/9 system has recently been experimentally engineered [16, 17].

Both systems are shown in Fig. 3.1. In both cases the figure depicts a single unit cell. The 7/9 (13/15) has  $N = 132$  (228) total lattice sites and is composed of six hexagonal units lengthwise for the lesser AGNR part, and 10 hexagons lengthwise for the greater AGNR part. In terms of the lattice spacing  $a$  between sites, the entire length of the unit cell is  $L = 24a$ . The system is bipartite, meaning we can divide the lattice into two independent sublattices, which we label one as consisting of A sites, and the other B sites. We apply periodic boundary conditions at the ends so that the unit cell shown in Fig. 3.1 repeats itself.

Under the tight-binding approximation, or equivalently the non-interacting limit, we have

$$H_0 = -t \sum_{\langle i,j \rangle, \sigma} a_{i\sigma}^\dagger a_{j\sigma} + h.c. , \quad (3.1)$$

where  $t$  is the hopping parameter<sup>1</sup>,  $a_j^\dagger$  ( $a_j$ ) is the fermionic creation (annihilation) operator at lattice site  $j$ ,  $\sigma$  the spin,  $h.c.$  stands for Hermitian conjugate, and the sum is over all nearest neighbors  $\langle i, j \rangle$ . As the Hamiltonian is quadratic in the number of creation and annihilation operators, the single particle dispersion as a function of longitudinal momentum  $k_x$  can be easily determined in this limit, which we show for the 7/9 case in Fig. 3.2. Note that the dispersion is the same for both spins. The number of bands shown in Fig. 3.2 corresponds to the number of lattice sites in the unit cell (132 for the 7/9 case). Aside from having more upper and lower bands due to the larger number of unit cell lattice sites, the dispersion for the 13/15 case is qualitatively similar to the 7/9 case. Of

<sup>1</sup> For the tight-binding description of graphene,  $t \sim 2.7$  eV [25]

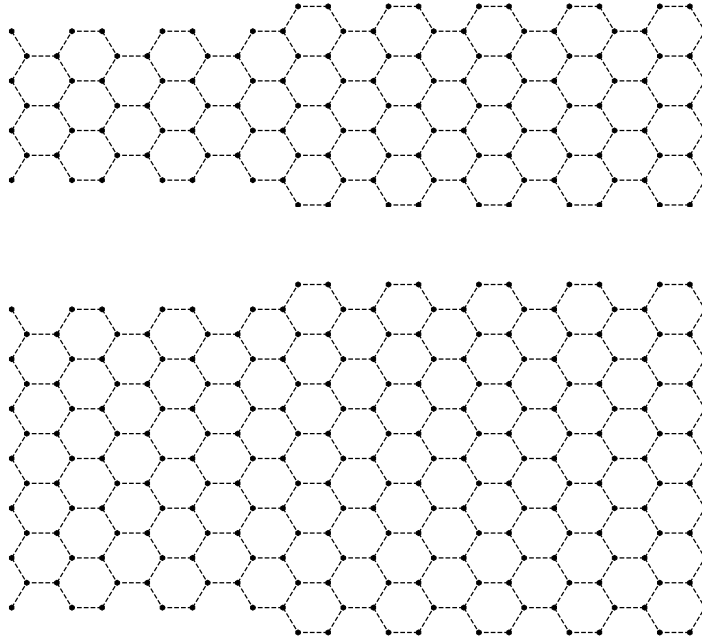


Figure 3.1: Single unit cell of the 7/9 (top) and 13/15 (bottom) hybrid systems considered in this work. The widths are set by the 7 (13) and 9 (15) armchair nanoribbon parts, while the lengths have 6 hexagons and 10 hexagons for the 7 (13) and 9 (15) parts, respectively. Periodic boundary conditions are employed at the ends.

particular interest is the point at  $k_x = 0$  where there seems to be an apparent level crossing at  $E/t = 0$ , denoted as a red point in the main plot in Fig. 3.2. In fact, upon closer inspection as shown in the inset of Fig. 3.2, there is *no* level crossing at this point since it consists of two states with energies  $E/t = \pm 0.0015996$ . For the 13/15 case there is also an avoided level-crossing and the corresponding energies are  $E/t = \pm 0.0090408$ . In Fig. 3.3 we show the wavefunction densities,  $\rho(x) = |\psi(x)|^2$ , for each lattice site  $x$  on an extended hybrid system for these states on these two geometries. These densities are the same for either positive or negative energy solutions. The localization of the states at the junctions is apparent in this figure. Further, the localization is confined to specific sublattices denoted by the red and blue colors in Fig. 3.3, and alternates between the different junctions.

In what follows, we assume that the system is electrically neutral and thus half-filled, meaning that all negative energy states are occupied. The Fermi surface of the system then corresponds to zero energy. We thus concentrate on the lowest *unoccupied* single-particle state. In the non-interacting case this corresponds to the state denoted by the red dot in the inset of Fig. 3.2. In the remainder of the paper we loosely refer to this state as the localized state, though it remains to be seen if the state remains localized in the presence of interactions and within a finite volume.

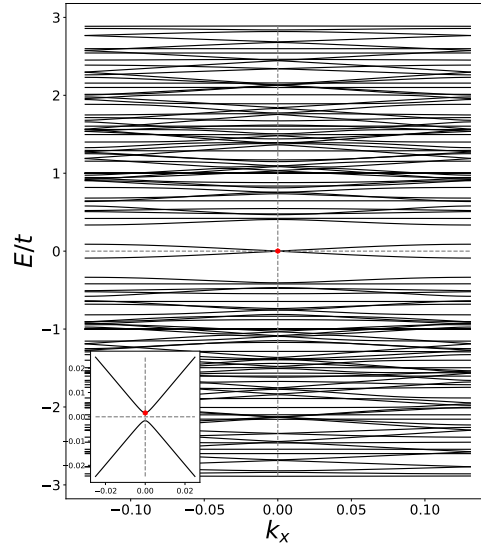


Figure 3.2: Non-interacting dispersion of the 7/9 hybrid ribbon. The inset shows the avoided level crossing near the Fermi surface at  $k_x = 0$ .  $k_x$  is expressed in units of the inverse length  $L^{-1}$  with  $L = 24a$  being the unit cell length and  $a$  the lattice spacing. The dispersion for the 13/15 system has more upper and lower bands but is qualitatively similar in structure.

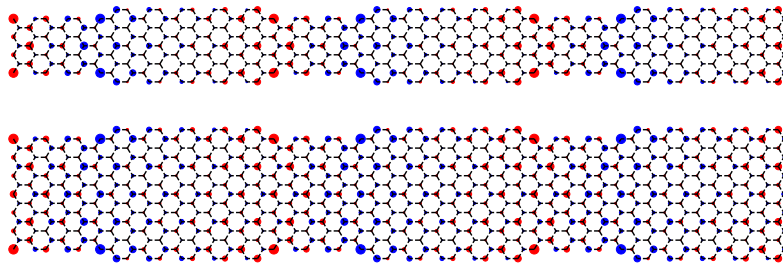


Figure 3.3: Non-interacting single-particle wavefunction densities for the 7/9 (above) and 13/15 (below) hybrid ribbons. The 7/9 and 13/15 configurations have non-interacting energies  $E/t = 0.0015996$  and  $0.0090408$ , respectively. The size of the circles is proportional to the density and the color denotes the two sublattices, red = A sites, blue = B sites.

### 3.3 QMC calculations of the Hubbard Model

We now include a Hubbard onsite interaction,

$$H = -t \sum_{\langle i,j \rangle, \sigma} \left( a_{i\sigma}^\dagger a_{j\sigma} + h.c. \right) + U \sum_x \left( n_{x\uparrow} - \frac{1}{2} \right) \left( n_{x\downarrow} - \frac{1}{2} \right), \quad (3.2)$$

where  $n_{x\uparrow} = a_{x\uparrow}^\dagger a_{x\uparrow}$  is the number operator for spin up fermions at site  $x$  and similarly for spin down fermions. The form of the interaction ensures that the system remains at half-filling for any value of  $U$ . In what follows, we assume that all stated values of  $U$  and  $\beta$  are expressed in units of the hopping parameter  $t$ , i.e. “ $U$ ” =  $U/t$ , “ $\beta$ ” =  $t\beta$ . All derived quantities, such as energies, are then expressed in units of  $t$ . Without loss of generality, this is equivalent to setting  $t = 1$  in Eq. (3.2) for our simulations.

Note that the onsite interaction is quartic in the number of creation and annihilation operators, and therefore no direct diagonalization is possible. Therefore we use QMC simulations to investigate the hybrid systems for values of the onsite interaction  $U$  corresponding to the strongly coupled regime. Our formalism for performing QMC simulations of low-dimensional Hubbard systems have been described in detail in [26–28]. Here we just point out some salient features pertinent to this work.

To extract the quasi-particle energies we calculate momentum correlators as a function of time,

$$C_k(\tau) \equiv \langle a_k(\tau) a_k^\dagger(0) \rangle = \frac{1}{Z} \text{Tr} \left[ a_k(\tau) a_k^\dagger(0) e^{-\beta H} \right], \quad (3.3)$$

where  $\beta$  represents an inverse temperature and  $k = (k_x, \kappa)$  is a momentum index corresponding to the state. The time  $\tau \in [0, \beta)$ , and in our simulations we discretize this variable into  $N_t$  timeslices. We use  $N_t = 64, 80$  and  $96$  in our simulations with  $\beta = 8, 10$ , and  $12$ , respectively, for the  $7/9$  system. For the  $13/15$  system we only investigate with  $(N_t, \beta) = (64, 8)$ . The variable  $\kappa$  is an index corresponding to one of the possible  $N = 132$  ( $228$ ) states of the  $7/9$  ( $13/15$ ) system for a given  $k_x$ . We choose  $\kappa$  to correspond to the state with the lowest possible positive energy. Fig. 3.4 shows all  $k_x = 0$  correlators at the non-interacting  $U = 0$  case and  $\beta = 8$  for the  $7/9$  system. A spectral decomposition of the expression in Eq. (3.3), as is done in App. C.1, shows that these correlators have an exponential dependence in time,  $\sim e^{-E_k \tau}$ , where their arguments correspond to the non-interacting energies of the system at  $k_x = 0$ . These energies correspond to both the positive and negative points that occur at  $k_x = 0$  in Fig. 3.2. In the presence of interactions  $U \neq 0$ , and within a finite inverse temperature  $\beta$ , the correlators will have a more complicated dependence on  $\tau$  due to thermal contamination with excited states and backwards-propagating states. However, these effects are usually fleeting since the dependence on the excited states is exponentially suppressed. Therefore, as long as  $\tau \gg 1$  but  $\tau < \beta$ , the correlators will recover an exponential dependence but now with fully interacting energies in their arguments. One can thus extract the fully interacting energies by analyzing the exponential behavior of the correlators in this regime. We stress that the correlator in (3.3) and the energy  $E_k$  dictating its exponential decay are not related to any response of the system due to some external probe. The energy  $E_k$  represents the fully-interacting single-particle eigen-energy of the Hamiltonian given in (3.2).<sup>2</sup>

Special care must be taken when dealing with correlators that represent states with very small energies,  $E\beta \ll 1$ , as is the case in our situation. Here the backwards-propagating states can provide a

<sup>2</sup> In practice the calculation of the correlator in (3.3) requires calculating the inverse of the so-called fermion matrix  $M$  and then analyzing its time-dependence. More details of this method are provided, for example, in [27] and [7].

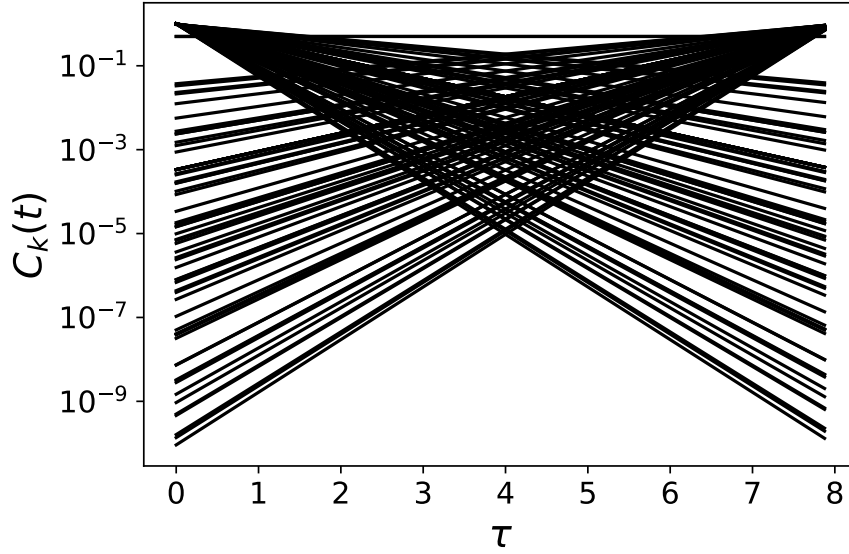


Figure 3.4: All non-interacting correlators at  $k_x = 0$  for the 7/9 system.

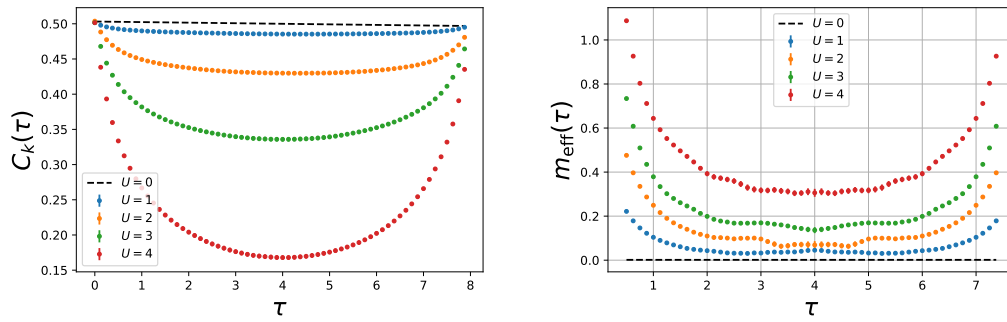


Figure 3.5: Dependence of correlators for the lowest energy localized state (left) and its corresponding effective masses (right) as defined in Eq. (3.5). In both cases the black dashed line corresponds to the non-interacting result.

nearly equally important contribution to the correlator, essentially making the correlator symmetric about the  $\tau = \beta/2$  point. The left panel of Fig. 3.5 shows examples of the dependence of the correlators for the localized state as a function of  $U$ . It is indeed the case that these low-energy correlators cannot be described by a single exponential. We now describe how we extract energies from these correlators.

### 3.3.1 Energy of the localized states

To extract the energies from these correlators, we first take advantage of the particle-hole symmetry of our problem that states that for any energy solution  $E_k$ , there is a corresponding solution with opposite sign,  $-E_k$ . This is also evident from our correlators, where for each correlator that falls off in time as  $C_k^-(\tau) \sim e^{-E_k\tau}$ , there is a growing correlator, corresponding to the energy with opposite sign, of the form  $C_k^+(\tau) \sim e^{E_k(\tau-\beta)}$ . We average these two correlators.

$$C_k^{sym}(\tau) = \frac{1}{2} (C_k^-(\tau) + C_k^+(\tau)) , \quad (3.4)$$

to effectively make a cosh function of the form  $\cosh(E_k(\tau - \beta/2))$  in the region  $\tau \gg 1$  and  $\tau < \beta$ .

As a visual aid to estimating the energies of these correlators, we calculate the so called ‘‘effective mass’’  $m_{eff}(\tau)$ ,

$$m_{eff}(\tau) = \frac{1}{\delta} \cosh^{-1} \left( \frac{C_k^{sym}(\tau - \delta) + C_k^{sym}(\tau + \delta)}{2C_k^{sym}(\tau)} \right) , \quad (3.5)$$

where  $\delta$  is some free parameter. If  $C_k^{sym}(\tau)$  were exactly a cosh function then  $m_{eff}(\tau) = E_k$  for all  $\tau$ . As the cosh behavior is only valid for  $1 \ll t \ll \beta$  we expect that the effective mass to ‘flatten out’ around the region  $\tau = \beta/2$ . The right panel of Fig. 3.5 shows our extracted effective masses for the localized state using  $\delta = 4\beta/N_t$ . As expected the region around  $\tau = \beta/2$  is flat and corresponds to the interacting energy  $E_k/t$ . We stress, however, that these effective masses are only used as a visual aid for estimating the energies.

To actually obtain the energies, we instead fit directly the correlator  $C_k^{sym}(\tau)$ . We show our extracted energies for values of  $U \in [1, 2, 3, 4]$  and  $\beta \in [8, 10, 12]$  in Fig. 3.6. Our fits are performed within a finite window around the  $\tau = \beta/2$  point and are done under the bootstrap procedure to obtain uncertainties. Looking at Fig. 3.6 we see a growing dependence on the energy of the localized state as  $U$  increases. We attribute this dependence to the finite volume of the system, both spatially and temporally, since within such an environment the state is no longer protected by SPT. Still, in all cases we examined we found that the energy of the localized state remained the lowest, despite its apparent dependence on  $U$ .

### 3.3.2 Wavefunction densities of the localized state

We can also extract the site-dependent densities of the states in our QMC simulations, which in turn allow us to demonstrate localization of the states visually. A detailed explanation of our calculation is given in App. C.1, and we provide only a cursory description here.

Instead of the momentum correlators calculated in Eq. (3.3), we instead consider the half-momentum, half-spatial correlators

$$C_k(x, \tau) \equiv \langle a_x(\tau) a_k^\dagger(0) \rangle = \frac{1}{Z} \text{Tr} \left[ a_x(\tau) a_k^\dagger(0) e^{-\beta H} \right] . \quad (3.6)$$

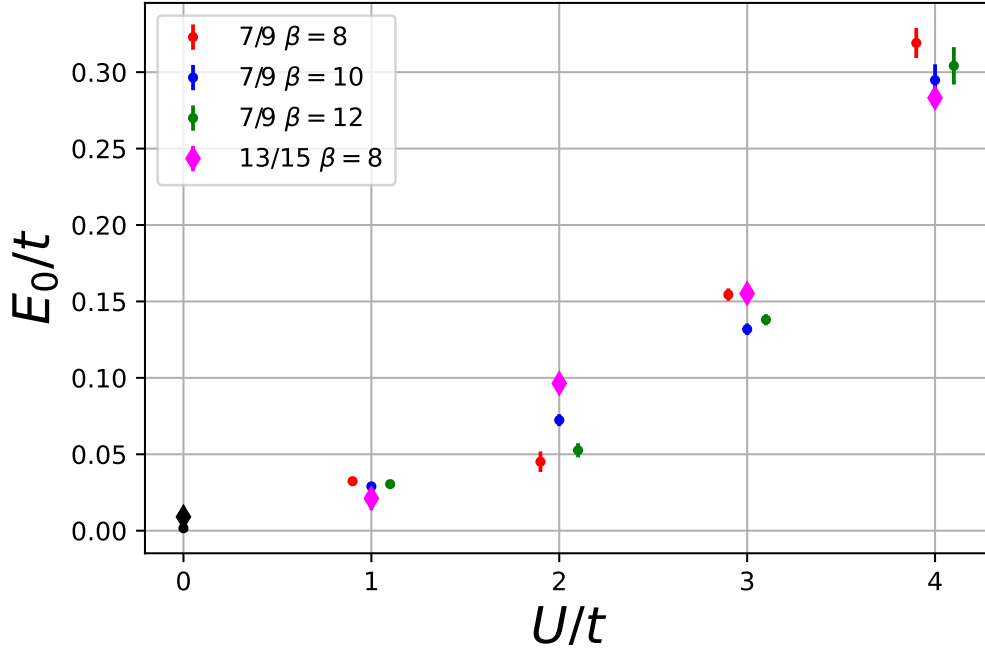


Figure 3.6: Energy  $E_0$  of the lowest state as a function of onsite interaction  $U$  obtained from QMC calculations for the 7/9 (dots) and 13/15 (diamonds) systems. The 7/9 simulations were performed with three different values of  $\beta$ , where  $\beta = 8$  (12) results are slightly shifted to the left (right) on the x-axis so as to make the points more easily differentiable. Only  $\beta = 8$  was used for the 13/15 system. The black points at  $U = 0$  are the non-interacting results.

The effective density  $\rho_k(x, \tau)$  for the state  $k$  at each lattice site  $x$  is given by

$$\rho_k(x, \tau) \equiv \frac{|C_k(x, \tau)|^2}{\sum_y |C_k(y, \tau)|^2}. \quad (3.7)$$

where the sum in the denominator of the right-hand side is over all lattice sites in the unit cell. As was the case with the effective masses, we extract the densities by looking at the region around  $\tau = \beta/2$  where the effective density is flat.

We plot these densities for the localized state in Fig. 3.7 for different values of  $U$  for the 7/9 system. We find that the changes in the densities vary only slightly as a function of  $U$  and are practically indistinguishable in Fig. 3.7. We see similar behavior for the 13/15 system. In Fig. 3.8 we concentrate on a specific lattice site of the 7/9 system, the bottom- and left-most site of the unit cell, and show how the density at this site varies as  $U$  increases. When  $U = 0$  this site is one of four A sites that has a maximum probability for occupation compared to other A sites. With increasing  $U$  this density diminishes, but still remains the largest. We find a similar behavior with other high-density sites on both 7/9 and 13/15 systems. For sites with initially low probabilities at  $U = 0$ , their densities slightly grow with increasing  $U$ . However, the changes are too small to drastically change the general electron

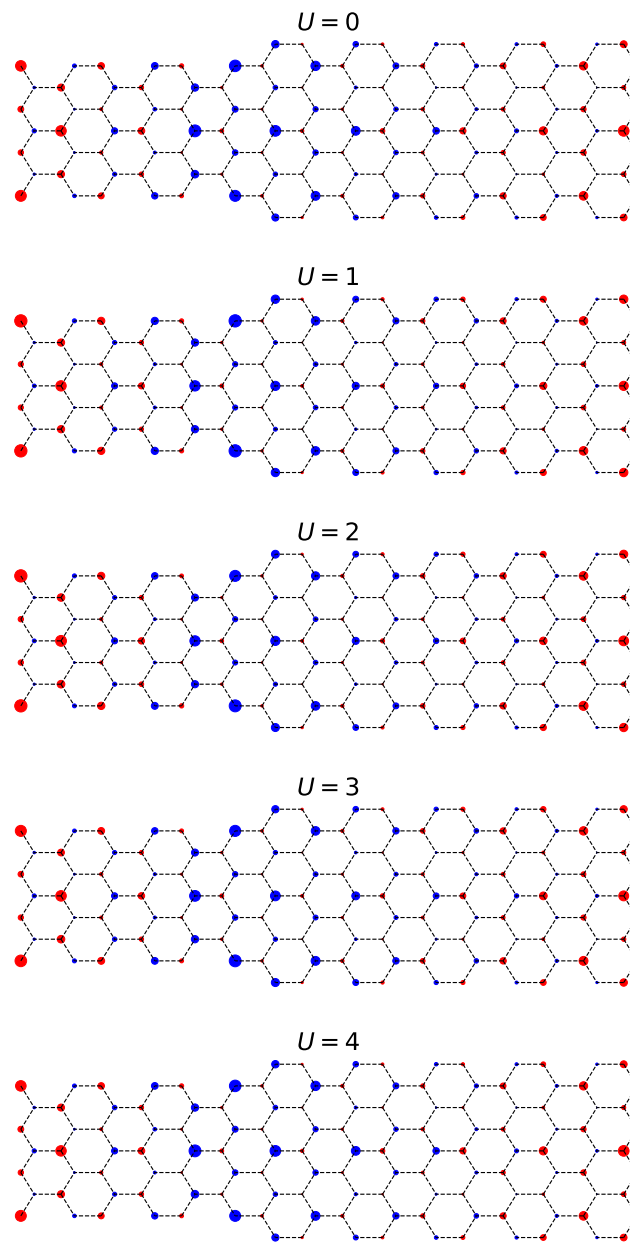


Figure 3.7: Density profile of lowest  $k_x = 0$  energy state for different values  $U$ , compared with the non-interacting case (i.e.  $U = 0$ ).

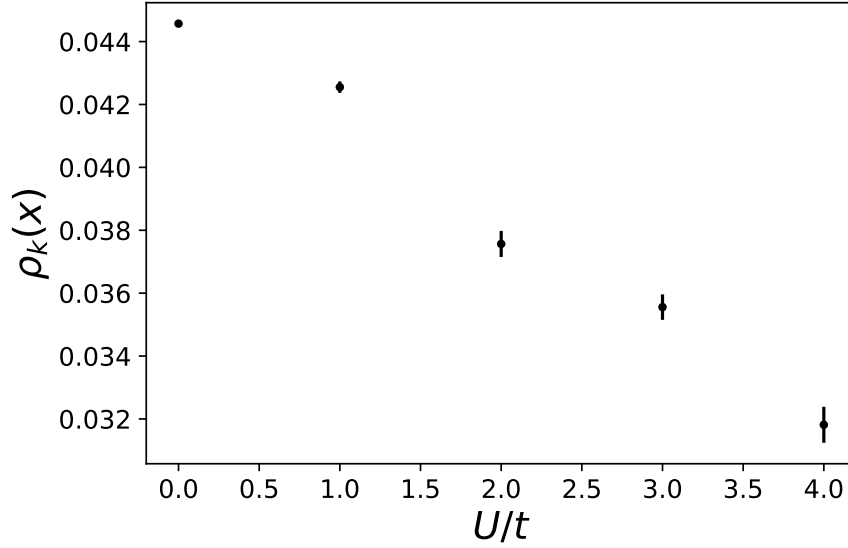


Figure 3.8: Wavefunction density  $\rho_k(x)$  of the bottom- and left-most lattice site of our unit cell hybrid AGNR as a function of  $U$ .

occupation profile. Thus the localization of this state persists as  $U$  grows large, despite its growing energy.

Our results definitely show the strong dependence of the energy on  $U$  within a finite volume. The localization, however, is robust and persists in such environments. A more definitive QMC investigation of this state would require repeated calculations of this system with more values of  $\beta$  and number of timeslices  $N_t$ , as well as more unit cells, allowing for extrapolations to zero-temperature, to the continuum limit, and to the infinite volume (length), respectively. We are actively pursuing this line of research.

Still, the fact that these states remain localized for large values of  $U$  within such an extreme finite volume bodes well for their potential utilization in advanced electronics, which by construction are finite in extent.

### 3.4 The symmetric-line limit

We now consider the inclusion of a nearest-neighbor superconducting pairing term  $\Delta$  to the Hamiltonian,

$$H_0 = - \sum_{\langle i,j \rangle, \sigma} \left( t a_{i\sigma}^\dagger a_{j\sigma} + \Delta a_{i\sigma}^\dagger a_{j\sigma}^\dagger + \text{h.c.} \right) + U \sum_x \left( n_{x\uparrow} - \frac{1}{2} \right) \left( n_{x\downarrow} - \frac{1}{2} \right). \quad (3.8)$$

The pairing term has the same symmetry properties as the hopping term, and in particular, the Hamiltonian remains invariant under time reversal. Therefore the inclusion of this term does not change the topology of the system.

As described in [19–21], for example, when  $\Delta$  has the same magnitude as the hopping parameter  $t$ ,

the onsite interaction term becomes quadratic in the number of creation and annihilation operators and therefore the spectrum of the system can be obtained by direct diagonalization. We repeat the derivation for our system here. We follow the conventions introduced in [19].

Typically one uses a Bogoliubov-Valatin transformation [29, 30] in theories with pairing terms. However, in this case, with an eye towards the interacting onsite term, we instead perform a canonical transformation to a Majorana basis,

$$\begin{aligned} a_{i\sigma} &= \eta_{i\sigma} + i\gamma_{i\sigma}, & a_{i\sigma}^\dagger &= \eta_{i\sigma} - i\gamma_{i\sigma}, \\ a_{j\sigma} &= \gamma_{j\sigma} + i\eta_{j\sigma}, & a_{j\sigma}^\dagger &= \gamma_{j\sigma} - i\eta_{j\sigma}, \end{aligned} \quad (3.9)$$

where  $i \in A$  sites and  $j \in B$  sites. The Hamiltonian in Eq. (3.8) then becomes

$$H = -2i \sum_{\langle i,j \rangle \sigma} [(\Delta + t) \gamma_{i\sigma} \gamma_{j\sigma} + (\Delta - t) \eta_{i\sigma} \eta_{j\sigma}] - U \sum_{x \in A \& B} (2i\eta_{x\uparrow} \eta_{x\downarrow}) (2i\gamma_{x\uparrow} \gamma_{x\downarrow}). \quad (3.10)$$

We now take the symmetric line limit by setting  $\Delta = t$ , thereby eliminating the  $\eta$  Majorana fermions from the kinetic energy of the Hamiltonian above,

$$H_{\text{sym}} = -4it \sum_{\langle i,j \rangle \sigma} \gamma_{i\sigma} \gamma_{j\sigma} - U \sum_{x \in A \& B} (2i\eta_{x\uparrow} \eta_{x\downarrow}) (2i\gamma_{x\uparrow} \gamma_{x\downarrow}). \quad (3.11)$$

Notice that the  $\gamma$  Majorana fermions have a kinetic term similar to the original tight-binding Hamiltonian of Eq. (3.1), but now with a hopping amplitude  $4t$ . Indeed, when  $U = 0$  the dispersion for this system, when normalized by  $4t$ , is identical to the non-interacting dispersion shown in Fig. 3.2.

Now consider the site-dependent operator  $\hat{d}_j \equiv 2i\eta_{j\uparrow}\eta_{j\downarrow}$ . One has that  $[H_{\text{sym}}, \hat{d}_j] = 0 \forall j$ . Therefore, within Eq. (3.11), the term  $2i\eta_{x\uparrow}\eta_{x\downarrow}$  ( $= \hat{d}_x$ ) can be replaced, in general, by a complex number  $d_x$  (no hat symbol). As can be derived explicitly from (3.9), the Majorana operators  $\eta$  have the property that  $\eta^2 = 1/4$  which implies that  $\hat{d}_x^2 = 1/4$  [31]. Thus we can make the following replacement  $\hat{d}_x \rightarrow d_x = \pm 1/2$  in Eq. (3.11). This gives

$$H_{\text{sym}} = -4it \sum_{\langle i,j \rangle \sigma} \gamma_{i\sigma} \gamma_{j\sigma} - 2iU \sum_{x \in A \& B} d_x (\gamma_{x\uparrow} \gamma_{x\downarrow}). \quad (3.12)$$

The equation above shows that in the symmetric line limit the  $\eta$  Majorana fermions completely decouple from the theory. They provide a zero-energy topological flat band to the to the dispersion, independent of  $U$ , but as argued in [19] these states do not correspond to localized states.

The Hamiltonian in Eq. (3.12) is quadratic in the Majorana operators and therefore can be directly diagonalized once the coefficients  $d_i$  are fixed. In principle, given  $N$  lattice sites, there are  $2^N$  different possible combinations of  $d_i$ , all satisfying the flat band condition for the  $\eta$  Majorana fermions but providing a different spectrum for the  $\gamma$  Majorana fermions. We consider two uniform solutions in this work, the first being the ferromagnetic solution with  $d_i = 1/2 \forall i$  and the other the antiferromagnetic case where  $d_i = 1/2$  for  $i \in A$  sites and  $d_i = -1/2$  for  $i \in B$  sites. Lastly we consider a random configuration where  $d_i = \pm 1/2$  is chosen randomly at each site  $i$ .

Since the discussion above applies to any bipartite lattice, we can directly use it on our systems. In our calculations both 7/9 and 13/15 systems exhibit nearly identical qualitative results. To keep the presentation reasonable we therefore only present results for the 7/9 system and comment on the 13/15

system when appropriate.

### 3.4.1 Ferromagnetic configuration

In this configuration we choose  $d_i = 1/2 \forall i$ . Our results are identical if we instead chose  $d_i = -1/2 \forall i$ . We show the dispersion for this system for select values of  $U$  in Fig. 3.9. In general the dispersion becomes quite dense and the separation between the lowest state and the next excited state diminishes as  $U$  is increased.

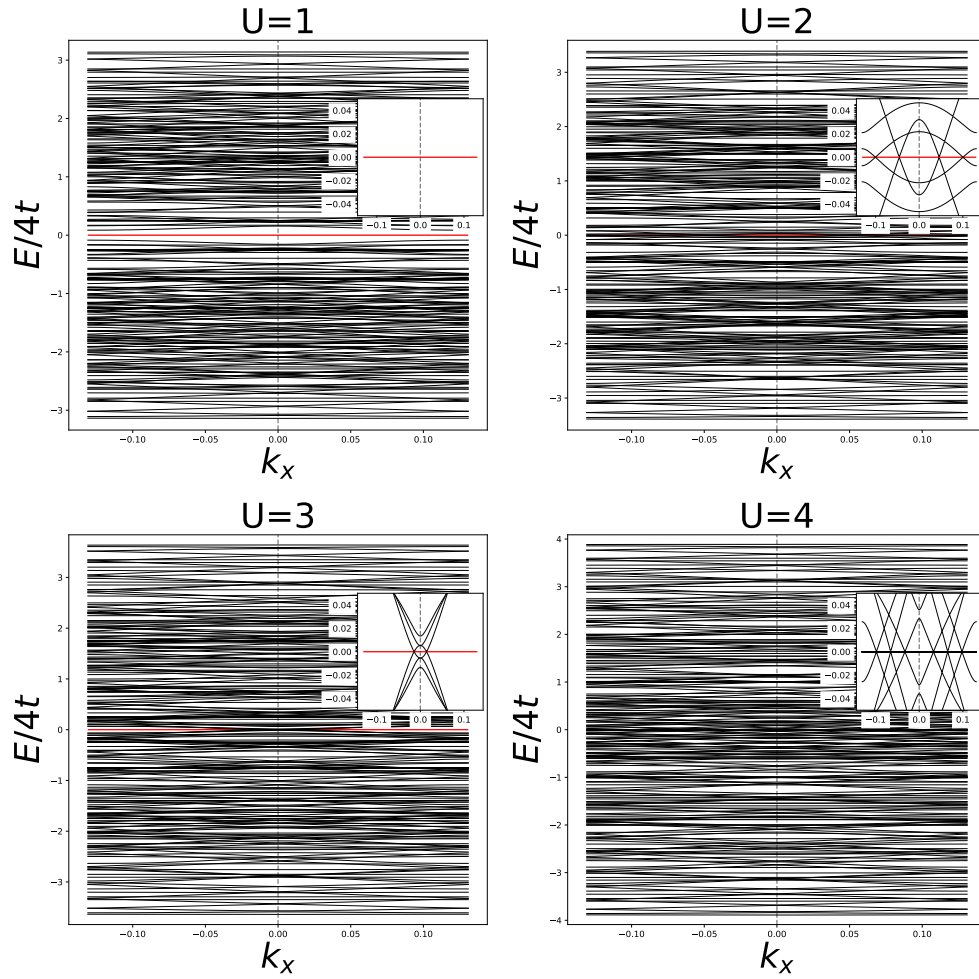


Figure 3.9: Ferromagnetic dispersion in the symmetric line limit for different values of  $U$ . The red horizontal line is the flat band energy for the decoupled  $\eta$  Majorana fermions.

The wavefunction densities for the lowest energy state are shown in Fig. 3.10. We find that this configuration exhibits no localization at  $k_x = 0$  for the large  $U$ s considered here, though we have confirmed that it is perturbatively recovered in the limit  $U \rightarrow 0$ .

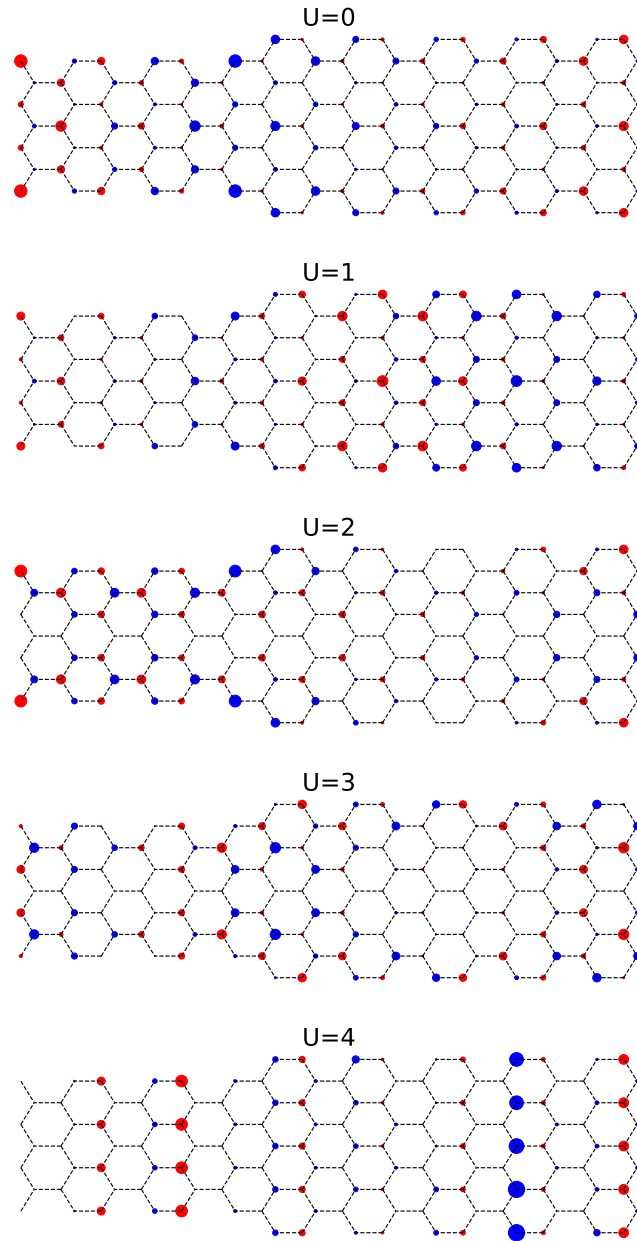


Figure 3.10: Density profile of the lowest  $k_x = 0$  energy state at the symmetric line limit for the ferromagnetic configuration for different values of  $U$ . The result is the same for either spins  $\sigma$ . Non-interacting case corresponds to  $U = 0$ .

Finally, the energy  $E_0$  of the lowest state has a complicated dependence on the interaction term  $U$ , as is shown in Fig. 3.11. This is due to the fact that we consider only the lowest positive energy

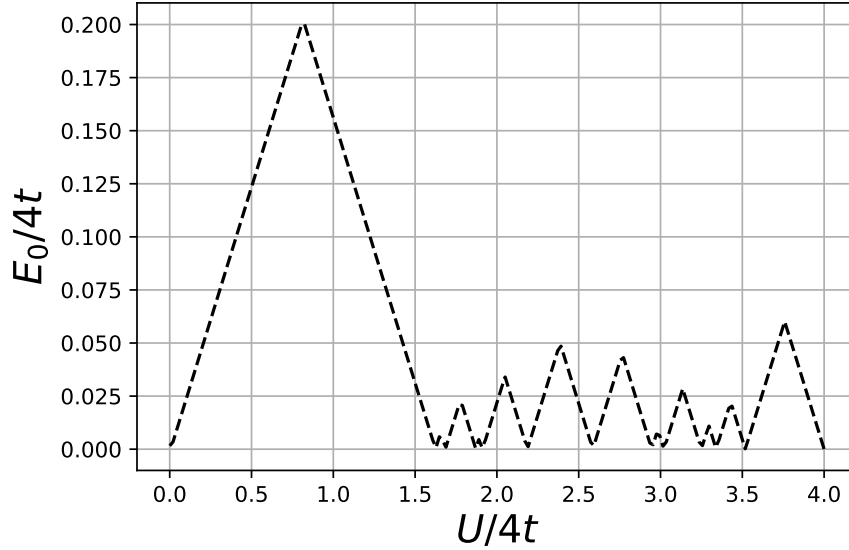


Figure 3.11: Dependence of the lowest positive energy  $E_0$  as a function of  $U$  in the ferromagnetic configuration.

level at  $k_x = 0$ . As  $U$  increases the energy levels from the upper and lower bands come together and eventually cross each other. Before each crossing the minimal energy decreases and after a crossing it begins to increase again. Eventually the lowest energy levels cross  $E_0 = 0$  after which the next highest one takes its place.

### 3.4.2 Antiferromagnetic configuration

Fig. 3.12 shows the dispersion of the hybrid ribbon at the symmetric line limit for select values of  $U > 0$  in the antiferromagnetic configuration. Notice that the lowest positive energy increases with larger  $U$  and forms essentially a flat band solution. Numerically we find a linear dependence of this energy on  $U$ , as shown in Fig. 3.13.

For all  $U$ s investigated, the wavefunction densities of this state does not change and remains exactly the same as that of the non-interacting state shown in Fig. 3.3. Therefore this state remains localized, despite its energy having a linear dependence on  $U$ . We conclude that the flat band that develops for  $U > 0$  is robust and is unaffected by interactions. Unlike the ferromagnetic case, when we increase  $U$  the gap in the antiferromagnetic system increases linearly since no low lying energy levels cross each other and therefore no complicated  $U$  dependence is introduced.

### 3.4.3 Random configuration

To a certain extent a random configuration of  $d_i$ s is similar to the antiferromagnetic configuration in that such a configuration has no long range order. Thus one might expect that the dispersion in the random configuration is similar to the antiferromagnetic case. We find this to be true for values of  $U$  as large as  $U \lesssim 2$ .

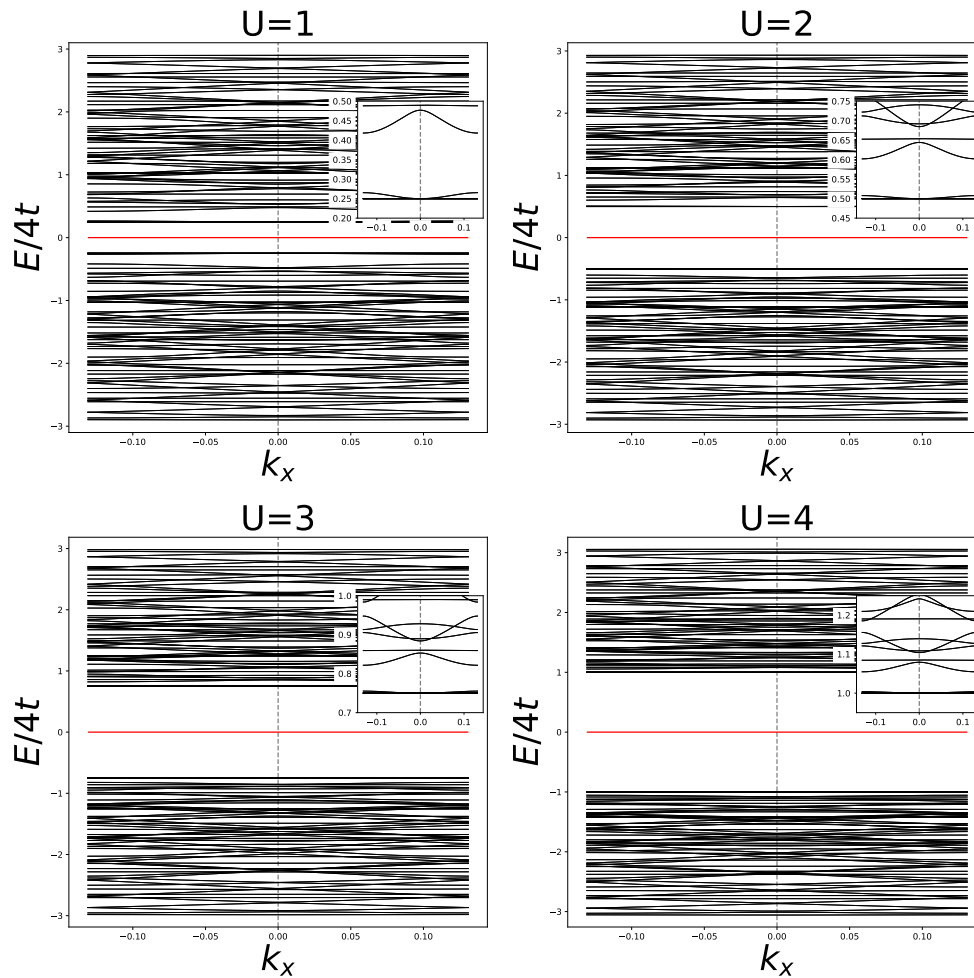


Figure 3.12: Antiferromagnetic dispersion in the symmetric line limit for different values of  $U$ . The red horizontal line is the flat band energy for the decoupled  $\eta$  Majorana fermions.

To see this, we first show in Fig. 3.14 the dispersion for different values  $U$  using a single randomly sampled configuration in each case. Not surprisingly, the dispersions become progressively dense and chaotic with increasing  $U$ . To construct the accompanying wavefunction densities, we calculate 100 random configurations for each value of  $U$  and average their wavefunction densities, the results of which are shown in Fig. 3.15. In this case the localization of the lowest state can be seen for  $U = 1$  and  $U = 2$ . However, for larger  $U$  any analogies of the dispersion with the antiferromagnetic configuration is lost and localization is no longer present.

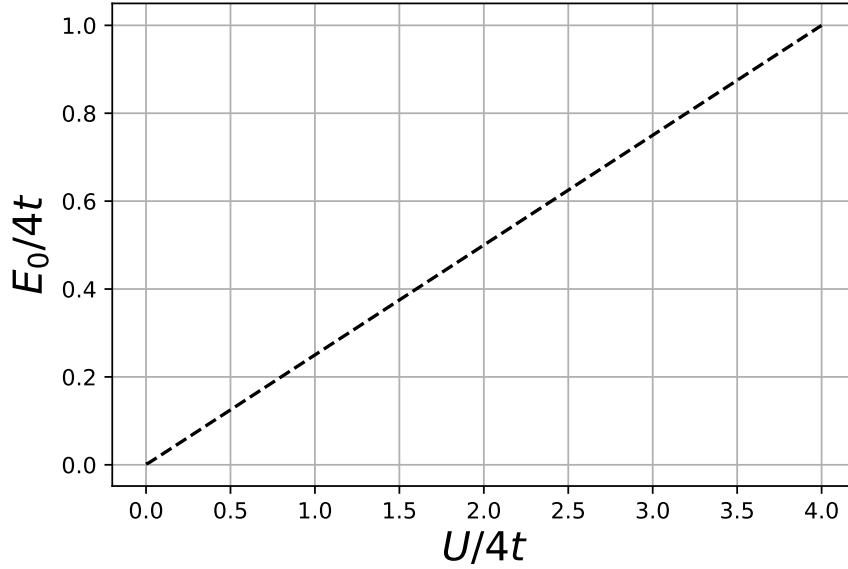


Figure 3.13: Dependence of the lowest positive energy  $E_0$  as a function of  $U$  in the antiferromagnetic configuration for 7/9 ribbon. The 13/15 system presents the same linear relation.

### 3.5 Analogy with Domain-wall fermions

Domain wall fermions were formulated originally by Kaplan [22] as a way to circumvent the so-called Nielsen-Ninomiya no-go theorem [32] in lattice gauge theory, which states that the number of left-handed chiral fermions  $\psi_L$  must equal the number of right-handed chiral fermions  $\psi_R$  in any discretized, local, Hermitian, and translationally invariant field theory. Kaplan's formulation of domain wall fermions introduced an extra bulk dimension on top of the four spacetime dimensions, whereby a single fermion of one chirality was localized on the 4-d spacetime manifold (the domain wall where all the relevant physics occurs) of the 5-d space, and another fermion of opposite chirality was constrained on the opposite 4-d domain wall. In this manner, lattice gauge calculations utilizing domain wall fermions could simulate, in principle, an odd number of fermions with specific chirality by concentrating on one of the 4-d domain wall manifolds without violating the Nielsen-Ninomiya no-go theorem. Chiral symmetry is still violated since the Ginsburg-Wilson equation remains non-zero in the bulk. This manifests itself as a small overlap of the fermion wavefunctions in the bulk, which in turn leads to a residual mass  $\mu$  for each fermion that mixes their chiralities,  $\mu(\bar{\psi}_L\psi_R + \bar{\psi}_R\psi_L)$ . As the bulk direction is extended, the overlap reduces leading to a vanishingly small residual mass and therefore a vanishing chiral-symmetry violation. Kaplan's formulation is actually valid for any theory in  $2n + 1$  dimensions, where  $2n$  represents the spacetime dimension and the extra dimension represents the bulk.

Chiral symmetry breaking has been discussed in the context of the 2d graphene hexagonal lattice (see, e.g., [33, 34]). Here chiral symmetry manifests itself as a sublattice symmetry between the A and B sites and originates from an underlying time-reversal and charge-conjugate symmetry [35, 36]. The low-energy "Dirac" modes of the system can be described by an effective relativistic field theory in

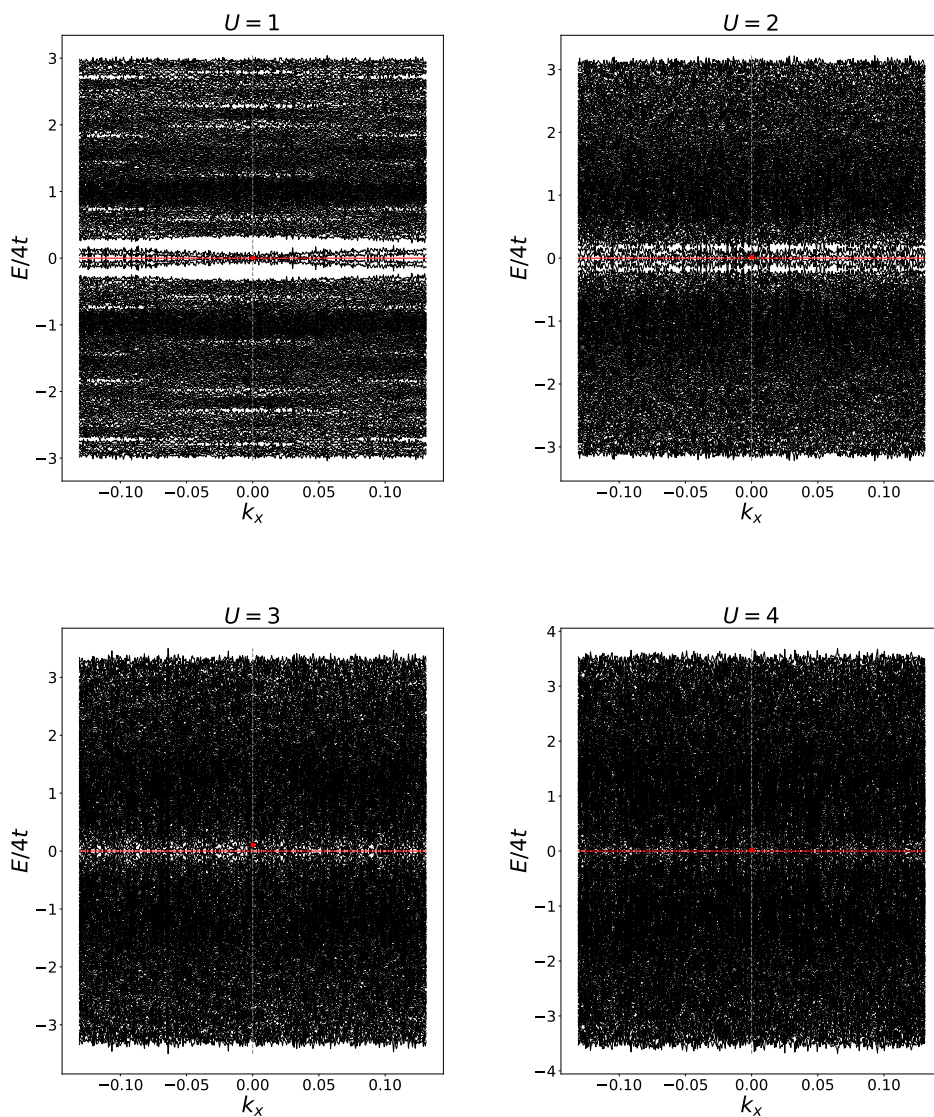


Figure 3.14: Dispersion at the symmetric line limit using random configurations.

2+1 dimensions. As argued in [33], the formation of a gap in these modes is equivalent to a staggered mass [37] for the fermions that breaks the sublattice symmetry.

In our ribbons we may treat one of the spatial dimensions as the manifold, or junction, while the other remaining spatial dimension between the junctions as the bulk. If we concentrate on just the low-energy localized state of our system and describe it within some effective field theory, then the shift away from zero energy can also be represented as a staggered mass that presumably depends on the overlap of the wavefunctions of the two chiral edge states within the bulk, and thus should vanish

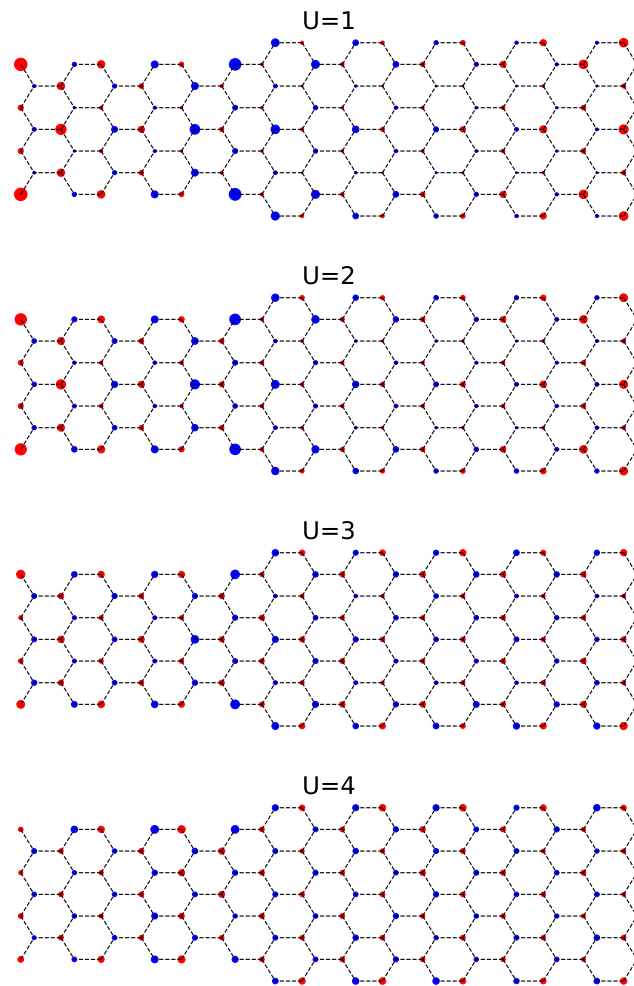


Figure 3.15: Density profile of the lowest  $k_x = 0$  energy state at the symmetric line limit using random configurations for different values of  $U$ . Localization can be seen in the cases with  $U = 1$  and 2, but is lost for higher values.

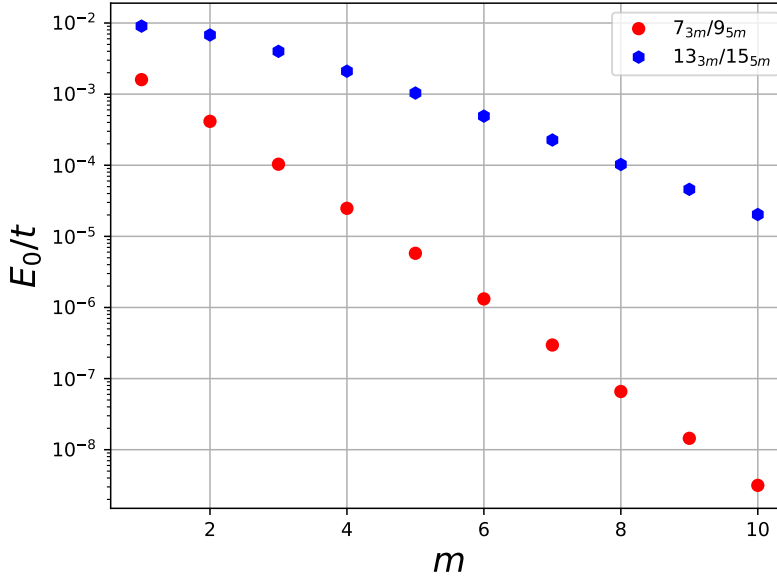


Figure 3.16: The non-interacting energy of the localized state for both 7/9 and 13/15 ribbons as the bulk direction between junctions is extended in multiples of  $m$ . The width between the junctions is  $3m$  ( $5m$ ) for the lesser (greater) ribbon, corresponding to  $6m$  ( $10m$ ) hexagonal units. When  $m = 1$  we have the unit cells depicted in Fig. 3.1.

as the bulk direction is extended. We find this to indeed be the case in the non-interacting limit as we show in Fig. 3.16. Here we show the energy of the localized state for both 7/9 and 13/15 ribbons as we extend the bulk direction. There is a clear exponential decay in the energy. Thus the localized states on opposite A/B sublattices at the junctions of the topologically distinct ribbons offer a potential physical realization of Kaplan's domain wall fermions, albeit in reduced dimensions. A formal description of these chiral states within an effective field theory context is something we are currently developing.

### 3.6 Conclusions

Localized states at the junction of topologically distinct nanoribbons offer promising avenues in constructing advanced electronics and potentially provide a means for topological, fault-tolerant quantum computing. Central to this idea is the stability of such states not just to slight perturbations, but to large electron correlation effects. In principle SPT provides this stability, but only in the limit of infinitely long ribbons where SPT invariance is manifest. In a finite volume this protection is not guaranteed, and as such, the stability of such states comes into question when electron correlations become large.

In this paper we investigated the stability of the (nearly) zero-mode localized states in a finite 7/9 and 13/15 hybrid nanoribbons with periodic boundary conditions under the influence of temperature and electron-electron interactions. We investigated two scenarios, one where we considered just

the Hubbard model at half-filling and performed QMC simulations for a range of  $U$  that included the strongly interacting regime. We then introduced to the Hubbard model a nearest neighbor superconducting term whose parameter was tuned to the so called symmetric line limit. In this limit, when transforming to a Majorana basis, we could calculate the single-particle spectrum and wavefunctions exactly for any value of  $U$ . Provided that we concentrate on the antiferromagnetic configuration in the latter case, we found that in both cases the energy of the localized states increased with larger  $U$ , but remained the lowest energy state regardless. More importantly, we found that the localization of the states persisted at the junctions, indicating that this feature is robustly maintained in the strongly interacting, finite volume regime. Though by no means a proof, our observations of persistence of localization in both 7/9 and 13/15 hybrid geometries suggests that such effects are generic to other hybrid geometries that support localization. But this remains to be seen. These findings enhance the possibility of using these systems for manufacturing novel electronic devices which are inherently finite in volume.

**TL thanks Evan Berkowitz, Andrei Kryjevski, Johann Ostmeyer for enlightening discussions related to this work. This work was supported in part by the Chinese Academy of Sciences (CAS) President's International Fellowship Initiative (PIFI) (Grant No. 2018DM0034) and Volkswagen Stiftung (Grant No. 93562).**

---

## Effective theory for graphene nanoribbons with junctions

---

This chapter is based on [3]

**Effective theory for graphene nanoribbons with junctions** J. Ostmeyer, L. Razmadze, E. Berkowitz, T. Luu and U. Meißner, Phys. Rev. B **109**, 195135 (2024) [[arXiv:cond-mat/2401.04715](https://arxiv.org/abs/2401.04715)]

In prior studies, the junction states of armchair ribbons and their dependence on the on-site Hubbard interaction were investigated. It was previously claimed that the low-energy mode in this system arises from the differing topological  $\mathbb{Z}_2$  charges of two ribbons [15]. However, examples exist where localization persists even in the absence of any variation in the topological invariant between the two ribbons. A simpler explanation can be derived by analyzing the long-wavelength limit of a straightforward tight-binding model applied to the ribbons. In accordance with [15], only ribbons whose widths differ by 2 were considered. Nevertheless, it is reasonable to extend the analysis to hybrid ribbons composed of armchair graphene nanoribbons (AGNRs) of arbitrary widths.

For a ribbon of a given width  $N$ , the Hamiltonian is decomposed into  $N$  sectors, each described by a massive Dirac equation:

$$(1 + j)\sigma_x - j\frac{3}{2}ka\sigma_y, \quad (4.1)$$

where  $j = 2 \cos\left(\frac{\pi}{N+1}m\right)$  with  $m = 1, \dots, N$ . For  $j = -1$ —which occurs only for widths  $N = 3m + 2$ —the mass term vanishes, and zero modes propagate within the ribbon. When such a ribbon is joined with one that cannot support zero modes or massless excitations, the propagation decays gradually, forming an evanescent wave-like pattern. When two ribbons with different widths are joined, neither of which supports zero modes, the propagation decays on both sides of the junction, forming a sharply localized peak independent of topological considerations. Conversely, if "garlands" of short ribbons of alternating widths are constructed, different localization behavior emerges. Interleaving two ribbon sections, such that only one supports zero-mass excitations, causes the wavefunction to predominantly localize within the ribbon supporting zero modes, but this localization is distributed over the entire section rather than forming a sharp peak. Furthermore, in scenarios where two infinite ribbons are connected by a short segment of width  $N = 3m + 2$ , the wavefunction becomes effectively trapped, resulting in strong localization within a small region of the system. This configuration offers a novel method for engineering quantum dots.

In this work, an *effective theory* for hybrid graphene nanoribbons was derived. This study suggests an alternative explanation different from the  $\mathbb{Z}_2$  topological invariant argument, highlighting that the localization of junction states can be explained entirely without topology. Instead, a detailed tight-binding approach was used to predict the energy gap and spatial characteristics of localized states across a wide range of hybrid ribbon geometries.

Two distinct types of localized states were identified: the familiar, sharply defined *Fuji* localizations and a newly discovered type, referred to as *Kilimanjaro* localizations, which are smeared over an extended segment of the hybrid ribbon. For *Fuji* localizations, we found that strong localization at symmetric junctions occurs only when the width of the narrower ribbon  $N$  satisfies  $N \pmod{3} = 1$ . In contrast, edge-aligned junctions, regardless of the relative widths of the ribbons, do not support strong localization. This nuanced behavior underscores the limitations of the traditional topological framework and demonstrates the importance of geometry and symmetry in the formation of localized states.

The discovery of *Kilimanjaro* localizations revealed an important new class of states that differ from the typical evanescent wave solutions. These states form a broader, wave-like distribution and are more sensitive to the junction's symmetry properties. Unlike *Fuji* localizations, which are highly concentrated near the junction, *Kilimanjaro* localizations spread over a finite segment, indicating a different mechanism for state formation that extends the concept of topological protection.

The implications of these findings extend beyond theoretical interest. The persistence of localized

states in hybrid ribbons despite changes in their topological invariant suggests new avenues for the design of robust, fault-tolerant qubits for quantum computing applications. By carefully engineering the junction geometry and tuning the interaction strengths, it may be possible to construct nanoribbon-based quantum dots with tailored energy spectra and enhanced stability against decoherence.

To further refine the description of these junction states, the effective tight-binding model can be extended to include staggered mass term, that can capture additional physical effects, such as Hubbard interaction. Specifically, introducing a staggered mass term  $m_s$  in analogy to the Su-Schrieffer-Heeger (SSH) model increases the system's minimal energy to  $\sqrt{(t_N - t_{N+2})^2 + m_s^2}$ . Since the effective hopping strengths  $t_N$  and  $t_{N+2}$  are determined by the ribbon gap, the staggered mass term modifies the energy without altering the underlying effective hopping values. It is therefore possible to use simulate Hubbard interactions for various interaction strengths and fit the staggered mass term to the resulting energies to capture the  $U$  dependence of the model.

## 4.1 Introduction

The ability to engineer hybrid nanoribbons [16, 17] has opened up the possibility of using such systems to manufacture quantum dots [18] and other advanced electronic devices. A central aspect that drives the usefulness of these systems is their ability to support localized electronic states that can be achieved through careful doping of the ribbons. Various models of nanoribbons exhibit edge-state localization with a topological origin [14, 19, 20, 38]. In [15] it was argued that completely localized low-energy states occur at the junction of two armchair graphene nanoribbons (AGNRs) that are topologically distinct, forming so-called symmetry-protected topological edge states that should depend only on the geometrical, or topological, aspects of the system and not on the details of any interaction. These states have electrons confined not only to the edge of the ribbon, but concentrated around the junctions.

Ref. [2] confirmed that this localization is robust against the inclusion of an onsite Hubbard interaction via non-perturbative calculations. The localization of states for the 7/9 and 13/15 hybrid nanoribbon systems persisted for a wide range of Hubbard interactions. Recently the authors of Ref. [39] have also investigated the role of interactions in ribbons with finite lengths using a mean-field prescription. Other interesting phenomena occur when certain symmetries, such as the sublattice or *chiral* symmetry, is broken in these systems [40].

Though states in these hybrid systems demonstrate localization originating at junctions between different distinct AGNRs, the exact asymptotic behavior of these localized states has not been quantified. As a function of distance from a junction wavefunctions may fall off exponentially ('strong localization') or with some power law ('weak localization'). This distinction has ramifications for the engineering requirements for manufacturing ribbons that support localization. As we show in this paper, ribbon junctions that support wavefunctions with exponential decays on either side can be constructed such that they are nearly gapless under the tight-binding approximation. Further, localization in this case can occur for a hybrid system with a single junction.

On the other hand, weak localization on either side of the ribbon junction cannot support a zero mode. Using weak localization to concentrate a state along a ribbon segment requires ribbons with an even number of junctions.

These findings are easily understood through an effective theory (ET) of the hybrid ribbons in one dimension (1-D). We show how to construct such a theory, and demonstrate how the parameters of this ET can be tuned to reproduce the low-energy spectrum of hybrid ribbons, even in the presence

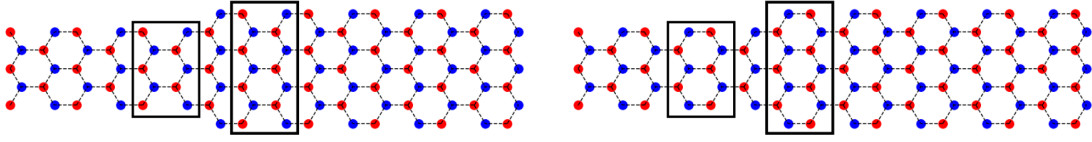


Figure 4.1: A symmetric  $5/7$  junction made from the intersection of a 5-AGNR and a 7-AGNR. The solid rectangles highlight the unit cells of the two individual AGNRs, with two different but equivalent choices shown in the left and right panels. The junction resides between the two unit cells shown, respectively. Note that the central junction has an additional lattice point residing on the blue sublattice compared to the red sublattice in both cases, as described in the text. The central junction and the junction on the edge of the compound unit cell can be thought of as a single unit cell divided in two.

of non-perturbative interaction. Once tuned, it is much simpler to use this theory to ascertain the behavior of the low-energy spectrum of these systems for different ribbon lengths. Indeed, we use this ET to make predictions on the specifications of hybrid ribbons that lead to a (nearly) gapless system. We verify the predictions of our ET by comparing directly with calculations on the original hybrid systems.

Our paper is organized as follows. In Sec. 4.1 we review ribbons of uniform width and their non-interacting dispersion relations; whether a given width is gapped or not controls how electronic states are localized around the junctions of hybrid ribbons, which we demonstrate in Sec. 4.2. If a uniform ribbon is gapped the wavefunction decays exponentially on a segment of that width near a junction, while if the uniform ribbon is not gapped the wavefunction decays only with an inverse power law. From this understanding we develop and test an effective one-dimensional tight-binding Hamiltonian with two hopping amplitudes in Sec. 4.3. We show how the effective hopping amplitudes depend on the specific geometries of the hybrid ribbons, identifying low-energy constants (LECs) that depend on the width of the ribbon segments but not on their lengths. After fitting these LECs we demonstrate how our ET predicts ribbon widths and lengths that have a nearly-gapless spectrum. We extend the validity of the ET to hybrid ribbons with Hubbard interaction by introducing an additional LEC and verify correctness using quantum Monte Carlo simulations. After commenting on hybrid ribbons not aligned along their centers, we recapitulate in Sect. 4.4.

Armchair graphene nanoribbons (AGNRs) are carbon nanostructures defined by their edge terminations and can be seen as a portion of an infinite honeycomb lattice with inter-ion spacing  $a$ . The ribbons enjoy a translational symmetry along their length which generates a lattice momentum  $k$ . The width  $N$  of an AGNR is the number of ions along a zigzag path across the ribbon, and a single unit cell consists of two neighboring transverse zigzags. A ribbon of  $m$  unit cells can be compactified with periodic boundary conditions at its ends. Fig. 4.1 shows two ribbon segments of widths 5 and 7 joined at a junction. Clearly both segments as well as the complete hybrid ribbon have a bipartite structure where ions of one triangular sublattice (colored blue) have neighbors only on the other sublattice (colored red) and vice-versa.

In order to understand how the geometry influences the strength of electronic state localisations, we have to investigate the energy spectra of the different armchair ribbons themselves. Of interest will be the state that is closest to zero energy, since this state will govern the long-range correlations. A gapped system has a finite correlation length while an ungapped system has infinite correlations, cut off in practice by the physical length of the ribbon.

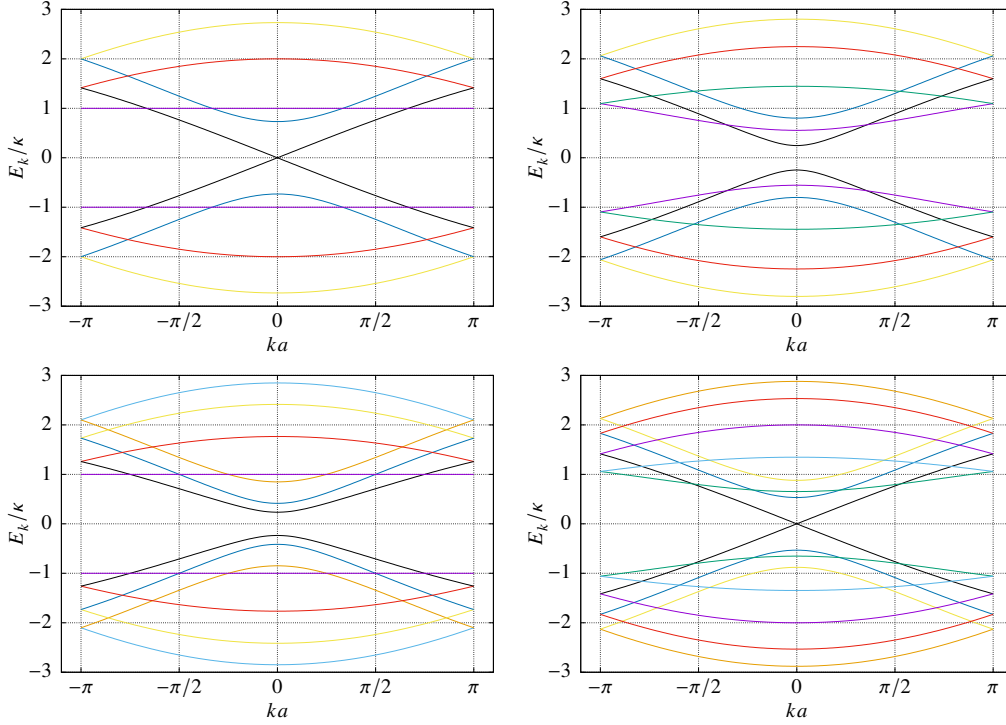


Figure 4.2: Dispersion relations of infinitely long (i.e.  $m_N = \infty$ ) armchair ribbons with widths  $N = 5, 6, 7, 8$  (top left to bottom right).

With nearest-neighbor hopping amplitude  $\kappa$  these systems are described by the Hamiltonian

$$H = -\kappa \sum_{\langle x,y \rangle} \left( \psi_x^\dagger \psi_y + \psi_y^\dagger \psi_x \right) + \text{interactions} \quad (4.2)$$

where  $\psi_x$  destroys an electron at site  $x$ , with  $x$  and  $y$  are on different sublattices, and we suppress spin labels here and henceforth. When the interactions are neglected,  $H$  is just the tight-binding Hamiltonian used to describe the band structure [25, 41] and we can find energy eigenstates by diagonalizing the adjacency matrix.

The dispersion relations of armchair ribbons of widths 5 to 8 described by this Hamiltonian are shown in Fig. 4.2. The armchair ribbons with widths  $N = 5$  and  $N = 8$  are gapless while the widths  $N = 6$  and  $N = 7$  have finite gaps. This reflects the well-known fact that armchair ribbons are gapless if and only if their width is

$$N \equiv 2 \pmod{3}. \quad (4.3)$$

A general analytic description of the spectrum of these ribbons in the tight-binding model can be found in Ref. [14]. The noninteracting many-body state has all the negative energy states filled.

The authors of [15] enumerated four distinct types of AGNR edge terminations based on ribbon width and inversion and mirror symmetries. They showed that the nanoribbons have an associated

binary conserved quantity, the so-called  $Z_2$  topological invariant.

## 4.2 Hybrids Ribbons and Junctions

Finite ribbon segments of different width can be joined together to form a *hybrid ribbon*. The interface of two materials can support surface modes [24], in this case modes localized along the hybrid ribbon's length. We mention two out of the multitude of possible shapes that hybrid ribbons can have: two semi-infinite segments with only a single junction and repeated segments of alternating widths, with a junction at every width change. If the alternation is regular the two alternating segments form one compound unit cell which may be repeated  $L$  times along the hybrid ribbon's length; we reuse  $m$  to count the number of unit cells in a segment. The compound unit cell will later be represented by two sites in our effective theory, one site for each junction.

In Ref. [15] it was argued that the topology of these systems preserved the localization of states even under the presence of interactions. Their perturbative calculations corroborated this claim. Consequently in Ref. [2] it was shown numerically that this localization persisted in the non-perturbative regime. In particular, [2] investigated the 7/9-hybrid (and the 13/15-hybrid) nanoribbon with non-perturbative stochastic methods and found that localization indeed persisted in the presence of a Hubbard interaction. One goal of this present work is to better quantify the nature of these localized states for not only the 7/9 geometry, but for other hybrid nanoribbon geometries. As we show in later sections, the dynamics of these low-energy states can be captured in a simple effective 1-D model, which in turn allows us to make predictions for a broader range of hybrid nanoribbons.

For simplicity we only consider ribbons segments consisting of a width- $N$  armchair of length  $m_N$  and a width- $N + 2$  armchair of length  $m_{N+2}$  with odd  $N$ . When ribbon segments of different widths are aligned along their centers, as in Fig. 4.1, so that the ribbon has a reflection symmetry, the junction has a surplus of a single lattice site, belonging to one of the sublattices (blue in the center of Fig. 4.1, red at the edge). In this picture it is crucial to tile the hybrid ribbon with unit cells of similar shape in both lattice segments. The two left-over zigzags on the junctions can be understood as a single unit cell divided. While in the left panel of Fig. 4.1 we choose unit cells that are open at top and bottom, we can equivalently choose all unit cells to be closed as in the right panel. In the former case the surplus lattice site comes from the junction zigzag of the broad segment while in the latter case the surplus resides within the narrow segment, but it always belongs to the same sublattice. This sublattice surplus locally breaks chiral symmetry. We will find later that hybrid ribbons aligned at an edge do not break chiral symmetry.

Fig. 4.3 shows two compound unit cells of an example 7/9-hybrid nanoribbon, where we see the honeycomb lattice which forms the basis for extended carbon nanostructures. A ribbon of width  $N = 7$  has topological invariant  $Z_2 = 0$ , while a ribbon of width  $N + 2 = 9$  has invariant  $Z_2 = 1$  (more details in Tab. 4.1); localization is conjectured to occur at the junctions [15]. This system has been experimentally fabricated [16, 17].

Because the geometry controls the gap, a localized state will decay differently on the two sides of the junction. A localized electron's wavefunction  $\phi$  should decay with the dimensionless distance from the junction  $\Delta x$ . With large enough length segment length  $m$ , we expect the asymptotic decay to be governed by the gap or gaplessness of the infinite ribbon of the same width.<sup>1</sup> In a gapped segment

<sup>1</sup> Exactly how long each segment needs to be to exhibit such a simple decay is not clear a priori. While we only intend to describe asymptotic behaviour, in practice  $m \gtrsim 3$  appears to suffice.

we expect strong localization and exponential decay

$$\phi \sim e^{-\beta \Delta x}, \quad (4.4)$$

and in a gapless segment we expect monomial decay

$$\phi \sim \Delta x^{-\beta}, \quad (4.5)$$

and only weak localization. In both cases  $\beta$  is some positive width-dependent parameter independent of segment length  $m$  and the number of compound unit cells  $L$ . This dependence on width  $N$  has to be determined from fits to solutions of the full problem.

In the bottom panel Fig. 4.3 we show the lowest positive-energy single-electron tight-binding eigenfunction on a 7/9 hybrid ribbon where the width-7 segments have 5 unit cells and the width-9 segments have 8 unit cells each. We take the eigenfunction  $\phi$  and compute the density normalized per unit cell

$$\rho(x) = |\phi(x)|^2 \quad \frac{1}{L} \sum_x \rho(x) = 1. \quad (4.6)$$

The radii of the circles are proportional to  $\rho$  and colored according to their sublattice. In the top panel we show the marginal densities  $\rho(x)$  summed over the width of the ribbon, again coloring according to sublattice. The green line is obtained by adding both the red and blue marginal densities along a transverse zigzag and represents the total occupancy probability along the ribbon's length. Both 7- and 9-armchair ribbons are gapped since neither satisfy the gaplessness condition (4.3), so correlations decay exponentially on both sides of each junction in Fig. 4.3.

That the  $N = 7$  gap is larger than the  $N = 9$  gap is apparent by the faster decay on the width-7 segments. We observe that on neighboring junctions the states are not only localized in space but are also concentrated on one sublattice or the other. The strong exponential localization allows these states to be clearly delineated.

We remark that this junction also has changing topology according to Ref. [15] (see Tab. 4.1) and their prediction of localisation therefore coincides with ours. The same occurs for the 13/15 hybrid system, which we show in Fig. 4.4. However, we will see that there are counterexamples to the otherwise well-motivated conjecture put forth in Ref. [15] that the localizations are driven purely by the topological  $Z_2$  boundary. The model we will develop in Sec. 4.3 is generally applicable and reliably quantifies localizations even in the cases that evade the topological argument.

Fig. 4.5 shows the low-energy states from 3/5, 5/7, and 9/11 hybrid ribbons. Each of these examples has a gapless segment, since  $5 \equiv 11 \equiv 2 \pmod{3}$  satisfying the gaplessness condition (4.3), and on the gapless segment no sharp localization on the junction occurs. Instead, on the scale shown the eigenstate looks essentially constant on the gapless segments.

We distinguish these ‘Kilimanjaro-localized’ states with a large plateau from the sharply-peaked ‘Fuji-localized’ states that have exponential decay on both sides of a junction.<sup>2</sup> We remark that the cumulated occupancy density shown in green is not exactly constant in the plateau region. Instead, the density increases towards the center. In fact, if the gapless segment is very short, the localization can be very sharp, not unlike Fuji localization. But, the state can also be meaningfully spread over vast

<sup>2</sup> Mount Kilimanjaro in Tanzania has an extended high plateau, while the Japanese mount Fuji features a sharp peak. The resemblances to the respective localisations inspired the naming scheme.

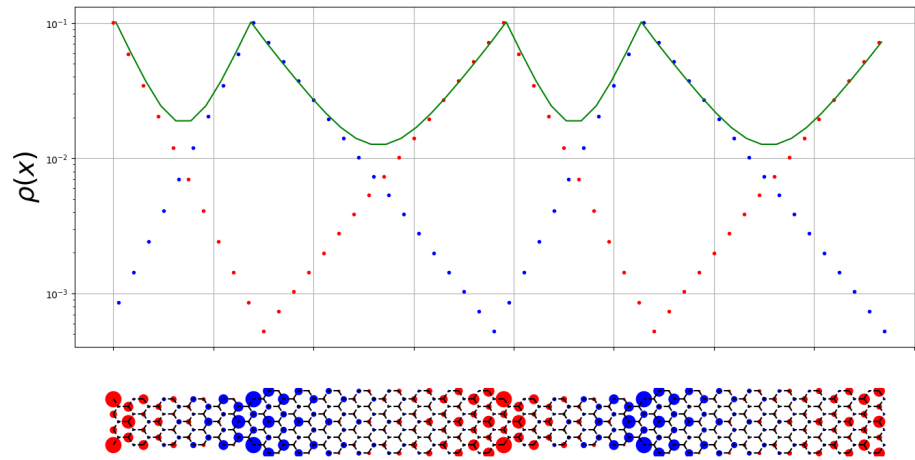


Figure 4.3: Bottom: the Fuji-localised state of a 7/9 hybrid ribbon with  $(m_7, m_9) = (5, 8)$ , shown with  $L = 2$  two unit cells. The circles' radii are proportional to the densities  $\rho$  (4.6) and their color indicates the sublattice. Top: We sum  $\rho$  along the width of the ribbon and color each point colored according to sublattice. The green line is the sum of both red and blue points along one zigzag cross-section and represents the total occupancy probability (integrated across the ribbon's width) along the ribbon's length.

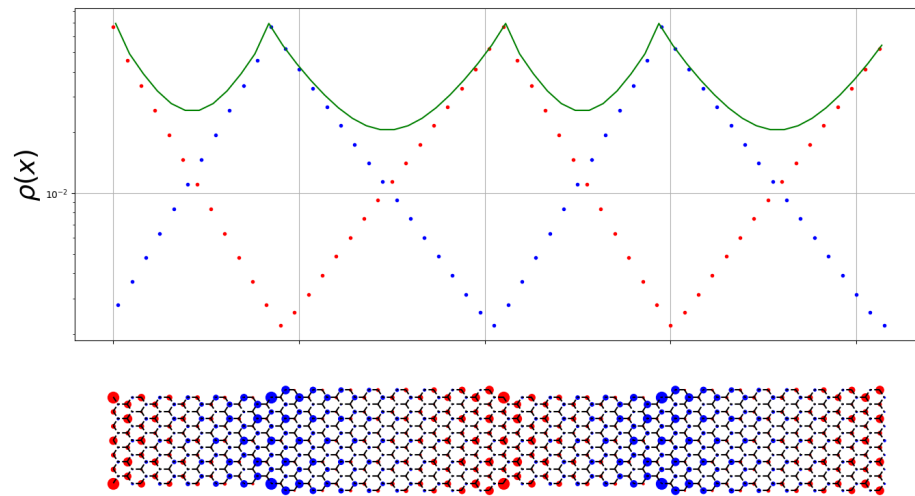


Figure 4.4: Similar to fig. 4.3 but now the 13/15 hybrid with  $(m_{13}, m_{15}) = (6, 8)$ .

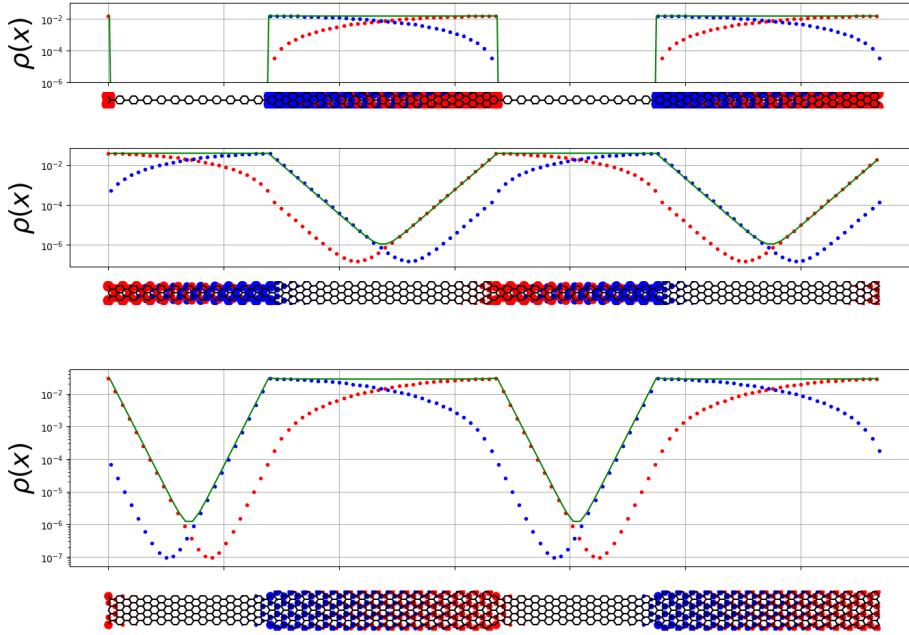


Figure 4.5: Lowest energy state densities of a 3/5 (top), a 5/7 (middle) and a 9/11 hybrid (bottom), all with segment lengths  $(m_N, m_{N+2}) = (12, 16)$ . These examples do not feature the two-sided exponential Fuji localisation on the junctions since width-5 and width-11 armchair ribbons have long range correlations. However, the states are trapped within those gapless segments, showing Kilimanjaro localisation.

regions if the gapless segment is long enough.

Focusing on the 5/7 hybrid, as we make  $m_7$  larger the low-energy state remains confined to the width-5 segments. If we take  $m_7 \gg m_5$ , we can effectively localize the density into an arbitrarily small space compared to the total length of the ribbon. Unlike the Fuji localization, in this limit there is no sharp splitting between the two sublattices. The localization in the gapless segment are only polynomial in nature and states localized to the two sublattices at either end of the gapless segment have a large overlap.

The 5/7 example, in particular, contradicts the claim in Ref. [15] that a change in topology implies a Fuji localization. However, we find that the reverse implication—localization requires a change in topology—is consistent with the examples we have examined and the effective theory we present in Sec. 4.3.

The findings of Ref. [15] are based on hybrid ribbons with a single junction connected by semi-infinite ends, whereas our investigations here involve hybrid ribbons with periodic boundary conditions, which essentially models an infinite number of junctions. A natural question is whether this difference accounts for the discrepancy between our findings. With our numerical techniques it is not possible to model infinite ribbons. However, instead of periodic boundary conditions at the ends, we can use open boundary conditions and investigate the nature of the localization as we extend the length of each semi-ribbon. We show the length-normalized densities for the lowest non-zero energy state<sup>3</sup> for

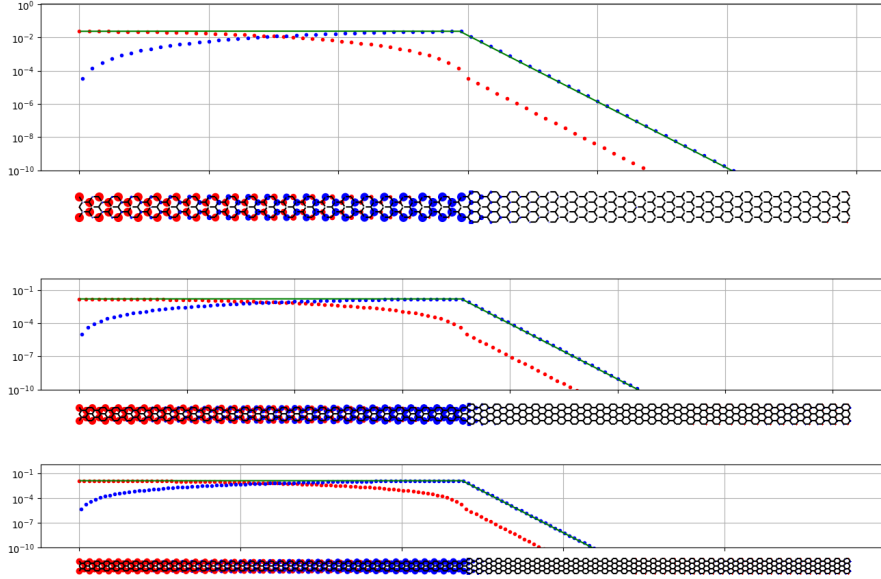


Figure 4.6: Lowest non-zero energy state densities of the 5/7 ribbon with open boundary conditions. The top panel has  $(m_N, m_{N+2}) = (20, 20)$ , middle  $(m_N, m_{N+2}) = (30, 30)$ , and bottom  $(m_N, m_{N+2}) = (40, 40)$ . The states are again trapped within those gapped segments and demonstrate Kilimanjaro localisation.

increasingly long 5/7 hybrid ribbons with open boundaries in Fig. 4.6. The Kilimanjaro localisation is prominent and remains so as the ribbons' respective lengths increase. We therefore surmise that this type of localisation persists in the limit of semi-infinite ends. This is perfectly in line with the expectations in our ET framework and cannot be reconciled with the predictions in Ref. [15].

Table 4.1: Topological invariant [15] (Tab. I therein) for the narrower and broader parts of different junctions respectively. In a hybrid ribbon with a symmetric junction (Figs. 4.1 and 4.3 to 4.5), the  $Z'_2$  invariant describes the topology in the narrow and  $Z_2$  the broader segment. In bottom aligned junctions (Fig. 4.12) both parts are described by the  $Z'_2$  invariant. Ref. [15] predicts localisations for junctions with changing topology.

$N$	3	5	7	9	11	13	15	17	19	21
$N + 2$	5	7	9	11	13	15	17	19	21	23
$Z'_2(N)$	1	0	0	0	1	1	1	0	0	0
$Z_2(N + 2)$	1	1	1	0	0	0	1	1	1	0

<sup>3</sup> With open boundary conditions we always find two degenerate zero-energy states that correspond to perfect localisations on the extreme ends of the system. These states play no role in the limit of semi-infinite ends, as their localisations are pushed to infinity. The relevant states are the lowest non-zero energy states, which we show in Fig. 4.6

### 4.3 Effective 1-D Tight-binding model

#### 4.3.1 Formulation

An electron localized on a junction is smeared out over many sites of one sublattice near by. We observe in Figs. 4.3, 4.4, and 4.5 that at a junction the wavefunction is concentrated on the sublattice with a surplus site. This sublattice symmetry breaking and wavefunction concentration allows us to treat the  $2L$  junctions from  $L$  compound unit cells as the sites of our model. Because the junctions alternate between having a surplus of one of the honeycomb sublattices (and the corresponding wavefunction concentration), we arrive at a length  $L$  bipartite lattice with a two-site basis. The two effective sites can be thought of as the local surplus of one or the other sublattice. Electrons hop between these effective sites via some hopping amplitude controlled by the width and length of the segment connecting them; a segment of width  $N$  and length  $m_N$  lets electrons tunnel with an amplitude controlled by the wavefunction overlap. If two junctions are separated by a strongly-localizing segment (4.4) of length  $m$  the wavefunction overlap and thus the tunnelling amplitude  $t$  will be exponentially small,

$$t \sim e^{-\beta m}, \quad (4.7)$$

while two junctions separated by a weakly-localizing segment (4.5) will have polynomial overlap and tunnelling amplitude

$$t \sim m^{-\beta}, \quad (4.8)$$

redefining the dimensionless  $\beta$ .

An effective 1-D tight binding Hamiltonian that describes a hybrid ribbon of alternating widths  $N$  and  $N + 2$  is

$$H_{1D} = - \sum_{x=0}^{L-1} \left( t_N c_{2x}^\dagger c_{2x+1} + t_{N+2} c_{2x+1}^\dagger c_{2x+2} + \text{h.c.} \right), \quad (4.9)$$

where  $c_x$  destroys a fermion at effective site  $x$ , and  $t_N$  is the tunnelling (or hopping) amplitude across a ribbon segment of width  $N$ . It can be block-diagonalised by a Fourier transformation yielding

$$H_{1D} = - \sum_k c_k^\dagger \begin{pmatrix} 0 & t_N e^{ik} + t_{N+2} e^{-ik} \\ t_N e^{-ik} + t_{N+2} e^{ik} & 0 \end{pmatrix} c_k, \quad (4.10)$$

where the dimensionless momentum  $k$  is in terms of the inverse lattice spacing and the creation and annihilation operators in momentum space are two-dimensional vectors,

$$c_k = \begin{pmatrix} c_{k,A} \\ c_{k,B} \end{pmatrix} \quad (4.11)$$

and the  $A$  and  $B$  indices indicate the two sublattices or equivalently the two junctions.

After diagonalising the blocks we obtain the dispersion relation

$$E(k) = \pm \sqrt{t_N^2 + t_{N+2}^2 + 2t_N t_{N+2} \cos 2k} \quad (4.12)$$

for momenta in the reduced first Brillouin zone  $k \in [0, \pi)$  and the energy gap

$$\Delta \equiv 2|E(\pi/2)| = 2\sqrt{t_N^2 + t_{N+2}^2 - 2t_N t_{N+2}} = 2|t_N - t_{N+2}| \quad (4.13)$$

between lowest positive and highest negative energies which will become very important in the following considerations. Note that a hybrid ribbon with small  $t_N$  and  $t_{N+2}$  necessarily has a small gap. However, a small  $t_N$  is a consequence of a large pure-armchair gap since in this case it is less likely to hop between junctions. This effective theory predicts that joining two strongly gapped ribbons leads to a very small overall gap.

Sharpening the scaling of the overlaps (4.7) and (4.8) into quantitative predictions, the effective hopping amplitudes are

$$t_N(m) = \begin{cases} \kappa \alpha m^{-\beta} & \text{with } \beta \sim 1, \quad \text{if } N = 2 \pmod{3}, \\ \kappa \alpha e^{-\beta m} & \text{with } \beta \sim \Delta_N, \quad \text{otherwise,} \end{cases} \quad (4.14)$$

with  $\alpha$  another (a priori unknown) positive dimensionless parameter that can only depend on  $N$ , not on  $m$  and  $L$  and the honeycomb  $\kappa$  (4.2) appears for dimensional reasons. In the first case  $\beta$  is expected to be related to critical behaviour and cannot be predicted from first principles. In contrast, the exponential decay is governed by the magnitude of the pure  $N$ -armchair ribbon gap  $\Delta_N$  up to small corrections. We will use this ansatz to fit the low-energy constants (LECs)  $\alpha$  and  $\beta$  for different values of  $N$ .

Concisely, the effective treatment predicts that an  $N/N+2$  hybrid ribbon of two armchair nanoribbons has Fuji-localised states with close to zero energy if and only if the junction is center-aligned and  $N \pmod{3} = 1$  so that neither width fulfils the gaplessness condition (4.3).

### 4.3.2 Determination of the Low-Energy Constants

We now have all ingredients to fix the low-energy constants (4.14) of our 1-D effective theory (4.9). By considering a particular  $N/N+2$  hybrid ribbon, we calculate the gap  $\Delta$  (defined as twice the lowest positive single-particle energy) of the hybrid system for different ribbon lengths  $m_N$  and  $m_{N+2}$ . For the sake of simplicity we choose one of the lengths very large, say  $m_{N+2} \gg m_N$ , so that the  $N+2$ -width ribbon segment is long enough to be compatible with the thermodynamic limit. Then the effects of this ribbon segment are negligible and the junction gap (4.13) reduces to  $\Delta = 2t_N$ . We fit our results for  $t_N(m_N)$  to the form of the effective hopping (4.14), fixing the parameters  $\alpha_N$  and  $\beta_N$ . Two representative fits are shown in Fig. 4.7, with a power law fit in the left panel and an exponential fit on the right.

We summarise the results of the fitted low-energy constants in table 4.2 for select values of  $N$ . Within either class, power law or exponential, we observe the trend that both LECs  $\alpha$  and  $\beta$  decrease with growing  $N$ . While we do not have a direct physical interpretation for the proportionality constant  $\alpha$ , it is clear that  $\beta$  has to follow this trend because the asymptotic  $N \rightarrow \infty$  case of graphene is gapless. In particular, the exponential case features decay coefficients  $\beta$  similar to the pure armchair ribbon

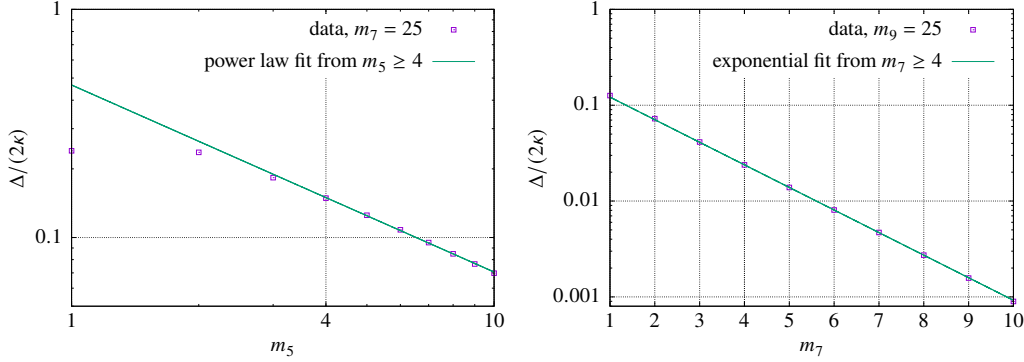


Figure 4.7: Gaps of a 5/7-hybrid (left) and a 7/9-hybrid (right) used to fit the LECs (4.14) for  $N = 5$  and  $N = 7$ , respectively. When fitting a power law as a function of the length  $m_5$ , the length  $m_7 = 25$  has been kept fixed and similarly for the exponential fit to  $m_7$  we fixed  $m_9 = 25$ .

gap  $\Delta_N$  as expected.

Note how the 7/9-junction is special in the sense that it is the smallest ribbon size with strong localisation for both widths. No Fuji localisation is possible in narrower center-aligned ribbons. We also remark that the 3-armchair ribbon features such a strong exponential decay that it is virtually instant and (at least within double floating precision)  $t_3(m) = 0$  for  $m > 0$ . Localised states do not penetrate into the 3-armchair at all.

Table 4.2: Fitted low-energy constants (LECs)  $\alpha, \beta$  from eq. (4.14) following the exponential (exp) or power (pow) laws depending on the width  $N$  of the armchair ribbon.  $\Delta_N$  is the corresponding energy gap of the ribbon without junction. For  $N = 3$  we have  $\beta = \infty$  and there is no value for  $\alpha$  since the wavefunction is exactly confined to the junction (see Fig. 4.5).

$N$	3	5	7	9	11	13	15	17	19	21
Decay	exp	pow	exp	exp	pow	exp	exp	pow	exp	exp
$\alpha$	-	0.57	0.21	0.22	0.43	0.13	0.15	0.32	0.09	0.11
$\beta$	$\infty$	0.89	0.54	0.34	0.79	0.30	0.23	0.69	0.22	0.18
$\Delta_N$	0.83	0	0.47	0.35	0	0.26	0.22	0	0.18	0.16

### 4.3.3 Application of our effective theory

Despite the simplicity of our effective theory, we can already use it to make predictions in cases where the original system is more difficult to simulate. We can apply our ET, for example, to predict the respective lengths at which the gap of a hybrid nanoribbon (almost) vanishes. As an example we return to our prototypical 7/9 hybrid system, but with the desire to pick segment lengths so that the system is as close as possible to gapless.

To minimize the gap (4.13) our ET provides the condition

$$t_7 \stackrel{!}{=} t_9 \quad \Rightarrow \quad \alpha_7 e^{-\beta_7 m_7} \stackrel{!}{=} \alpha_9 e^{-\beta_9 m_9} \quad \Rightarrow \quad m_7 = \frac{\beta_9}{\beta_7} m_9 + \ln \frac{\alpha_7}{\alpha_9} \quad (4.15)$$

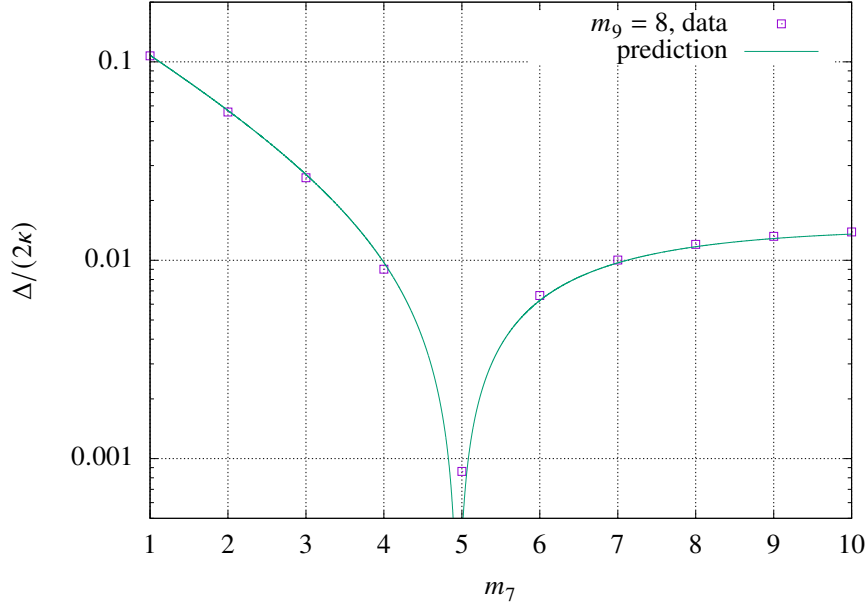


Figure 4.8: Gap of a 7/9-hybrid ribbon given by the prediction (4.15) and direct diagonalization of the underlying tight-binding Hamiltonian shown in (4.2) (without interactions).

has to hold as best possible for integers  $m_7$  and  $m_9$ . Using the parameters given in Table 4.2 we find that  $(m_7, m_9) = (5, 8)$  is a good tuple that nearly satisfies this constraint. This prediction is confirmed in Fig. 4.8, which shows the hybrid ribbon's gap as a function of the width-7 segments' length, holding the width-9 segments at  $m_9 = 8$ . The next three smallest tuples that our theory predicts for this system are  $(22, 35)$ ,  $(39, 62)$ , and  $(56, 89)$ . For the 13/15 hybrid system our effective theory predicts the following four smallest tuples giving a near zero gap:  $(m_{13}, m_{15}) = (6, 8)$ ,  $(29, 38)$ ,  $(52, 68)$ , and  $(75, 98)$ .

Note that in both these systems, both ribbon widths are gapped and the localization is Fuji. For systems where one width is gapped and the other is not, our theory predicts that such systems cannot support a (near) zero gap without weakly-localising segments many orders of magnitude longer than the strongly-localising segments. This is consistent with all our simulations to date.

### 4.3.4 Incorporating Interactions

So far we have focused on noninteracting tight-binding dynamics, both within the hybrid nanoribbon and its effective 1-D description. Including interactions, for example by adding an onsite Hubbard interaction  $U$  that couples the spin-up  $\uparrow$  and spin-down  $\downarrow$  electrons

$$H_{\text{Hubbard}} = U \sum_x \left( \psi_{x,\uparrow}^\dagger \psi_{x,\uparrow} - \frac{1}{2} \right) \left( \psi_{x,\downarrow}^\dagger \psi_{x,\downarrow} - \frac{1}{2} \right) \quad (4.16)$$

to the underlying tight-binding Hamiltonian (4.2), precludes simple diagonalization.

Ref. [2] showed that the localization was robust against the influence of the Hubbard interaction

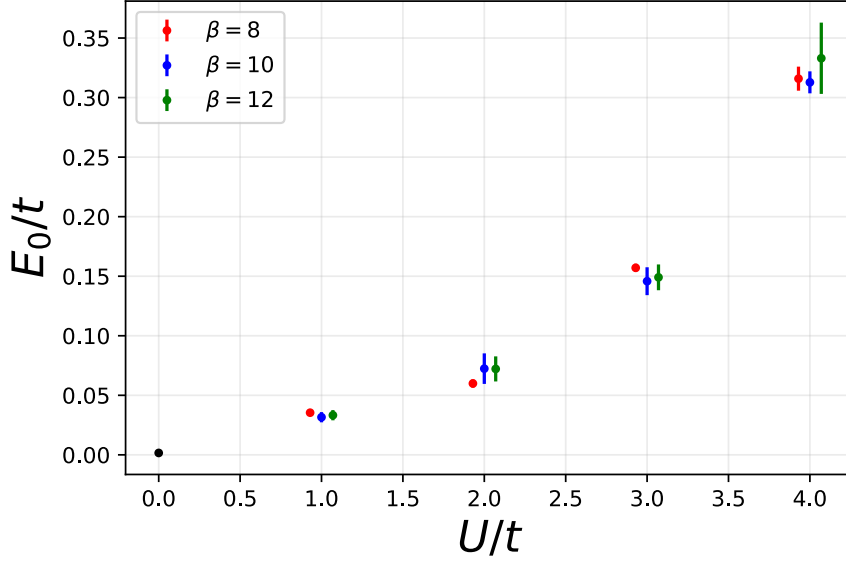


Figure 4.9: Interacting energy  $E_0$ , depicted as points with error bars, of the lowest state as a function of onsite Hubbard interaction  $U$  obtained from QMC calculations in Ref. [2] for the 7/9 system with  $(m_7, m_9) = (3, 5)$ . The 7/9 simulations were performed with three different values of inverse temperature  $\beta$ , where  $\beta = 8$  (12) results are slightly shifted to the left (right) to help visually differentiate the points. The black point corresponds to the non-interacting result.

(4.16) via stochastic Monte Carlo methods and that there is a nearly quadratic dependence of the gap on  $U$ . Fig. 4.9 shows this dependence for the example of the 7/9 system.

Our 1-D effective model (4.9) can easily incorporate these results by including

$$m_s \left( c_{2x}^\dagger c_{2x} - c_{2x+1}^\dagger c_{2x+1} \right), \quad (4.17)$$

where the effective staggered mass  $m_s$  is a LEC and fit to reproduce the quadratic dependence. The momentum-space formulation (4.10) becomes

$$H_{1D} = - \sum_k c_k^\dagger \begin{pmatrix} m_s & t_N e^{ik} + t_{N+2} e^{-ik} \\ t_N e^{-ik} + t_{N+2} e^{ik} & -m_s \end{pmatrix} c_k, \quad (4.18)$$

which can be easily diagonalized, giving

$$E(k) = \pm \sqrt{t_N^2 + t_{N+2}^2 + 2t_N t_{N+2} \cos 2k + m_s^2}. \quad (4.19)$$

and a gap

$$\Delta = 2|E(\pi/2)| = 2\sqrt{(t_N - t_{N+2})^2 + m_s^2}. \quad (4.20)$$

The presence of this staggered mass does not change the scaling behavior of the hopping terms (4.14) and therefore does not affect the nature of the localization. For a given  $U$  simulated with a particular

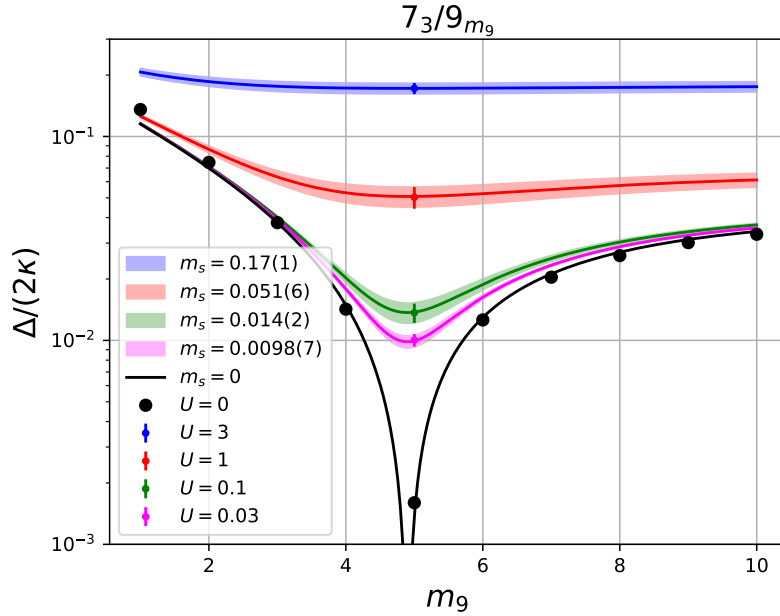


Figure 4.10: Extracting  $m_s$  from the underlying theory. Here stochastic simulations of the full 7/9 hybrid system with tuple  $(m_7, m_9) = (3, 5)$ ,  $L = 1$  and inverse temperature  $\beta = 8$  were performed at different values of  $U$  as labelled in the figure and shown as points with error bars. The value of  $m_s$  was fitted to each of these points, and the resulting prediction of the gap provided by our ET (eq. 4.20) for other tuples where  $m_7 = 3$  and  $m_9 \in [1, 10]$  is plotted. The black points are the non-interacting results.

tuple  $(m_N, m_{N+2})$ , the parameter  $m_s$  can be tuned so that our ET matches the energy of the underlying theory, like that shown in Fig. 4.9. Once tuned, we can then make predictions for the size of the gap for hybrid ribbons with segments of the same widths but with different lengths.

The tuple that minimizes the gap will be the one that corresponds to  $|t_N - t_{N+2}| \sim 0$ . Since the staggered mass preserves the scaling behavior of the hopping terms, the predicted tuples that minimize the gap in the previous section when  $m_s = 0$  will also minimize the gap for  $m_s \neq 0$ . However, in this case the minimum gap becomes  $\Delta \sim 2m_s$ .

As an example of how we can extract  $m_s$ , we perform stochastic simulations of the underlying Hubbard theory on the full 7/9 hybrid ribbon with tuple  $(m_7, m_9) = (3, 5)$ . The details of our Quantum Monte Carlo (QMC) simulations are described in [2]. In short, we sample the electron configurations from their quantum mechanical probability distribution using a Markov chain with global updates. In the limit of high statistics these simulations become exact. Given limited computational resources, we arrive at a distribution of values around the true result and we depict the standard error of this distribution as error bars in Figures 4.9 to 4.11.

The results of the gap for different values of Hubbard coupling  $U$  are shown as points with errorbars in Fig. 4.10. We then fit our ET to these results, thereby extracting  $m_s$  with the values shown in Fig. 4.10. With  $m_s$  in hand, we can predict the value of the gap for other combinations of segment lengths, shown by bands in the same figure.

To demonstrate the efficacy of our ET, we use these same values of  $m_s$  to plot our predicted gaps for

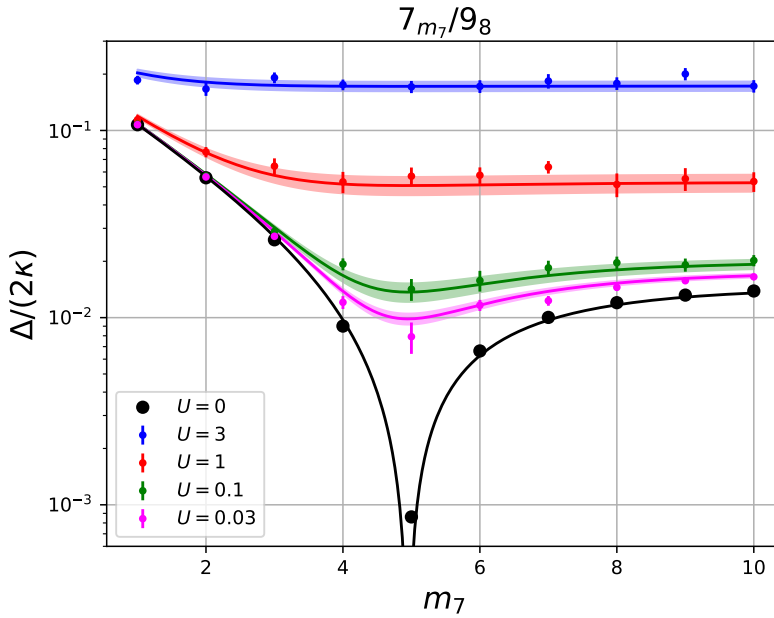


Figure 4.11: Comparing our ET prediction with the underlying theory. Using the values of  $m_s$  extracted in Fig. 4.10, we plot our ET prediction of the gap, shown as bands, for  $7/9$  geometries where  $m_9 = 8$  and  $m_7 \in [1, 10]$ . Superimposed on these bands are the gaps obtained from stochastic simulations of the underlying theory of these systems.

completely different  $7/9$  geometries, with  $m_9 = 8$ , in Fig. 4.11. Every band in Fig. 4.11 is a prediction given the low energy constants  $\alpha$  and  $\beta$  from the noninteracting case and the effective staggered mass  $m_s$  for that Hubbard coupling. In particular, the  $(m_7, m_9) = (3, 5)$  hybrid geometry used to extract  $m_s$  does not appear in Fig. 4.11 at all. We then perform stochastic simulations of the underlying theory of these systems and plot their resulting gaps, shown as data points with errorbars. We find good agreement between our simulations and ET. We thus surmise that our ET with a staggered mass captures both the dynamics and interactions of the lowest energy spectrum of the hybrid nanoribbons.

More quantitative descriptions of interacting hybrid nanoribbons, potentially going beyond Hubbard interactions, are possible within our formalism. For example, the inclusion of off-diagonal superconducting pairing terms, i.e.  $c_k c_k$  and  $c_k^\dagger c_k^\dagger$ , may be done with the aid of a Bogoliubov transformation [29]. One could alter the dynamics of the system by including next-to-nearest neighbor hoppings, or extend the interaction by considering onsite plus nearest neighbor couplings (i.e. extended Hubbard). Such possibilities are the subject of future investigations.

### 4.3.5 Misaligned Hybrid Ribbons

In the hybrid ribbons discussed so far the segments are aligned along their center. In Fig. 4.12 we show junctions aligned along the bottom edge. Unlike the center-aligned hybrids, the junctions of these edge-aligned hybrids do not have surplus of one sublattice or the other and do not break the local sublattice symmetry. This can be seen by tiling the entire hybrid ribbon with similar unit cells

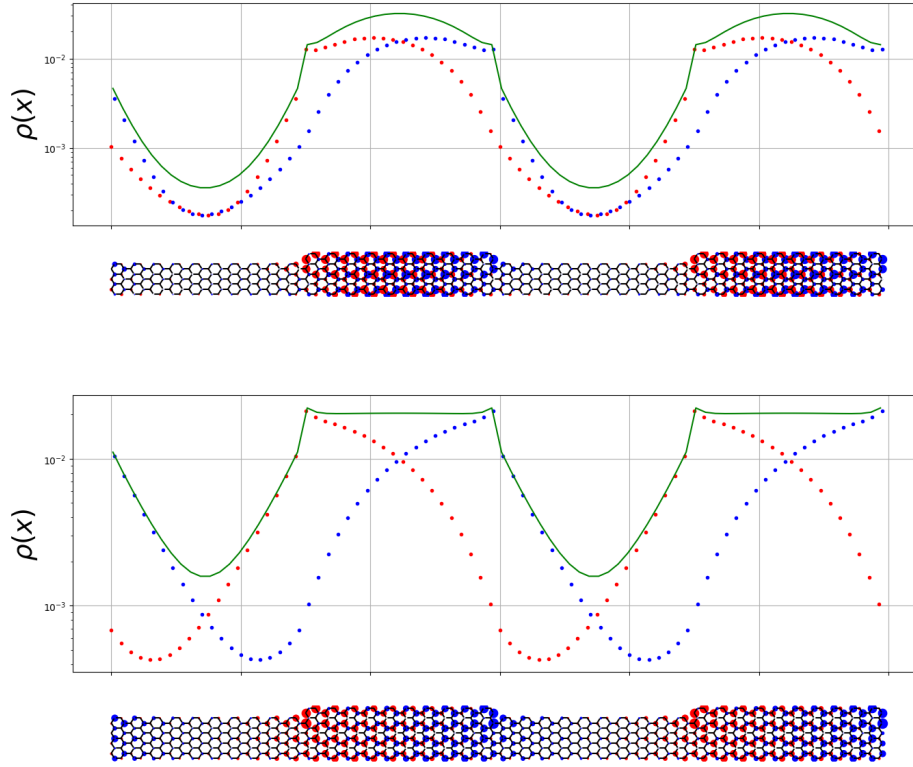


Figure 4.12: Lowest energy state densities of a 7/9-junction (top) and a 9/11-junction (bottom) with  $(m_N, m_{N+2}) = (10, 10)$  and aligned at the bottom rather than the center. According to Ref. [15] the 9/11-junction features a change in the topology of the respective armchairs (see Table 4.1). Both cases are Kilimanjaro-localised since the 9- and 11-armchair sides, respectively, exhibit long range correlations.

(closed at top and bottom as in the right panel of Fig. 4.1) so that no junction zigzag remains. Strictly speaking, our ET breaks down in this case because no effective lattice site is generated.

Because the sublattice symmetry is locally maintained, there is no local surplus of either sublattice and we predict that no Fuji localisation is possible. This is indeed what we observe in both cases of 7/9 and 9/11 edge-aligned junctions. The latter has a change in topology as can be seen in Table 4.1 and thus poses another counterexample to the conjecture in Ref. [15]. We identify these states as another realisation of Kilimanjaro-localisation; the state concentrates into the segment with the smaller gap.

For hybrids whose segments' widths differ by more than 2 some offsets will maintain the sublattice symmetry and some will not. We leave a detailed study of these scenarios to future work.

## 4.4 Conclusions

When two armchair graphene nanoribbons (AGNRs) of different widths are joined symmetrically (see e.g. Fig. 4.3), the combined system can feature a smaller band gap than either of the AGNRs and the state with energy closest to zero is localised at the junction. Such a localisation can either be strong with correlations decaying exponentially, or weak with a mere power law decay of correlations (typically not considered localised). We showed that the nature of this localisation depends solely on the band gaps of the AGNRs at either side of the junction. More specifically, the localisation is strong on one side of the junction if and only if the AGNR on this side has a non-zero gap. This in turn is the case if and only if the ribbon is of width  $N \neq 2 \pmod{3}$ .

We discovered that, in addition to localisations on junctions, a different type of localisation is also possible, namely a state localised within a hybrid ribbon segment as shown in Fig. 4.5. We dub the former type of localisations ‘Fuji’ and the latter ‘Kilimanjaro’. Fuji localisations require exponential correlation decay on both sides of the junction, therefore they are only realised by symmetric  $N/N + 2$  junctions with  $N \pmod{3} = 1$ . Kilimanjaro localisations are much more common in that they appear in all  $N/N + 2$  hybrid AGNRs (symmetric and non-symmetric, see Fig. 4.12) without Fuji localisation. We observed that these results often coincide with the topology based conjecture for Fuji localisations put forward in Ref. [15], however, we have also identified counterexamples to the predictions from topology arguments while our description is more fundamental and rigorous for all  $N/N + 2$  hybrid AGNRs with odd  $N$ .

We have derived a very simple way to predict and accurately quantify the different types of localised bound states appearing in hybrid AGNRs. For this we reduce the initial two-dimensional tight binding problem to a one-dimensional effective theory (ET) where the junctions of the hybrid AGNR form the sites of the 1-D lattice. The ET also relies on a tight binding Hamiltonian (4.9) which is diagonalised analytically and the hopping amplitude between two junctions is defined solely by the ribbon connecting these junctions. Eq. (4.14) summarises this dependence. The hopping decays exponentially with ribbon length for gapped ribbons, signifying strong localisation, and it decays as a power law for gapless ribbons resulting in weak localisation. We have identified two parameters  $\alpha, \beta$ , so-called low-energy constants (LECs), in this description that depend only on the width of the AGNR and cannot be determined other than through fitting. We have performed these fits for odd ribbon widths up to  $N \leq 21$  and summarised the results in table 4.2. The same fitting procedure can easily be extended to arbitrarily broad ribbons, limited only by computing resources. Once the LECs are determined, they can be used to predict the band gap in hybrid AGNRs, for instance yielding tuples of respective ribbon segment lengths with the smallest gap.

Finally, we put forth an extension of our ET in the presence of Hubbard type interactions (4.16). Consistent with previous findings [2], we predict the localisations to persist in the presence of interaction and we furthermore describe the quadratic dependence of the gap on the Hubbard interaction using an effective staggered mass term as a third LEC.

Localised Fuji-type states in armchair nanoribbons have been proposed as qubit candidates for fault-tolerant quantum computing before [2, 15, 16, 18] (nicely explained and visualised in Ref. [42]). Their stability against perturbations make them very promising for this application. We now add that Kilimanjaro-localised states are also well suited for the same task and they even might have some advantages, for instance that Fuji localisations come in alternating shapes while all Kilimanjaro localisations are symmetric and thus equivalent. Moreover, while localised Fuji states for a particular junction type always have the same extent, Kilimanjaro states can be smeared out over virtually

arbitrary lengths, purely governed by the length of the confining ribbon segment.

---

## Hubbard interaction at finite $T$ on a hexagonal lattice

---

This chapter is based on [4]

**Hubbard interaction at finite  $T$  on a hexagonal lattice**, L. Razmadze and T. Luu, PoS LATTICE2024 071 (2024) [[arXiv:cond-mat/2411.03196](https://arxiv.org/abs/cond-mat/2411.03196)]

Understanding how interactions and external perturbations modify the behavior of quantum systems is a central problem in condensed matter physics. Among the many models studied, the Hubbard interaction, characterized by an interaction strength  $U$ , serves as a prototypical framework for examining these effects. The Hubbard model captures the essential physics of electron-electron interactions in lattice systems and has been used in our prior research as a perturbing force to study stability of the localized states. In this paper, we focus on the effects of the Hubbard interaction on the electronic properties of graphene. However, the analysis can easily be extended to the graphene nanoribbons.

The approach builds upon the tight-binding model of graphene, which accurately describes its low-energy electronic states. By introducing the Hubbard interaction, we systematically explore how the energy spectrum and state properties are modified. At half-filling, our findings reveal that linear corrections in  $U$  vanish due to symmetry constraints, and the leading-order contributions scale as  $O(U^2)$ . This is also what we observed in the previous works. This result suggests that the absence of linear corrections is not merely a coincidence but is rooted in the chiral or sublattice symmetry of the system. This hypothesis is further supported by the observation that introducing a staggered mass, which breaks sublattice symmetry, reinstates linear terms in  $U$ . Moreover, even when deviating from half-filling by adding a chemical potential, the linear corrections remain absent, underscoring the robustness of this symmetry-driven behavior.

The combined effects of interactions and thermal fluctuations on localized states remain an open question. To investigate this, we introduce thermal perturbations and analyze their influence on energy states and temporal correlations. Specifically, we derive time-dependent correlation functions analytically and compare them against numerical results obtained via Monte Carlo simulations. This comparison reveals that our perturbative treatment remains accurate even for relatively large values of  $U$ , particularly in systems with small lattice sizes where finite-size effects are prominent. In [D](#)  $3 \times 3$  graphene is examined. Due to existence of Dirac  $K$  points correlator at  $\Gamma$  point exhibits a plateau, which was suspected from HMC simulations, but was written of as an artifact due to insufficient precision.

To validate our findings, we further analyze smaller lattice systems using exact solutions. These exact results exhibit remarkable agreement with the perturbative calculations, even for non-perturbative values of  $U$ . This agreement highlights the robustness of our approach and provides strong evidence for the reliability of the perturbative framework across a broad range of interaction strengths. The interplay between exact and perturbative results offers valuable insights into the behavior of strongly interacting systems and the limits of analytical approximations.

Our investigation extends naturally to graphene nanoribbons, where the interplay of geometry, symmetry, and interactions creates a rich landscape of physical phenomena. Nanoribbons exhibit unique electronic properties, such as width-dependent bandgaps and edge states, making them ideal systems for exploring the effects of interactions and perturbations. By analyzing nanoribbon systems, we demonstrate how structural effects, such as ribbon width and edge symmetry, influence the behavior of low-energy states. For example, at specific ribbon widths, chiral symmetry ensures the emergence of zero-mass excitations, which dominate the electronic response. These properties make nanoribbons an excellent platform for studying the combined effects of Hubbard interactions and thermal perturbations.

In the context of thermal perturbations, we explore the dependence of energy states and correlation functions on temperature. Finite temporal volume effects are explicitly analyzed, revealing that thermal fluctuations influence the stability of non-perturbed states. The resilience of quantum states under thermal perturbations is a key result of our study, providing further evidence for their robustness and potential applicability in real-world devices.

The broader implications of this work lie in its ability to bridge theoretical predictions and practical applications. By elucidating the role of Hubbard interactions and thermal effects in graphene-based systems, this study provides a framework for designing and optimizing nanoscale devices. Graphene nanoribbons, with their tunable electronic properties and rich interplay of topology and symmetry, emerge as promising candidates for applications in nanoelectronics and quantum information science. Furthermore, the insights gained from this study contribute to a deeper understanding of interaction-driven phenomena in strongly correlated systems, paving the way for future explorations of novel materials and quantum states of matter.

## 5.1 Introduction

In any quantum system, we can define a characteristic temperature  $T_C$ , representing a scale comparable to the energy of the system's lowest eigenmode. At temperatures  $T \ll T_C$ , the thermal energy is insufficient to excite even the lowest eigenstates, enabling an approximation  $T = 0$  since temporal finite-volume effects are negligible. However, when  $T \approx T_C$ , the application of thermal field theory becomes essential to accurately capture the system's behavior.

In the context of lattice QCD, this characteristic temperature corresponds to the pion mass  $T \approx m_\pi \approx 150\text{MeV}$ , a sufficiently high threshold where thermal effects significantly impact the study of nuclear matter and quark-gluon plasma [43, 44]. In “cold” lattice QCD calculations, where the temporal extent is  $\approx 30 - 40 \text{ MeV} \ll m_\pi$ , the finite temporal effects are justifiably ignored. Conversely, in physical low-dimensional lattice structures—such as graphene sheets, graphene nanoribbons, and topological insulators—the lowest energy eigenmodes are much lower than the temporal extent, often just a few eV or even zero [45], e.g. the momentum  $K$ -points in graphene. In these systems thermal effects must be included from the outset.

While temperature-dependent properties of small lattices can be investigated using computational approaches like Hamiltonian Monte Carlo (HMC), these methods remain computationally demanding even for modest lattice sizes. In this work, we approach the problem analytically, solving the self-energy  $\Sigma$  of the system perturbatively in the Hubbard coupling  $U$  to arrive at explicit temperature dependencies. For small lattices, exact solutions are also possible, enabling a direct comparison with perturbative results. Throughout this paper, we use the inverse temperature notation,  $\beta = 1/T$ , to express temperature-dependent quantities.

### 5.1.1 System

We investigate this system using a tight-binding Hamiltonian with an on-site Hubbard interaction term at half-filling [27], given by:

$$H = - \sum_{\langle x,y \rangle_s} (c_{xs}^\dagger c_{ys} + c_{ys}^\dagger c_{xs}) - \frac{U}{2} \sum_x (n_{x\uparrow} - n_{x\downarrow})^2 \quad (5.1)$$

where  $\langle x, y \rangle$  indicates a summation over nearest-neighbor sites,  $c^\dagger/c$  denotes the fermionic creation/annihilation operator, and  $n = c^\dagger c$  represents the corresponding number operator. This Hamiltonian is applied to a graphene sheet of size  $L_x \times L_y$  (see Fig. 5.1), where  $L_x$  and  $L_y$  refer to the width and length of the sheet in unit cells. We will refer to the  $1 \times 1$  sheet as the 2-site and the  $1 \times 2$  as

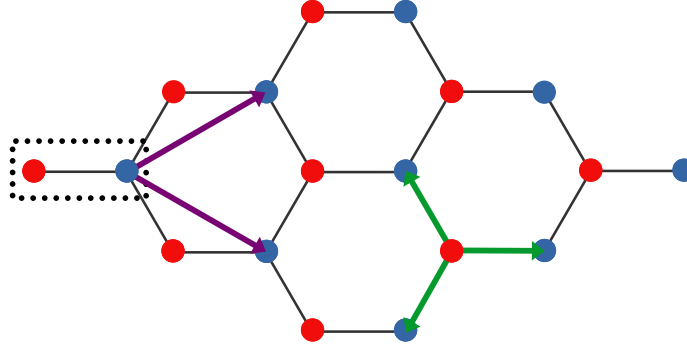


Figure 5.1:  $4 \times 4$  Graphene sheet. Graphene forms a hexagonal bipartite lattice with two sites **A** and **B** in each unit cell (dotted rectangle), located at  $\xi_A = (0, 0)$  and  $\xi_B = (1, 0)$  respectively. The lattice translation vectors, shown in purple, are  $a_{1,2} = (3/2, \pm\sqrt{3}/2)$ , and the nearest-neighbor vectors are marked by green arrows.

the 4-site lattice. The graphene structure also has a well-defined Brillouin zone (BZ) comprising of  $\Lambda = L_x L_y$  momentum points. Examples are given in Fig. 5.2.

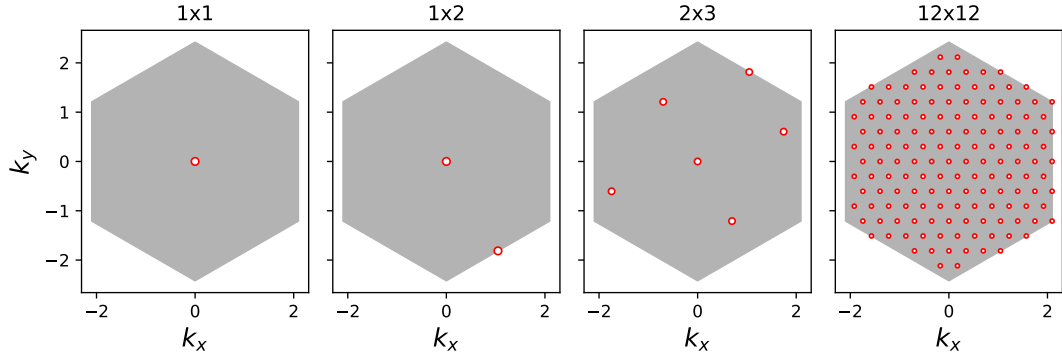


Figure 5.2: Brillouin zones for various lattice sizes in graphene. As lattice size increases, momentum points increasingly populate the hexagonal Brillouin zone. Of particular importance are the momentum points at the center ( $\Gamma$ -point), at the midpoint of the edges ( $M$ -point), and at the vertices ( $K$ -points). In the thermodynamic limit when  $L_x, L_y \rightarrow \infty$ , the BZ forms a hexagon.

To diagonalize the Hamiltonian, we apply a Fourier transform on each sublattice. Letting  $x$  enumerate unit cells and  $\lambda$  denote the sublattice, we define:

$$c_{x\lambda s} = \frac{1}{\sqrt{\Lambda}} \sum_k e^{ik(x+\xi_\lambda)} c_{k\lambda s}. \quad (5.2)$$

The Fourier transform yields a  $2 \times 2$  matrix in sublattice space, which is diagonalized to arrive at

$$H_0 = \sum_{k\rho s} \mathcal{E}_k^\rho \phi_{k\rho s}^\dagger \phi_{k\rho s}, \quad \mathcal{E}_k^\rho = \rho \mathcal{E}_k = \rho |f(k)|, \quad (5.3)$$

where

$$f(k) = e^{ik_x} + 2e^{-ik_x/2} \cos(\sqrt{3}k_y/2) \quad \text{and} \quad \rho = \pm 1. \quad (5.4)$$

To clarify the physical meaning of  $\rho$ , we introduce the Fermi energy  $\mathcal{E}_F$ , defined such that all states with  $\mathcal{E}_k^\rho \leq \mathcal{E}_F$  are filled [5]. States above  $\mathcal{E}_F$  are called *particles* and states below  $\mathcal{E}_F$  are called *holes*. In our case  $\mathcal{E}_F = 0$  which means  $\rho = \pm 1$  states represent particles/holes.

In this representation the interaction part of the Hamiltonian can be split into a quadratic part,  $H_1$ , which we will refer to as the *mass term* and a quartic part,  $H_2$ , which we will call the *interaction vertex*. The mass term  $H_1$  is then

$$H_1 = -\frac{U}{2} \sum_{k\rho s} \phi_{k\rho s}^\dagger \phi_{k\rho s}. \quad (5.5)$$

For  $H_2$  we introduce the multi-index notation  $\mathbf{k} = (k, \rho)$  and define the quartic interaction vertex

$$V_{\mathbf{k}'\mathbf{l}'\mathbf{k}\mathbf{l}} = \frac{U}{4\Lambda} \delta_{\mathbf{k}'+\mathbf{l}',\mathbf{k}+\mathbf{l}} \left( 1 + \rho'\sigma'\rho\sigma e^{-i(\theta_k - \theta_{k'} + \theta_l - \theta_{l'})} e^{-i(k'+l'-k-l)\xi_b} \right), \quad e^{i\theta_k} = \frac{f(k)}{|f(k)|}, \quad (5.6)$$

where  $\delta_{\mathbf{k}'+\mathbf{l}',\mathbf{k}+\mathbf{l}}$  is defined modulo the BZ. Then the final Hamiltonian takes the following form

$$H = \sum_{\mathbf{k}s} \left( \mathcal{E}_{\mathbf{k}} - \frac{U}{2} \right) \phi_{\mathbf{k}s}^\dagger \phi_{\mathbf{k}s} + \sum_{\mathbf{k}'\mathbf{l}'\mathbf{k}\mathbf{l}} V_{\mathbf{k}'\mathbf{l}'\mathbf{k}\mathbf{l}} \phi_{\mathbf{k}'\uparrow}^\dagger \phi_{\mathbf{l}'\downarrow}^\dagger \phi_{\mathbf{k}\downarrow} \phi_{\mathbf{l}\uparrow}. \quad (5.7)$$

## 5.2 Thermal Field Theory

We operate within the interaction picture in *imaginary time*  $\tau \equiv it$ , and we perturb about the free, non-interacting ( $U = 0$ ) system. We designate the  $U$ -independent part of the Hamiltonian as the free Hamiltonian,  $H_0$ , and denote the remainder as the interaction term,  $H_I$ . Our free propagator is

$$G_{\mathbf{k}s}^0(\tau) = -\left\langle T_\tau [\phi_{\mathbf{k}s}(\tau) \phi_{\mathbf{k}s}^\dagger] \right\rangle_0, \quad (5.8)$$

where  $\langle T_\tau[\dots] \rangle_0$  stands for *thermal average* and  $T_\tau$  is a *time ordering* operator. The explicit time-dependent form of this quantity is:

$$G_{\mathbf{k}}^0(\tau) = e^{-\tau \mathcal{E}_{\mathbf{k}}} \begin{cases} -(1 - n_{\mathbf{k}}) & \tau > 0 \\ n_{\mathbf{k}} & \tau \leq 0 \end{cases} \quad \text{with} \quad n_{\mathbf{k}} = \frac{1}{e^{\beta \mathcal{E}_{\mathbf{k}}} + 1}, \quad (5.9)$$

where  $n_{\mathbf{k}}$  is the fermion number. Since  $G^0$  is spin independent we drop the  $s$ . This propagator is periodic in imaginary time, allowing us to express it in terms of a Fourier transform in  $\tau$ ,

$$G_{\mathbf{k}}^0(i\omega) = \int_0^\beta d\tau G_{\mathbf{k}}^0(\tau) e^{i\omega\tau} = \frac{1}{i\omega - \mathcal{E}_{\mathbf{k}}}, \quad \omega = \frac{\pi}{\beta}(2m+1) \quad m \in \mathbb{Z}. \quad (5.10)$$

The inverse transform is provided by the *Matsubara sum*

$$G_{\mathbf{k}}^0(\tau) = \frac{1}{\beta} \sum_{\omega} \frac{e^{-i\omega\tau}}{i\omega - \mathcal{E}_{\mathbf{k}}}. \quad (5.11)$$

To account for interactions, we introduce a quantity analogous to the  $S$ -matrix in ordinary QFT [6], allowing us to express the interacting propagator which we'll simply refer to as a *correlator*.

$$C_{\mathbf{k}}(\tau) = -\frac{\langle T_{\tau} [S(\beta) \phi_{\mathbf{k}s}(\tau) \phi_{\mathbf{k}s}^{\dagger}] \rangle_0}{\langle S(\beta) \rangle_0}, \quad S(\tau) = T_{\tau} \exp \left\{ -\int_0^{\tau} H_I(\tau') d\tau' \right\}. \quad (5.12)$$

According to Wick's theorem, thermal average of time-ordered product of the fermionic operators can be expressed as the sum of all possible *Wick contractions*, defined as

$$\phi_{\mathbf{k}s}^{\bullet}(\tau_1) \phi_{\mathbf{l}s'}^{\dagger}(\tau_2) = -\delta_{\mathbf{k}\mathbf{l}} \delta_{ss'} G_{\mathbf{k}}^0(\tau_1 - \tau_2). \quad (5.13)$$

Rather than computing each contraction explicitly, we employ a diagrammatic approach, using Feynman diagrams to systematically capture higher-order contributions. In this case, we have one propagator and two interaction vertices from  $H_1$  and  $H_2$ , respectively. The complete set of Feynman rules for our calculations is as follows:

$$\begin{array}{l} \longrightarrow \sim \frac{1}{i\omega - \mathcal{E}_{\mathbf{k}}} \equiv G_{\mathbf{k}}^0(i\omega) \\ \longrightarrow \blacksquare \longrightarrow \sim -\frac{U}{2} \end{array} \quad \begin{array}{l} \begin{array}{c} \mathbf{l} \downarrow \\ \swarrow \quad \searrow \\ \bullet \\ \nearrow \quad \nwarrow \\ \mathbf{k} \uparrow \quad \mathbf{k}' \uparrow \end{array} \\ \sim V_{\mathbf{k}'\mathbf{l}\mathbf{k}} \end{array} \quad (5.14)$$

In this way, we only have to keep track of topologically distinct Feynman diagrams instead of all the possible Wick contractions.

### 5.3 Solution

In order to obtain a non-perturbative correction to the propagator we utilize the *self-energy*  $\Sigma_{\mathbf{k}}(i\omega)$ , which is the sum of all 1 particle irreducible (1-PI) diagrams.  $\Sigma$  is a 2x2 matrix in the sub-lattice basis and in general not diagonal. The fully dressed correlator (double line) can then be expressed using Dyson's equation

$$\text{double line} = \text{propagator} + \text{propagator} \circledast \Sigma \text{ double line}.$$

Poles of the correlator provide the spectrum arising from self-interactions, leading to the *quantization condition* (QC).

$$\det \left( G_{\mathbf{k}}^0(i\omega)^{-1} - \Sigma_{\mathbf{k}}(i\omega) \right) \Big|_{i\omega=E_{\mathbf{k}}} = 0, \quad (5.15)$$

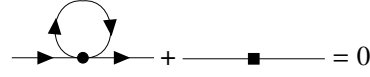
where  $E_{\mathbf{k}}$  is the interacting energy. Note that all temperature dependence (ie  $\beta$ -dependence) originates in  $\Sigma$ . To get the time-dependent correlator  $C_{\mathbf{k}}(\tau)$  we must perform a Matsubara sum. If  $\Sigma$  is diagonal we use standard complex integration techniques to rewrite the sum over frequencies  $\omega$  as a contour

integral which can be solved as a sum over the residues at the poles of the correlator [5].

$$C_{\mathbf{k}}(\tau) = \frac{1}{\beta} \sum_{\omega} \frac{e^{-i\omega\tau}}{i\omega - \mathcal{E}_{\mathbf{k}} - \Sigma_{\mathbf{k}}(i\omega)} = \sum_{z^*} \frac{e^{-z^*\tau}}{e^{-z^*\beta} + 1} \text{Res} \left( \frac{1}{z - \mathcal{E}_{\mathbf{k}} - \Sigma_{\mathbf{k}}(z)}, z = z^* \right). \quad (5.16)$$

Even if  $\Sigma$  is only approximately diagonal we can assume the off-diagonals to be zero with negligible error. We have also observed that for  $\Gamma$ ,  $M$  and  $K$  points self-energy is always diagonal.

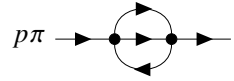
We calculate  $\Sigma$  to the leading non-trivial order in  $U$ . At  $\mathcal{O}(U)$  there are only two contributions, one from the mass term and the other from the interaction vertex. These contributions are constant and opposite in sign, canceling each other exactly. Diagrammatically the cancellation is given as



The diagram shows two terms separated by a plus sign. The first term is a horizontal line with a dot in the middle, and a loop above it consisting of two arrows forming a circle. The second term is a horizontal line with a square in the middle. The equation is set equal to zero.

$$= 0. \quad (5.17)$$

This implies that the leading order contribution must be at least  $\sim \mathcal{O}(U^2)$ . At this order we can use (5.17) and assume all diagrams containing ‘‘tadpoles’’ and mass terms to cancel and we are left with a single ‘‘sunset diagram’’:



The diagram shows a horizontal line with two dots in the middle, connected by a loop above and below. The equation is set equal to a sum over  $l'kl$  of  $|V_{pl'kl}|^2$  times a fraction.

$$p\pi \rightarrow \text{diagram} \rightarrow p\pi = \sum_{l'kl} |V_{pl'kl}|^2 \frac{n_{-l'} n_{\mathbf{k}} + (n_{l'} - n_{\mathbf{k}}) n_{-l}}{i\omega - (\mathcal{E}_{\mathbf{k}} - \mathcal{E}_{l'} + \mathcal{E}_l)}, \quad (5.18)$$

where we used shorthand  $-\mathbf{k} = (k, -\rho)$ , and also defined  $\mathbf{p} = (p, \pi)$  for external lines.

For the 2-site lattice there is only one momentum point  $\Gamma$ , therefore  $\mathcal{E}_{\mathbf{k}}^{\rho} = \rho \mathcal{E}_{\Gamma}$ . Here  $|V_{pl'kl}|^2$  simplifies to  $\frac{U^2}{4} \delta_{\pi\sigma', \rho\sigma}$ . At zero temperature the QC becomes a quadratic equation:

$$(E_{\Gamma}^{\pi} - \pi \mathcal{E}_{\Gamma})(E_{\Gamma}^{\pi} + 3\pi \mathcal{E}_{\Gamma}) - \frac{U^2}{4} = 0. \quad (5.19)$$

With the additional condition that  $E_{\Gamma}^{\pi}|_{U=0} = \pi \mathcal{E}_{\Gamma}$  we can analytically solve for the energy

$$E_{\Gamma}^{\pi} = \pi \mathcal{E}_{\Gamma} \left( \sqrt{\frac{U^2}{4\mathcal{E}_{\Gamma}^2} + 4} - 1 \right). \quad (5.20)$$

Even at  $T \neq 0$  the QC for 2-sites is a cubic polynomial, making it analytically solvable. However, exact expressions tend to be cumbersome and do not offer substantial insight. For larger lattices, solving the QC analytically becomes infeasible so we can use numerical methods to find the roots of (5.15). Due to the form of (5.18), QC is always a rational function of  $E_{\mathbf{k}}$ , meaning we can also find residues and perform the summation in (5.16). For larger lattices, however, accumulation of numerical errors precludes us from performing the residue sum to a sufficient degree of accuracy, forcing us to fall back on HMC. In principle, one could use arbitrary precision methods, albeit with a significant performance hit.

## 5.4 Results

### 5.4.1 $T = 0$

For the 2-site and 4-site systems, we compare perturbative results with exact solutions to assess the validity of the leading-order (LO) approximation. First, in the zero-temperature limit ( $\beta \rightarrow \infty$ ), we examine the dependence of energy on  $U$  alone. In the 2-site case perturbative expression (5.20) is equal to the exact solution given in [46]. For the 2-site problem, higher-order self-energy contributions vanish at  $T = 0$ , making it exactly solvable in our formalism.

For the 4-site system, which includes two momentum points in the Brillouin Zone (BZ) –  $\Gamma$  and  $M$  – the discrepancy between perturbative and exact results is more pronounced. Nevertheless, the agreement remains excellent for both momentum points, even up to  $U = 20$ , which is well into the non-perturbative regime, see Fig. 5.3.

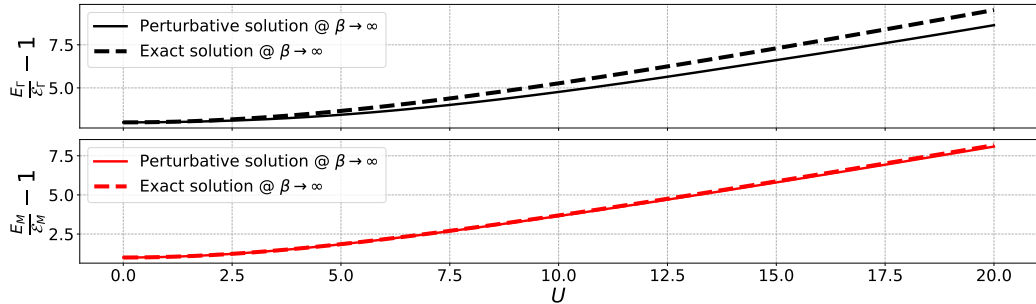


Figure 5.3: Energy dependence on  $U$  for the 4-site system at  $\beta \rightarrow \infty$ . Plots are shown for  $\Gamma$  and  $M$  points, demonstrating good agreement between perturbative and exact solutions even for large values of  $U$ .

### 5.4.2 $T \neq 0$

To examine finite-temperature behavior, we calculate the time-dependent correlators using equation 5.16. Notably, the particle and hole propagators are mirror images around  $\tau = \beta/2$ . For the 2-site system, the perturbative and exact calculations are in close agreement, although deviations become noticeable at very high values of  $U$  due to higher-order contributions at finite temperatures.

For the 4-site system, we analyze correlators at the  $\Gamma$  and  $M$  points. The deviation between perturbative and exact results is more pronounced here than in the 2-site case. However, the agreement is still good, extending beyond typical perturbative limits of  $U$ .

For lattices larger than 4-sites, exact solutions become computationally prohibitive, necessitating the use of Hybrid Monte Carlo (HMC) simulations [28, 37, 47]. In Fig. 5.6, we present the correlators for a  $2 \times 3$  graphene. Although the Brillouin Zone (BZ) contains 6 momentum points, only 3 unique correlators emerge, labeled as  $\Gamma$ ,  $M$ , and  $A$ . The latter correlator provides an example where the self-energy matrix  $\Sigma$  is not strictly diagonal. Despite this, we can approximate a solution to the quantization condition. Our calculations reveal that the off-diagonal terms are an order of magnitude smaller than the diagonal terms. If we denote this difference by  $\epsilon$ , by setting these off-diagonal terms to zero, we incur an error on the order of  $\epsilon^2$ , which remains negligible in this context.

As in the 2- and 4-site examples, we find very good agreement between our perturbative and HMC calculation for couplings up to  $U = 3$ . However, at  $U = 4$  we see definitive discrepancies in the

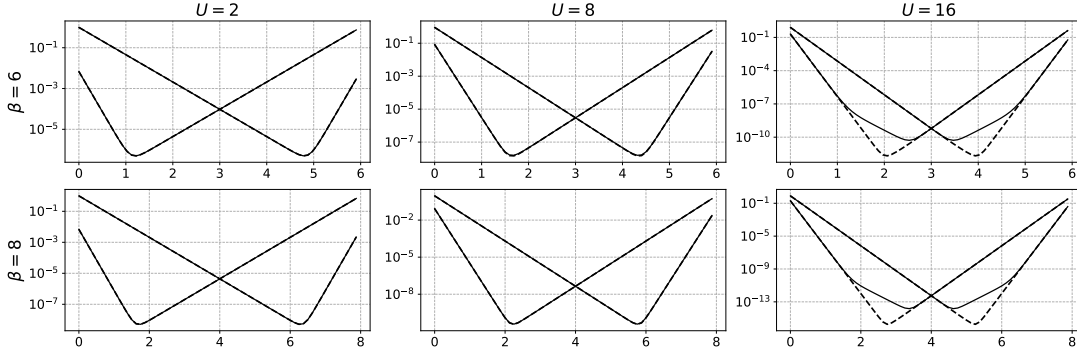


Figure 5.4:  $C_k(\tau)$  vs.  $\tau$  for the 2-site system with  $U = 2, 8, 16$  and  $\beta = 8, 10$ . Deviations between perturbative (dashed) and exact (solid) results only become apparent at very large  $U$ . Even at  $U = 8$ , a strongly non-perturbative value, the results show close agreement.

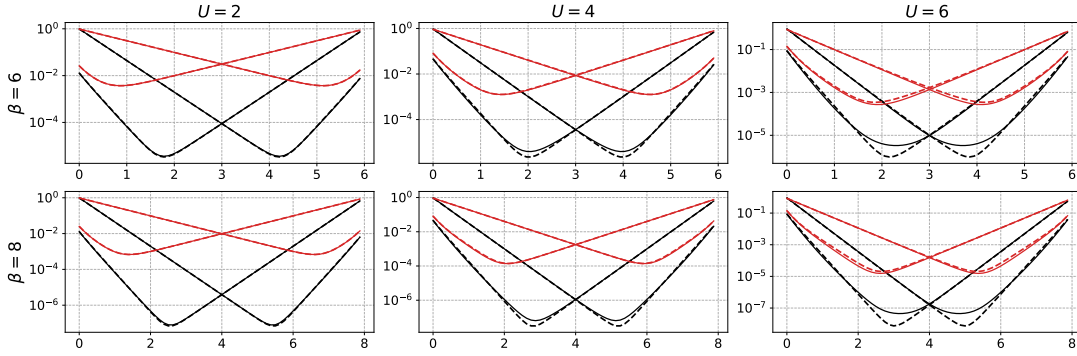


Figure 5.5:  $C_k(\tau)$  vs.  $\tau$  for the 4-site system at  $\Gamma$  (black) and  $M$  (red) points, with  $U = 2, 4, 6$  and  $\beta = 6, 8$ . Deviations between perturbative (dashed) and exact (solid) results are more apparent than in the 2-site case but still show strong agreement for high values of  $U$ .

correlators.

## 5.5 Summary and Outlook

This proceeding presents perturbative calculations of the self-energy  $\Sigma$  in thermal field theory applied to the Hubbard model on a graphene lattice, computed up to the leading non-trivial order,  $\mathcal{O}(U^2)$ . We have calculated the zero-temperature energy shift, achieving perfect agreement with exact results for the 2-site system and strong agreement for the 4-site system, even for non-perturbative values as high as  $U = 20$ . We further analyzed the time evolution of correlators for both 2-site and 4-site models, observing remarkable alignment between perturbative and exact results despite the large  $U$  values. Additionally, we investigated correlators for  $2 \times 3$  graphene sheet and compared our calculations to HMC simulated data for up to  $U = 3$  demonstrating good consistency. Only at larger  $U$  do we see a discrepancy between perturbative and HMC results. In the future we will use our formalism here to deduce the finite-temperature dependence of eigenenergies obtained from HMC simulations within a

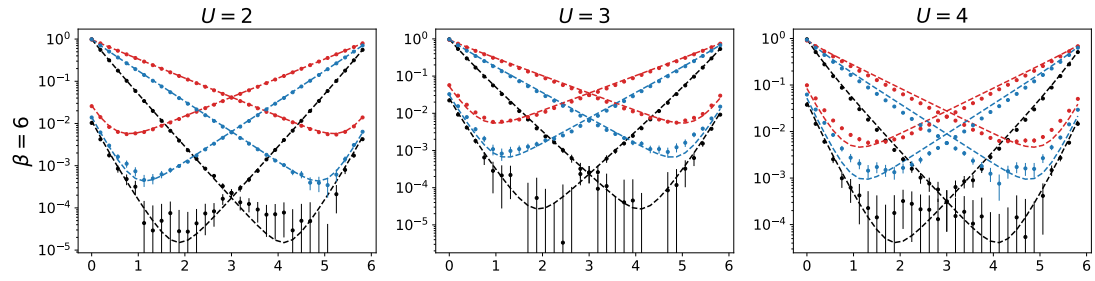


Figure 5.6:  $C_{\mathbf{k}}(\tau)$  vs.  $\tau$  for  $2 \times 3$  graphene at  $U = 2, 3$ , and  $4$ , all with  $\beta = 6$ . These are  $\Gamma$  (black),  $M$  (red) and  $A$  (blue) points. Dashed lines are perturbative correlators and the dots are from an HMC simulation. Agreement is very good. Even for  $A$  which is not diagonal in particle-hole basis. However, off-diagonal terms are small enough to treat it as approximately diagonal. To observe the deviation one has to go up to  $U = 4$ .

finite temporal volume.

---

## Conclusion

---

In summary, this thesis has examined the fundamental electronic characteristics of low-dimensional graphene sheets, nanoribbons and other complex geometries, with a particular focus on various types of localized quantum states in hybrid ribbons [1–3], the influence of finite-temperature effects on quasi-particle energies and two-point correlation functions [4], and the stability of quantum states under perturbations typical of Hubbard-type models [1, 2, 4]. While the potential applications of these findings in quantum computing present an exciting long-term aspiration, the primary aim of this research has been to enhance our understanding of the intrinsic material properties and interactions that could support future quantum technologies.

We investigated the role of interactions and external perturbations in shaping the electronic properties of graphene-based systems, focusing on graphene nanoribbons (GNRs) and hybrid ribbon configurations. Our work was motivated by the need to understand how localized states at junctions, governed by symmetry and topology, respond to finite-temperature effects as well as interactions which we chose to model using Hubbard-like models. This research builds upon established models and methods in condensed matter physics, like the Kitaev chain or thermal perturbation theory and explores these frameworks to hexagonal lattice systems and hybrid structures.

A central component of this study was the exploration of localized states and their stability under the Hubbard and BCS-Hubbard interactions, the latter being an exactly solvable extension that includes superconducting pairing  $\Delta$ . This model incorporates nearest-neighbor hopping  $t$ , on-site Hubbard interaction  $U$ , and pairing interactions, providing an ideal platform for investigating the interplay between superconductivity, interactions, and topology. When  $t = \Delta$ , the BCS-Hubbard model becomes exactly solvable, enabling us to derive closed-form expressions for the energy spectrum and wavefunctions across a broad range of interaction strengths. Although realizing superconductive pairing in physical systems remains challenging, the mathematical framework offers valuable insights into interaction-driven phenomena.

We applied the BCS-Hubbard model to hexagonal carbon nanoribbons (CNRs) with zigzag (ZNR) and armchair (ANR) geometries. These quasi-one-dimensional systems exhibit unique electronic properties due to their edge structures and confinement effects. Our analysis showed that for  $U = 0$ , armchair ribbons with widths  $N = 3m + 2$  (where  $m$  is an integer) exhibit gapless metallic behavior. As  $U$  increases, an energy gap opens, indicating a transition to an insulating state. In the  $U \rightarrow \infty$  limit, the system becomes an atomic insulator, with electrons tightly bound to atomic cores. These transitions illustrate the complex interplay between geometry, interactions, and superconducting pairing.

The starting objective of this research was to investigate the robustness of localized states at the junctions of hybrid GNRs. Our focus was on periodic hybrid nanoribbons, such as 7/9- and 13/15-hybrid ribbons, where sections of different widths are joined. We employed both the BCS-Hubbard model and standard Hubbard interactions simulated via Hybrid Monte Carlo (HMC) to study these systems. By extracting site-dependent quasi-particle wavefunction densities, we provided a detailed analysis of the spatial distribution of electronic states at the junctions.

A notable result of our work is the identification of two distinct types of localized states: the familiar, sharply defined *Fuji* localizations and a newly discovered type referred to as *Kilimanjaro* localizations. Fuji localizations are highly concentrated at the junctions and occur only when the width  $N$  of the narrower ribbon satisfies  $N \pmod{3} = 1$ . In contrast, Kilimanjaro localizations spread over an extended segment of the ribbon and are more sensitive to the junction's geometry.

In previous studies, the stability of localized states was attributed to differing topological charges of the ribbons. However, our findings revealed counterexamples where localization persists even without variations in the topological invariant. By analyzing the long-wavelength limit of a tight-binding model, we demonstrated that wavefunction localization can arise from evanescent wave-like behavior rather than purely topological protection. Our effective theory decomposes the Hamiltonian into multiple Dirac-like sectors, each characterized by a massive Dirac equation, providing a more nuanced explanation of localization phenomena in finite and periodic systems.

We extended our analysis to finite-temperature regimes to examine the resilience of localized states under thermal perturbations. By deriving time-dependent correlation functions and comparing them with numerical results from HMC simulations, we demonstrated that our perturbative treatment remains accurate even for large interaction strengths. This accuracy underscores the robustness of our framework. For instance, at the  $\Gamma$ -point of a  $3 \times 3$  graphene lattice, we observed a plateau in the correlation function due to Dirac  $K$ -points—a feature initially suspected to be a numerical artifact but later confirmed through precise simulations.

Our study also highlighted the importance of chiral symmetry in suppressing linear corrections in  $U$ . At half-filling, first-order corrections to the self-energy vanish due to symmetry constraints, and the leading-order contributions scale as  $O(U^2)$ . This behavior was further validated by introducing a staggered mass term that breaks sublattice symmetry, reinstating linear terms in  $U$ . The absence of linear corrections, even when deviating from half-filling, reinforces the idea that symmetry-driven mechanisms govern the low-energy properties of the system.

We explored the implications of these findings for GNRs, which exhibit width-dependent bandgaps and edge-localized states. By analyzing structural effects, such as ribbon width and edge symmetry, we demonstrated how these factors influence the electronic response. At specific widths, zero-mass excitations emerge, dominating the electronic properties and making GNRs an ideal platform for studying interaction-driven phenomena.

Our results suggest that hybrid GNRs could serve as robust carriers of quantum information, with potential applications in quantum dot engineering and fault-tolerant quantum computing. By carefully engineering the junction geometry and tuning interaction strengths, it is possible to construct nanoribbon-based quantum devices with tailored energy spectra and enhanced stability against decoherence. We also investigated the effects of a finite temporal volume, revealing that thermal fluctuations shift excitation energies but do not eliminate the robustness of localized states. This resilience underscores the potential applicability of GNRs in real-world nanoscale devices.

The broader implications of this thesis lie in its ability to bridge theoretical predictions and practical applications. By elucidating the role of Hubbard interactions, superconducting pairing, and thermal

---

effects in graphene-based systems, our study provides a comprehensive framework for designing and optimizing nanoscale devices. The insights gained contribute to the understanding of interaction-driven phenomena in strongly correlated systems and pave the way for future explorations of exotic quantum phases in low-dimensional materials.

Building upon the findings of this thesis, several promising avenues for future research can be pursued.

One key direction is to extend the use of the thermal field theory formalism to more complex geometries, including various types of graphene-based structures and hybrid nanoribbons with intricate boundary conditions. This approach will provide a deeper understanding of how thermal fluctuations and interaction effects manifest in different configurations and contribute to the broader study of low-dimensional quantum systems.

Another important focus is the incorporation of higher order perturbative contributions from the Hubbard interaction, like next-to-leading order (NLO) which would be  $O(U^3)$ . This refinement aims to enhance the precision of numerical simulations and analytical predictions, particularly for capturing interaction-driven corrections and subtle effects that become prominent in specific parameter regimes. Such higher-order contributions will allow for more accurate modeling of realistic systems and improve comparisons with experimental results.

Additionally, an exciting avenue for exploration involves establishing the connection between the effective model of hybrid ribbons and the topological charge of the Su-Schrieffer-Heeger (SSH) model under periodic boundary conditions. This investigation will help elucidate the topological properties of hybrid nanoribbons and their potential role in supporting robust quantum states, which are relevant for applications in topological quantum computing and fault-tolerant quantum information processing.

Further research directions also include studying the resilience of localized states under additional perturbations, such as disorder and external fields. By incorporating more complex interactions and analyzing larger lattice systems, future work aims to refine the understanding of the interplay between topology, symmetry, and interactions in hybrid graphene systems. These efforts underscore the significance of materials science in advancing the field of quantum information technology and highlight the challenges of bridging the gap between theoretical predictions and practical implementations.

Ultimately, while this thesis focuses on foundational research rather than immediate technological application, its goal from the outset has been to contribute to the broader scientific and technological advancement of quantum technologies and nanoelectronics. By deepening our understanding of the underlying properties of 2D materials, this work aims to support future investigations and pave the way for breakthroughs in quantum devices, including innovations in computation, information storage, and energy-efficient electronics.



---

## Useful information

---

### A.1 Commutator/Anticommutators

$$[A, B] = AB - BA, \quad (\text{A.1})$$

$$\{A, B\} = AB + BA, \quad (\text{A.2})$$

$$[A, BC] = [A, B]C + B[A, C], \quad (\text{A.3})$$

$$[AB, C] = A[B, C] + [A, C]B, \quad (\text{A.4})$$

$$[A, BC] = \{A, B\}C - B\{A, C\}, \quad (\text{A.5})$$

$$[AB, C] = A\{B, C\} - \{A, C\}B. \quad (\text{A.6})$$

### A.2 Matsubara sums

The inverse Fourier transform is expressed as Matsubara sum

$$\frac{1}{\beta} \sum_{i\omega} \frac{e^{-i\omega\tau}}{i\omega - \mathcal{E}} \quad (\text{A.7})$$

can be evaluated in the following way. The sum is defined over odd frequencies  $i\omega = \frac{\pi}{\beta}(2n + 1)$ . Notice that these are exactly the poles of the function

$$f(z) = \frac{1}{e^{-\beta z} + 1}. \quad (\text{A.8})$$

With this in mind define a complex integral

$$\lim_{R \rightarrow \infty} \oint_{|z| < R} F(z) f(z) e^{\tau z}. \quad (\text{A.9})$$

If  $F(z)$  vanishes as  $|z| \rightarrow \infty$  the integral is zero. On the other hand Cauchy formula tells us that this integral is a sum of all residues inside the contour.

$$0 = \frac{1}{\beta} \sum_{i\omega} e^{-i\omega\tau} F(i\omega) + \sum_{z^*} \frac{e^{-\tau z^*}}{e^{-\beta z^*} + 1} \text{Res}(F(z), z^*), \quad (\text{A.10})$$

where  $\beta$  comes from the residue of  $f(i\omega)$ . It is easy to see that for simple propagator one recovers [Equation 1.29](#)

$$\frac{1}{\beta} \sum_{i\omega} \frac{e^{-i\omega\tau}}{i\omega - \mathcal{E}} = \frac{e^{-\tau\mathcal{E}}}{e^{-\beta\mathcal{E}} + 1}. \quad (\text{A.11})$$

In general

$$\frac{1}{\beta} \sum_{\omega} F(i\omega) = \begin{cases} \sum_{z_0} \frac{\text{Res}(F(z), z_0)}{e^{z_0\beta} + 1} & \omega = \frac{\pi}{\beta}(2n+1), n \in \mathbb{Z} \\ \sum_{z_0} \frac{\text{Res}(F(z), z_0)}{e^{z_0\beta} - 1} & \omega = \frac{\pi}{\beta}(2n), n \in \mathbb{Z} \end{cases}. \quad (\text{A.12})$$

For poles of order  $n$  we have

$$\text{Res}(F(z), z_0) = \frac{1}{(n-1)!} \lim_{z \rightarrow z_0} \frac{d^{n-1}}{dz^{n-1}} ((z - z_0)^n F(z)), \quad (\text{A.13})$$

$$\frac{1}{\beta} \sum_{\omega' \text{ odd}} G_1^0(\omega') G_2^0(\omega' + \omega) = \frac{n_1 - n_2}{i\omega - \mathcal{E}_2 + \mathcal{E}_1} = (n_1 - n_2) G_{2-1}^0(\omega), \quad (\text{A.14})$$

$$\frac{1}{\beta} \sum_{\omega' \text{ even}} \frac{1}{i\omega' - \mathcal{E}_1} \frac{1}{i\omega' - \mathcal{E}_2} = \frac{n_1 - n_2}{(1 - 2n_1)(1 - 2n_2)} \frac{1}{\mathcal{E}_1 - \mathcal{E}_2}. \quad (\text{A.15})$$

---

## Detailed calculations

---

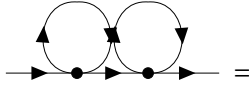
$$\begin{aligned}
 & \rightarrow \blacksquare \rightarrow = \\
 & -\frac{U}{2} \int_0^\beta d\tau_1 e^{i\omega\tau_1} \int_0^\beta d\tau \sum_{ks} \langle T_\tau [\phi_{pr}(\tau_1) \phi_{ks}^\dagger(\tau)] \rangle_0 \langle T_\tau [\phi_{ks}(\tau) \phi_{pr}^\dagger] \rangle_0 \\
 & = -\frac{U}{2} \int_0^\beta d\tau_1 e^{i\omega\tau_1} \int_0^\beta d\tau \sum_{ks} (-G_{pr}^0(\tau_1 - \tau)) (-G_{pr}^0(\tau)) \delta_{pk} \delta_{sr} \\
 & = -\frac{U}{2} \int_0^\beta d\tau_1 e^{i\omega\tau_1} \int_0^\beta d\tau \frac{1}{\beta^2} \sum_{\omega_1, \omega_2} G_{pr}^0(\omega_1) G_{pr}^0(\omega_2) e^{-i\omega_1(\tau_1 - \tau)} e^{-i\omega_2\tau} \\
 & = -\frac{U}{2} \int_0^\beta d\tau_1 \int_0^\beta d\tau \frac{1}{\beta^2} \sum_{\omega_1, \omega_2} G_{pr}^0(\omega_1) G_{pr}^0(\omega_2) e^{i(\omega - \omega_1)\tau_1} e^{i(\omega_1 - \omega_2)\tau} \\
 & = -\frac{U}{2} \frac{1}{\beta^2} \sum_{\omega_1, \omega_2} G_{pr}^0(\omega_1) G_{pr}^0(\omega_2) \beta \delta_{\omega\omega_1} \beta \delta_{\omega_1\omega_2} \\
 & = -\frac{U}{2} G_{pr}^0(\omega) G_{pr}^0(\omega). \tag{B.1}
 \end{aligned}$$



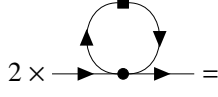
---



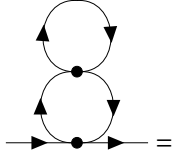
$$\begin{aligned}
& -\frac{(-)^2}{2} \left(-\frac{U}{2}\right)^2 \sum_{\substack{k,l \\ r,s}} \int_{1,2} \langle T_\tau [\phi_{kr}^\dagger(1) \phi_{kr}(1) \phi_{ls}^\dagger(2) \phi_{ls}(2) \phi_{p\uparrow}(3) \phi_{p\uparrow}^\dagger] \rangle_0 \\
& = -\frac{U^2}{8} \int_{1,2} \sum_{\substack{k,l \\ r,s}} (-G_{kr}^0(\tau_1 - \tau_2)) \delta_{kl}^{rs} (-G_{p\uparrow}^0(\tau_3 - \tau_1)) \delta_{kp}^{r\uparrow} (-G_{p\uparrow}^0(\tau_2)) \delta_{lp}^{s\uparrow} \\
& \quad + (1, k, \rho, r \leftrightarrow 2, l, \sigma, s) \\
& = \frac{U^2}{4} \int_{1,2} G_{p\uparrow}^0(\tau_1 - \tau_2) G_{p\uparrow}^0(\tau_3 - \tau_1) G_{p\uparrow}^0(\tau_2). \tag{B.3}
\end{aligned}$$



$$\begin{aligned}
& -\frac{(-)^2}{2} \sum_{\substack{k'l'kl \\ k''l''k''l''}} V_{k'l'kl} V_{k''l''k''l''} \int_{1,2} \langle T_\tau [\phi_{k'\uparrow}^\dagger(1) \phi_{l'\downarrow}^\dagger(1) \phi_{l\downarrow}(1) \phi_{k\uparrow}(1) \\
& \quad \phi_{k''\uparrow}^\dagger(2) \phi_{l''\downarrow}^\dagger(2) \phi_{l''\downarrow}(2) \phi_{k''\uparrow}(2) \phi_{p\uparrow}(3) \phi_{p\uparrow}^\dagger] \rangle_0 \\
& = -\frac{1}{2} \sum_{\substack{k'l'kl \\ k''l''k''l''}} V_{k'l'kl} V_{k''l''k''l''} \int_{1,2} \langle T_\tau [\phi_{k'\uparrow}^\dagger(1) G_{l\downarrow}^0(0^-) \delta_{ll'} \phi_{k\uparrow}(1) \\
& \quad \phi_{k''\uparrow}^\dagger(2) G_{l''\downarrow}^0(0^-) \delta_{l''l''} \phi_{k''\uparrow}(2) \phi_{p\uparrow}(3) \phi_{p\uparrow}^\dagger] \rangle_0 \\
& = -\frac{1}{2} \sum_{\substack{k'kl \\ k''k''l''}} V_{k'kl} V_{k''l''k''l''} n_l n_{l''} \int_{1,2} (-G_{k\uparrow}^0(\tau_1 - \tau_2)) \delta_{kk''} (-G_{p\uparrow}^0(\tau_3 - \tau_1)) \delta_{k'p} (-G_{p\uparrow}^0(\tau_2)) \delta_{k''p} \\
& \quad + (1, k'', k''' \leftrightarrow 2, k, k') \\
& = \sum_{kl''} V_{plkl} V_{kl''pl''} n_l n_{l''} \int_{1,2} G_{k\uparrow}^0(\tau_1 - \tau_2) G_{p\uparrow}^0(\tau_3 - \tau_1) G_{p\uparrow}^0(\tau_2) \\
& = \frac{U^2}{16\Lambda^2} \sum_{kl''} \delta_{pk} \left| 1 + \pi\rho e^{i(\theta_k - \theta_p)} \right|^2 n_l n_{l''} \int_{1,2} G_{k\uparrow}^0(\tau_1 - \tau_2) G_{p\uparrow}^0(\tau_3 - \tau_1) G_{p\uparrow}^0(\tau_2) \\
& = \frac{U^2}{4} \sum_k \delta_{pk} \int_{1,2} G_{k\uparrow}^0(\tau_1 - \tau_2) G_{p\uparrow}^0(\tau_3 - \tau_1) G_{p\uparrow}^0(\tau_2) \tag{B.4} \\
& = \frac{U^2}{4} \int_{1,2} G_{p\uparrow}^0(\tau_1 - \tau_2) G_{p\uparrow}^0(\tau_3 - \tau_1) G_{p\uparrow}^0(\tau_2).
\end{aligned}$$



$$\begin{aligned}
 2 \times & \text{---} \bullet \text{---} = \\
 & -2 \frac{(-)^2}{2!} \left( -\frac{U}{2} \right) \sum_{\substack{k', l', k \\ l, q, r}} V_{k' l' k l} \int_{1,2} \langle T_\tau [\phi_{q r}^\dagger(1) \phi_{q r}(1) \phi_{k' \uparrow}^\dagger(2) \phi_{l' \downarrow}^\dagger(2) \phi_{l \downarrow}(2) \phi_{k \uparrow}(2) \phi_{p \uparrow}(3) \phi_{p \uparrow}^\dagger] \rangle_0 \\
 & = \frac{U}{2} \sum_{\substack{k', l', k \\ l, q, r}} V_{k' l' k l} \int_{1,2} \langle T_\tau [\phi_{q r}^\dagger(1) \phi_{q r}(1) G_{p \uparrow}^0(\tau_3 - \tau_2) \delta_{k' p} \phi_{l' \downarrow}^\dagger(2) \phi_{l \downarrow}(2) G_{p \uparrow}^0(\tau_2) \delta_{k p}] \rangle_0 \\
 & = \frac{U}{2} \sum_{\substack{l', l \\ q, r}} V_{p l' p l} \int_{1,2} G_{p \uparrow}^0(\tau_3 - \tau_2) G_{p \uparrow}^0(\tau_2) \langle T_\tau [\phi_{q r}^\dagger(1) \phi_{q r}(1) \phi_{l' \downarrow}^\dagger(2) \phi_{l \downarrow}(2)] \rangle_0 \\
 & = \frac{U}{2} \sum_{\substack{l', l \\ q, r}} V_{p l' p l} \int_{1,2} G_{p \uparrow}^0(\tau_3 - \tau_2) G_{p \uparrow}^0(\tau_2) G_{q r}^0(\tau_2 - \tau_1) \delta_{q l}^{r \downarrow} (-G_{q r}^0(\tau_1 - \tau_2)) \delta_{q l}^{r \downarrow} \\
 & = -\frac{U}{2} \sum_q V_{p q p q} \int_{1,2} G_{p \uparrow}^0(\tau_3 - \tau_2) G_{p \uparrow}^0(\tau_2) G_{q \downarrow}^0(\tau_2 - \tau_1) G_{q \downarrow}^0(\tau_1 - \tau_2) \quad (\text{B.5}) \\
 & = -\frac{U^2}{4\Lambda} \sum_q \int_{1,2} G_{p \uparrow}^0(\tau_3 - \tau_2) G_{p \uparrow}^0(\tau_2) G_{q \downarrow}^0(\tau_2 - \tau_1) G_{q \downarrow}^0(\tau_1 - \tau_2).
 \end{aligned}$$



$$\begin{aligned}
&= -\frac{(-)^2}{2} \sum_{\substack{k'l'kl \\ k''l''k''l''}} V_{k'l'kl} V_{k''l''k''l''} \int_{1,2} \langle T_\tau [\phi_{k'\uparrow}^\dagger(1) \phi_{l'\downarrow}^\dagger(1) \phi_{l\downarrow}(1) \phi_{k\uparrow}(1) \\
&\quad \phi_{k''\uparrow}^\dagger(2) \phi_{l''\downarrow}^\dagger(2) \phi_{l''\downarrow}(2) \phi_{k''\uparrow}(2) \phi_{p\uparrow}(3) \phi_{p\uparrow}^\dagger] \rangle_0 \\
&= -\frac{1}{2} \sum_{\substack{k'l'kl \\ k''l''k''l''}} V_{k'l'kl} V_{k''l''k''l''} \int_{1,2} G_{k\uparrow}^0(0^-) \delta_{k'k} (-G_{l'\downarrow}^0(\tau_2 - \tau_1)) \delta_{l''l'} G_{l\downarrow}^0(\tau_1 - \tau_2) \delta_{l''l} \\
&\quad G_{p\uparrow}^0(\tau_3 - \tau_2) \delta_{k''p} G_{p\uparrow}^0(\tau_2) \delta_{k''p} + (1, \dots \leftrightarrow 2, \dots) \\
&= \sum_{l'kl} V_{kl'l'kl} V_{plpl} n_k \int_{1,2} G_{l'\downarrow}^0(\tau_2 - \tau_1) G_{l\downarrow}^0(\tau_1 - \tau_2) G_{p\uparrow}^0(\tau_3 - \tau_2) G_{p\uparrow}^0(\tau_2) \\
&= \sum_{l'kl} \frac{U}{4\Lambda} \delta_{l'l'} \left(1 + \sigma \sigma' e^{i(\theta_l - \theta_{l'})}\right) \frac{U}{2\Lambda} n_k \int_{1,2} G_{l'\downarrow}^0(\tau_2 - \tau_1) G_{l\downarrow}^0(\tau_1 - \tau_2) G_{p\uparrow}^0(\tau_3 - \tau_2) G_{p\uparrow}^0(\tau_2) \\
&= \frac{U^2}{4\Lambda} \sum_{l'l} \delta_{l'l} \int_{1,2} G_{l'\downarrow}^0(\tau_2 - \tau_1) G_{l\downarrow}^0(\tau_1 - \tau_2) G_{p\uparrow}^0(\tau_3 - \tau_2) G_{p\uparrow}^0(\tau_2) \quad (\text{B.6}) \\
&= \frac{U^2}{4\Lambda} \sum_l \int_{1,2} G_{l\downarrow}^0(\tau_2 - \tau_1) G_{l\downarrow}^0(\tau_1 - \tau_2) G_{p\uparrow}^0(\tau_3 - \tau_2) G_{p\uparrow}^0(\tau_2).
\end{aligned}$$

$$\begin{aligned}
 & \text{---} \bullet \begin{array}{c} \circlearrowleft \\ \circlearrowright \end{array} \text{---} = \\
 & -\frac{(-)^2}{2} \sum_{\substack{k'l'kl \\ k''l''k''l''}} V_{k'l'kl} V_{k''l''k''l''} \int_{1,2,3} e^{i\omega\tau_3} \langle T_\tau [\phi_{k'\uparrow}^\dagger(1) \phi_{l'\downarrow}^\dagger(1) \phi_{l\downarrow}(1) \phi_{k\uparrow}(1) \\
 & \quad \phi_{k''\uparrow}^\dagger(2) \phi_{l''\downarrow}^\dagger(2) \phi_{l''\downarrow}(2) \phi_{k''\uparrow}(2) \phi_{p\uparrow}(3) \phi_{p\uparrow}^\dagger] \rangle_0 \\
 & = -\frac{1}{2} \sum_{\substack{k'l'kl \\ k''l''k''l''}} V_{k'l'kl} V_{k''l''k''l''} \int_{1,2,3} e^{i\omega\tau_3} \langle T_\tau [G_{p\uparrow}^0(\tau_3 - \tau_1) \delta_{k'p} \phi_{l'\downarrow}^\dagger(1) \phi_{l\downarrow}(1) \phi_{k\uparrow}(1) \\
 & \quad \phi_{k''\uparrow}^\dagger(2) \phi_{l''\downarrow}^\dagger(2) \phi_{l''\downarrow}(2) G_{p\uparrow}^0(\tau_2) \delta_{k''p}] \rangle_0 \\
 & = -\frac{1}{2} \sum_{\substack{l'kl \\ k''l''l''}} V_{p'l'kl} V_{k''l''p'l''} \int_{1,2,3} e^{i\omega\tau_3} (-G_{k\uparrow}^0(\tau_1 - \tau_2)) \delta_{k''k} (-G_{l\downarrow}^0(\tau_1 - \tau_2)) \delta_{l''l} G_{l'\downarrow}^0(\tau_2 - \tau_1) \delta_{l''l'} \\
 & \quad G_{p\uparrow}^0(\tau_3 - \tau_1) G_{p\uparrow}^0(\tau_2) + (1, \dots \leftrightarrow 2, \dots) \\
 & = -\sum_{l'kl} V_{p'l'kl} V_{klp'l'} \int_{1,2,3} e^{i\omega\tau_3} G_{k\uparrow}^0(\tau_1 - \tau_2) G_{l\downarrow}^0(\tau_1 - \tau_2) G_{l'\downarrow}^0(\tau_2 - \tau_1) G_{p\uparrow}^0(\tau_3 - \tau_1) G_{p\uparrow}^0(\tau_2) \\
 & = -\sum_{l'kl} |V_{p'l'kl}|^2 \frac{1}{\beta^5} \sum_{\{\omega_i\}} \int_{1,2,3} G_{k\uparrow}^0(\omega_1) G_{l\downarrow}^0(\omega_2) G_{l'\downarrow}^0(\omega_3) G_{p\uparrow}^0(\omega_4) G_{p\uparrow}^0(\omega_5) \\
 & \quad \times e^{i(\omega - \omega_4)\tau_3} e^{-i(\omega_1 + \omega_2 - \omega_3 - \omega_4)\tau_1} e^{i(\omega_1 + \omega_2 - \omega_3 - \omega_5)\tau_2} \\
 & = -\sum_{l'kl} |V_{p'l'kl}|^2 \frac{1}{\beta^5} \sum_{\{\omega_i\}} \int_2 G_{k\uparrow}^0(\omega_1) G_{l\downarrow}^0(\omega_2) G_{l'\downarrow}^0(\omega_3) G_{p\uparrow}^0(\omega_4) G_{p\uparrow}^0(\omega_5) \\
 & \quad \times \beta \delta_{\omega, \omega_4} \beta \delta_{\omega_1 + \omega_2, \omega_3 + \omega_4} \beta \delta_{\omega_4, \omega_5} \\
 & = -\sum_{l'kl} |V_{p'l'kl}|^2 \frac{1}{\beta^2} \sum_{\omega' \omega_1} G_{k\uparrow}^0(\omega_1) G_{l'\downarrow}^0(\omega_1 - \omega') G_{p\uparrow}^0(\omega) G_{l\downarrow}^0(\omega - \omega') G_{p\uparrow}^0(\omega).
 \end{aligned} \tag{B.7}$$

We amputate the diagram to get only the 1PI contribution

$$\begin{aligned}
& - \sum_{l'kl} |V_{pl'kl}|^2 \frac{1}{\beta^2} \sum_{\omega', \omega_1} G_{k\uparrow}^0(\omega_1) G_{l'\downarrow}^0(\omega_1 - \omega') G_{l\downarrow}^0(\omega - \omega') \\
& = - \sum_{l'kl} |V_{pl'kl}|^2 \frac{1}{\beta} \sum_{\omega'} \frac{n_{l'} - n_k}{i\omega' - (\mathcal{E}_k^\rho - \mathcal{E}_{l'}^{\sigma'})} \frac{1}{i\omega - i\omega' - \mathcal{E}_l^\sigma + \mu} \\
& = - \sum_{l'kl} |V_{pl'kl}|^2 \frac{-1}{\beta} \sum_{\omega'} \frac{n_{l'} - n_k}{i\omega' - (\mathcal{E}_k^\rho - \mathcal{E}_{l'}^{\sigma'})} \frac{1}{i\omega' - (i\omega - \mathcal{E}_l^\sigma + \mu)} \\
& = - \sum_{l'kl} |V_{pl'kl}|^2 (n_{l'} - n_k) \frac{n_{k-l'}^-}{\mathcal{E}_k^\rho - \mathcal{E}_{l'}^{\sigma'} - (i\omega - \mathcal{E}_l^\sigma + \mu)} + \frac{n_{i\omega-l}^-}{i\omega - \mathcal{E}_l^\sigma + \mu - (\mathcal{E}_k^\rho - \mathcal{E}_{l'}^{\sigma'})} \\
& = \sum_{l'kl} |V_{pl'kl}|^2 \frac{(n_{l'} - n_k)(n_{k-l'}^- + n_{-l})}{i\omega - (\mathcal{E}_k^\rho - \mathcal{E}_{l'}^{\sigma'} + \mathcal{E}_l^\sigma - \mu)} \\
& = \sum_{l'kl} |V_{pl'kl}|^2 \frac{(n_{l'} - n_k)n_{k-l'}^- + (n_{l'} - n_k)n_{-l}}{i\omega - (\mathcal{E}_k^\rho - \mathcal{E}_{l'}^{\sigma'} + \mathcal{E}_l^\sigma) + \mu} \\
& = \sum_{l'kl} |V_{pl'kl}|^2 \frac{n_{-l}n_k + (n_{l'} - n_k)n_{-l}}{i\omega - (\mathcal{E}_k^\rho - \mathcal{E}_{l'}^{\sigma'} + \mathcal{E}_l^\sigma) + \mu}.
\end{aligned} \tag{B.8}$$



---

## Localization of electronic states in hybrid nanoribbons in the nonperturbative regime

---

### C.1 Extracting site densities from QMC simulations

To extract the amplitudes for each site we first calculate site-dependent spatial correlators of the form

$$C_k(x, t) \equiv \langle a_x(t) a_k^\dagger(0) \rangle = \frac{1}{Z} \text{Tr} \left[ a_x(t) a_k^\dagger(0) e^{-\beta H} \right], \quad (\text{C.1})$$

where  $Z = \text{Tr} \left[ e^{-\beta H} \right]$  and the trace is taken over the entire Fock space of the system. Here  $x$  refers to a particular site on the lattice and  $k = (k_x, \kappa)$  is the momentum variable that corresponds to the state that we are interested in. The creation operator  $a_k^\dagger$  is

$$a_k^\dagger = \frac{1}{N_u} \sum_{x_u, i} e^{-ik_x x_u} C_i^\kappa a_{x_u, i}^\dagger, \quad (\text{C.2})$$

where the sum is over  $N_u$  locations of the unit cells located at positions  $x_u$  and the ions  $i$  within each unit cell. The coefficients  $C_i^\kappa$  are the non-interacting eigenvector components obtained from the diagonalization of the tight-binding Hamiltonian. For the low-energy localized state, we have that  $k_x = 0$  and choose  $\kappa$  to correspond to the (non-interacting) eigenvector corresponding to this localized state.

By expressing the time-dependence in the right-hand side of Eq. (C.1) in the Heisenberg picture,

$$a_x(t) = e^{-Ht} a_x e^{Ht},$$

we can perform a spectral decomposition and determine the leading dependence of this correlator in the large time limit. We find

$$\lim_{1 \ll t < \beta} C_k(x, t) = \langle \Omega | a_x | \Omega + k \rangle \langle \Omega + k | a_k^\dagger | \Omega \rangle e^{-(\varepsilon_{\Omega+k} - \varepsilon_\Omega)t} + \dots, \quad (\text{C.3})$$

where the ellipsis represents terms that are exponentially suppressed. The state  $|\Omega\rangle$  and its associated energy  $\varepsilon_\Omega$  represents the half-filling global ground state and global interacting energy minimum,

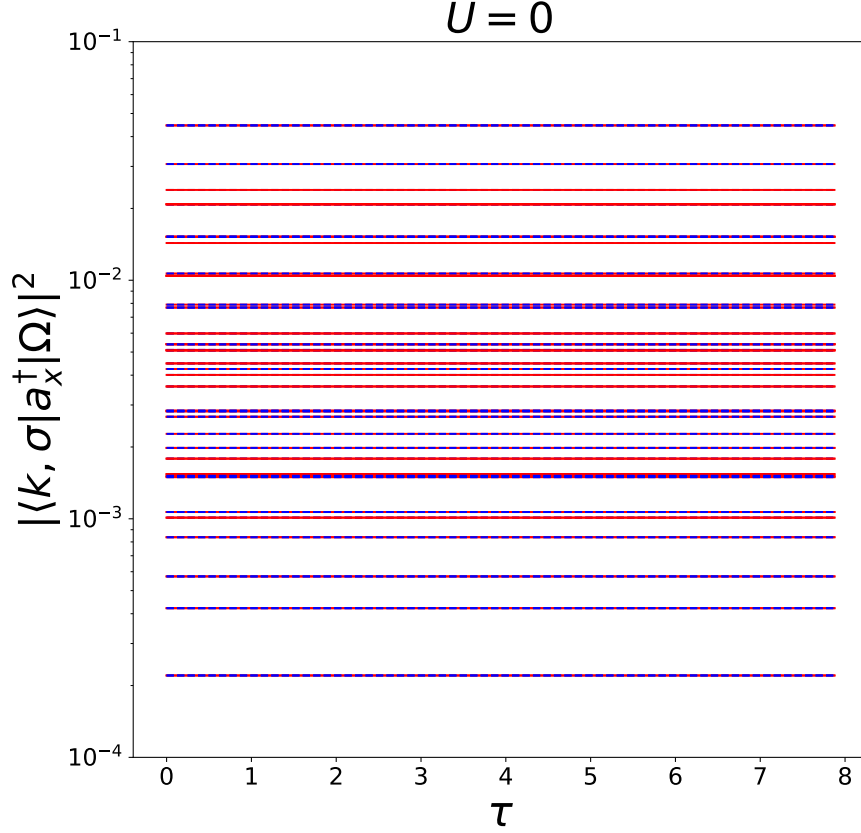


Figure C.1: Non-interacting wavefunction densities  $\rho_k(x, t)$  (labeled as  $|\langle k, \sigma | a_x^\dagger | \Omega \rangle|^2$  above) of the lowest energy localized state, as defined by Eq. (C.4). The different lines correspond to different lattice sites  $x$  and the red/blue coloring refer to A/B sites.

respectively, and the state  $|\Omega + k\rangle$  and associated energy  $\varepsilon_{\Omega+k}$  is the state with an additional fermion with momentum  $k$  above half filling and its corresponding interacting energy, respectively. The energy difference  $\varepsilon_{\Omega+k} - \varepsilon_{\Omega} \equiv E_k$  is exactly the interacting energy that we refer to in the manuscript.

The amplitude we are interested in is  $\langle \Omega | a_x | \Omega + k \rangle$ . Note that in the non-interacting limit we have that  $\langle \Omega + k | a_k^\dagger | \Omega \rangle = 1$  and the amplitude is, up to an overall phase, equivalent to  $C_i^k$  in Eq. (C.2). With interactions, unfortunately, we cannot extract this amplitude because it is multiplied by the factor  $\langle \Omega + k | a_k^\dagger | \Omega \rangle e^{-(E_{\Omega+k} - E_{\Omega})t}$  which we do not *a priori* know. However, note that this factor is *independent* of the site  $x$  and carries the same time dependence for all spatial correlators. Furthermore, we are interested in the densities,  $\rho_k(x) = |\langle \Omega | a_x | \Omega + k \rangle|^2$  which should be normalized over the lattice unit cell,  $\sum_x \rho_k(x) = 1$ . With these properties in mind, we instead analyze the following expression,

$$\rho_k(x, \tau) \equiv \frac{|C_k(x, \tau)|^2}{\sum_y |C_k(y, \tau)|^2}. \quad (\text{C.4})$$

Because of the independence of the unknown factor on spatial site  $x$  and its identical time dependence

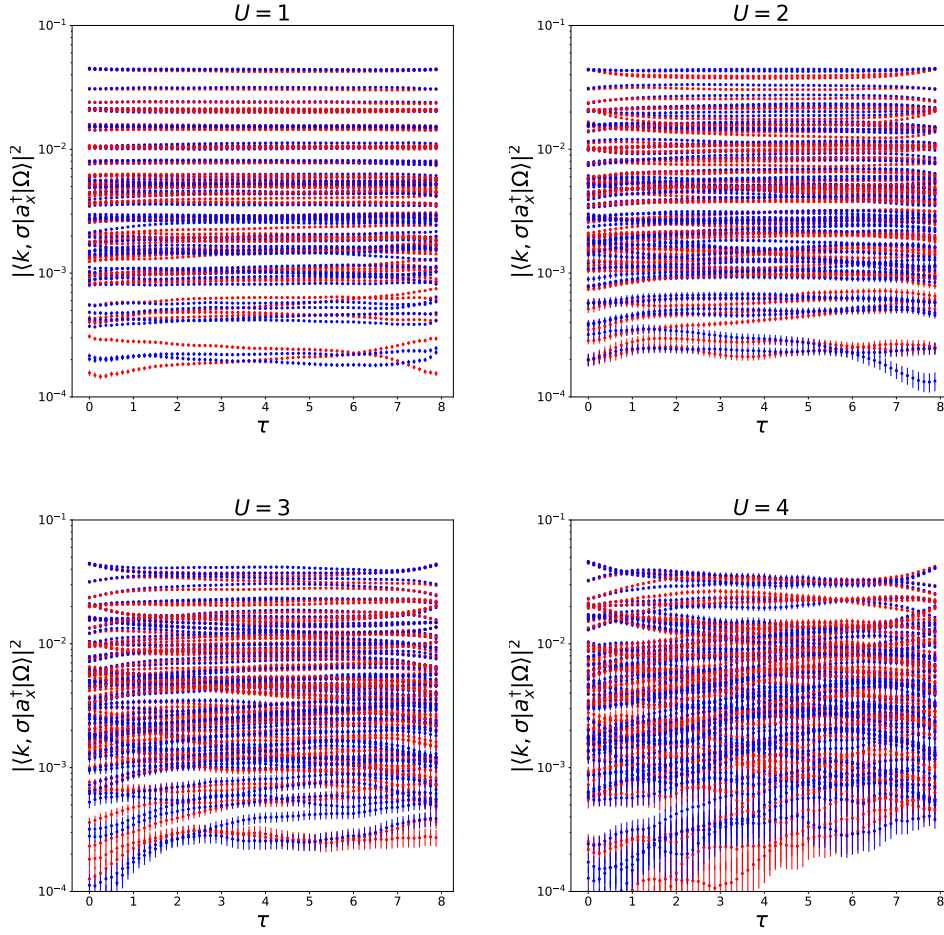


Figure C.2: Same as is in Fig. C.1, but now with non-zero values  $U$ . The non-interacting amplitudes at  $U = 0$  are shown in Fig. C.1.

for each spatial site, this factor cancels in this ratio. The resulting term is automatically normalized over all lattice sites and thus represents the density at each site  $x$ . In the non-interacting limit, the cancellation of the unknown factor occurs exactly for all  $\tau$ , and so Eq. (C.4) has no dependence on  $\tau$ . We have verified that it produces the exact wavefunction densities, as shown in Fig. C.1. For  $U \neq 0$ , the cancellation of the unknown factor occurs only in the scaling region given in Eq. (C.3), and so we extract the densities in the region where  $\rho_k(x, t)$  exhibits little to no time dependence and is thus relatively flat. Figure C.2 shows examples of the  $\rho_k(x, t)$  for different values of  $U$  including the non-interacting case. In all cases we extract the density in a region centered around  $t = \beta/2$ .



## Hubbard interaction at finite $T$ on a hexagonal lattice

### D.1 Results for $3 \times 3$ ribbons

We also examine a  $3 \times 3$  graphene sheet, which features three distinct correlators, labeled here as  $\Gamma$ ,  $K$  and  $A$ .  $K$  corresponds to the Dirac points where dispersion vanishes. Presence of the zero-energy state introduces a new type of behavior.  $K$  correlator itself is flat and starts at  $1/2$  instead of 1, whereas  $\Gamma$  correlator has a distinct plateau. This behavior is captured by the perturbative calculations, Fig. D.1. This was assumed to be an artifact in the simulations due to insufficient precision, however it seems that the plateau in the  $\Gamma$  correlator is indeed there. For  $U > 1$  we see a clear deviation between the plateaus of the HMC and perturbative correlators, however, the slopes of the correlators are approximated much better, despite the large values of the interaction strength.

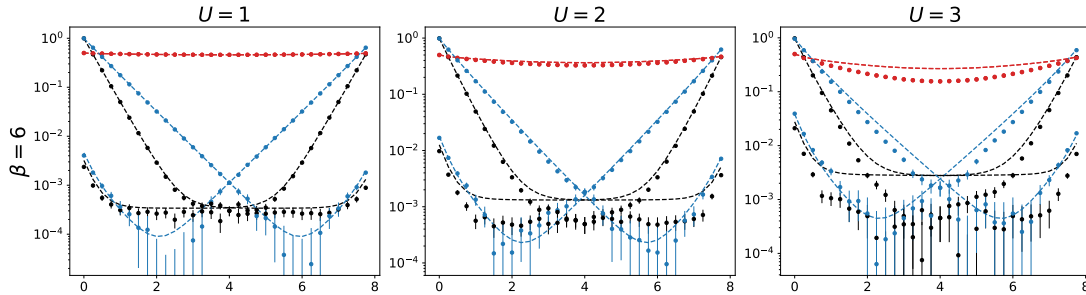


Figure D.1:  $C_k(\tau)$  vs.  $\tau$  for  $3 \times 3$  graphene at  $U = 1, 2,$  and  $3$  and  $\beta = 8$ . BZ of  $3 \times 3$  sheet contains *Dirac points*  $K, K'$  (red) where the dispersion vanishes. Corresponding correlator is “flat” and  $C_K(0) = 0.5$ .  $\Gamma$  (black) exhibits a plateau. The remaining correlator is labeled  $A$  (blue).



---

## Bibliography

---

- [1] L. Razmadze, *Topology and symmetry in carbon nanoribbons*, **PoS Regio2021** (2022) 031, URL: <https://doi.org/10.22323/1.412.0031> (cit. on pp. 1, 27, 89).
- [2] T. Luu, U.-G. Meißner and L. Razmadze, *Localization of electronic states in hybrid nanoribbons in the nonperturbative regime*, **Phys. Rev. B** **106** (19 2022) 195422, URL: <https://doi.org/10.1103/PhysRevB.106.195422> (cit. on pp. 1, 37, 61, 64, 72–74, 77, 89).
- [3] J. Ostmeyer, L. Razmadze, E. Berkowitz, T. Luu and U.-G. Meißner, *Effective theory for graphene nanoribbons with junctions*, **Phys. Rev. B** **109** (19 2024) 195135, URL: <https://doi.org/10.1103/PhysRevB.109.195135> (cit. on pp. 1, 59, 89).
- [4] L. Razmadze and T. Luu, *Hubbard interaction at finite  $T$  on a Hexagonal lattice*, **PoS LATTICE2024** (2024) 071, URL: <https://doi.org/10.22323/1.466.0071> (cit. on pp. 1, 16, 18, 79, 89).
- [5] A. Fetter and J. Walecka, *Quantum Theory of Many-Particle Systems*, Dover Books on Physics, Dover Publications, 2012, ISBN: 9780486134758, URL: [https://books.google.de/books?id=t5\\_DAgAAQBAJ](https://books.google.de/books?id=t5_DAgAAQBAJ) (cit. on pp. 11, 12, 17, 83, 85).
- [6] A. Abrikosov, L. Gorkov, I. Dzyaloshinski and R. Silverman, *Methods of Quantum Field Theory in Statistical Physics*, Dover Books on Physics, Dover Publications, 2012, ISBN: 9780486140155, URL: <https://books.google.de/books?id=JYTCAgAAQBAJ> (cit. on pp. 15, 16, 18, 84).
- [7] C. Gattringer and C. Lang, *Quantum Chromodynamics on the Lattice: An Introductory Presentation*, Lecture Notes in Physics, Springer Berlin Heidelberg, 2009, ISBN: 9783642018497, URL: <https://books.google.de/books?id=l2hZKnLYDxoC> (cit. on pp. 21, 43).
- [8] I. Omelyan, I. Mryglod and R. Folk, *Symplectic analytically integrable decomposition algorithms: classification, derivation, and application to molecular dynamics, quantum and celestial mechanics simulations*, **Computer Physics Communications** **151** (2003) 272, ISSN: 0010-4655, URL: <https://www.sciencedirect.com/science/article/pii/S0010465502007543> (cit. on p. 23).

- [9] A. Y. Kitaev, *Unpaired Majorana fermions in quantum wires*, *Uspekhi Fizicheskikh Nauk (UFN)* **44** (2001) 131, URL: <https://doi.org/10.1070/1063-7869/44/10s/s29> (cit. on p. 30).
- [10] Z. Chen, X. Li and T. K. Ng, *Exactly Solvable BCS-Hubbard Model in Arbitrary Dimensions*, *Phys. Rev. Lett.* **120** (4 2018) 046401, URL: <https://link.aps.org/doi/10.1103/PhysRevLett.120.046401> (cit. on p. 31).
- [11] M. Ezawa, *Exact solutions for two-dimensional topological superconductors: Hubbard interaction induced spontaneous symmetry breaking*, *Phys. Rev. B* **97** (24 2018) 241113, URL: <https://link.aps.org/doi/10.1103/PhysRevB.97.241113> (cit. on p. 31).
- [12] J.-J. Miao, D.-H. Xu, L. Zhang and F.-C. Zhang, *Exact solution to the Haldane-BCS-Hubbard model along the symmetric lines: Interaction-induced topological phase transition*, *Phys. Rev. B* **99** (24 2019) 245154, URL: <https://link.aps.org/doi/10.1103/PhysRevB.99.245154> (cit. on pp. 31, 32).
- [13] C. L. Kane and E. J. Mele, *Z<sub>2</sub> Topological Order and the Quantum Spin Hall Effect*, *Physical Review Letters* **95** (2005), URL: <http://dx.doi.org/10.1103/PhysRevLett.95.146802> (cit. on p. 36).
- [14] T. N. Katsunori Wakabayashi Ken-ichi Sasaki and T. Enoki, *Electronic states of graphene nanoribbons and analytical solutions*, *Science and Technology of Advanced Materials* **11** (2010) 054504, PMID: 27877361, eprint: <https://doi.org/10.1088/1468-6996/11/5/054504>, URL: <https://doi.org/10.1088/1468-6996/11/5/054504> (cit. on pp. 38, 39, 61, 63).
- [15] T. Cao, F. Zhao and S. G. Louie, *Topological Phases in Graphene Nanoribbons: Junction States, Spin Centers, and Quantum Spin Chains*, *Phys. Rev. Lett.* **119** (7 2017) 076401, URL: <https://link.aps.org/doi/10.1103/PhysRevLett.119.076401> (cit. on pp. 38–40, 60, 61, 63–65, 67, 68, 76, 77).
- [16] D. J. Rizzo et al., *Topological band engineering of graphene nanoribbons*, *Nature* **560** (7717 2018) 204, URL: <https://doi.org/10.1038/s41586-018-0376-8> (cit. on pp. 39, 40, 61, 64, 77).
- [17] O. Gröning et al., *Engineering of robust topological quantum phases in graphene nanoribbons*, *Nature* **560** (2018) 209, URL: <https://doi.org/10.1038/s41586-018-0375-9> (cit. on pp. 39, 40, 61, 64).
- [18] D. J. Rizzo et al., *Rationally Designed Topological Quantum Dots in Bottom-Up Graphene Nanoribbons*, *ACS Nano* **15** (2021) 20633, PMID: 34842409, eprint: <https://doi.org/10.1021/acsnano.1c09503>, URL: <https://doi.org/10.1021/acsnano.1c09503> (cit. on pp. 39, 61, 77).
- [19] M. Ezawa, *Exact solutions for two-dimensional topological superconductors: Hubbard interaction induced spontaneous symmetry breaking*, *Phys. Rev. B* **97** (24 2018) 241113, URL: <https://link.aps.org/doi/10.1103/PhysRevB.97.241113> (cit. on pp. 39, 48, 49, 61).

- 
- [20] S.-R. E. Yang, M.-C. Cha, H. J. Lee and Y. H. Kim, *Topologically ordered zigzag nanoribbon:  $e/2$  fractional edge charge, spin-charge separation, and ground-state degeneracy*, *Phys. Rev. Res.* **2** (3 2020) 033109, URL: <https://link.aps.org/doi/10.1103/PhysRevResearch.2.033109> (cit. on pp. 39, 48, 61).
- [21] J.-J. Miao, D.-H. Xu, L. Zhang and F.-C. Zhang, *Exact solution to the Haldane-BCS-Hubbard model along the symmetric lines: Interaction-induced topological phase transition*, *Phys. Rev. B* **99** (24 2019) 245154, URL: <https://link.aps.org/doi/10.1103/PhysRevB.99.245154> (cit. on pp. 39, 48).
- [22] D. B. Kaplan, *A method for simulating chiral fermions on the lattice*, *Physics Letters B* **288** (1992) 342, URL: <https://www.sciencedirect.com/science/article/pii/037026939291112M> (cit. on pp. 40, 54).
- [23] Y. Shamir, *Chiral fermions from lattice boundaries*, *Nuclear Physics B* **406** (1993) 90, URL: <https://www.sciencedirect.com/science/article/pii/055032139390162I> (cit. on p. 40).
- [24] J.-W. Rhim, J. Behrends and J. H. Bardarson, *Bulk-boundary correspondence from the intercellular Zak phase*, *Phys. Rev. B* **95** (3 2017) 035421, URL: <https://link.aps.org/doi/10.1103/PhysRevB.95.035421> (cit. on pp. 40, 64).
- [25] R. Kundu, *Tight-binding Parameters for Graphene*, *Modern Physics Letters B* **25** (2011) 163, URL: <https://doi.org/10.1142/S0217984911025663> (cit. on pp. 40, 63).
- [26] T. Luu and T. A. Lähde, *Quantum Monte Carlo calculations for carbon nanotubes*, *Phys. Rev. B* **93** (15 2016) 155106, URL: <https://link.aps.org/doi/10.1103/PhysRevB.93.155106> (cit. on p. 43).
- [27] J. Ostmeyer et al., *Semimetal–Mott insulator quantum phase transition of the Hubbard model on the honeycomb lattice*, *Phys. Rev. B* **102** (24 2020) 245105, URL: <https://link.aps.org/doi/10.1103/PhysRevB.102.245105> (cit. on pp. 43, 81).
- [28] J. Ostmeyer et al., *Antiferromagnetic character of the quantum phase transition in the Hubbard model on the honeycomb lattice*, *Phys. Rev. B* **104** (15 2021) 155142, URL: <https://link.aps.org/doi/10.1103/PhysRevB.104.155142> (cit. on pp. 43, 86).
- [29] N. N. Bogoljubov, *On a new method in the theory of superconductivity*, *Nuovo Cim.* **7** (6 1958) 794, URL: <https://doi.org/10.1007/BF02745585> (cit. on pp. 49, 75).
- [30] J. G. Valatin, *Comments on the theory of superconductivity*, *Il Nuovo Cimento* (1955-1965) **7** (6 1958) 843, URL: <https://doi.org/10.1007/BF02745589> (cit. on p. 49).
- [31] Z. Chen, X. Li and T. K. Ng, *Exactly Solvable BCS-Hubbard Model in Arbitrary Dimensions*, *Phys. Rev. Lett.* **120** (4 2018) 046401, URL: <https://link.aps.org/doi/10.1103/PhysRevLett.120.046401> (cit. on p. 49).

- [32] H. Nielsen and M. Ninomiya, *A no-go theorem for regularizing chiral fermions*, *Physics Letters B* **105** (1981) 219, URL: <https://www.sciencedirect.com/science/article/pii/0370269381910261> (cit. on p. 54).
- [33] G. W. Semenoff, *Condensed-Matter Simulation of a Three-Dimensional Anomaly*, *Phys. Rev. Lett.* **53** (26 1984) 2449, URL: <https://link.aps.org/doi/10.1103/PhysRevLett.53.2449> (cit. on pp. 54, 55).
- [34] G. W. Semenoff, *Chiral symmetry breaking in graphene*, *Physica Scripta* **2012** (2012) 014016, URL: <https://dx.doi.org/10.1088/0031-8949/2012/T146/014016> (cit. on p. 54).
- [35] B. A. Bernevig, *Topological Insulators and Topological Superconductors*, Princeton: Princeton University Press, 2013, ISBN: 9781400846733, URL: <https://doi.org/10.1515/9781400846733> (cit. on p. 54).
- [36] T. Stanescu, *Introduction to Topological Quantum Matter & Quantum Computation*, Boca Raton: CRC Press, 2016, URL: <https://doi.org/10.1201/9781315181509> (cit. on p. 54).
- [37] D. Smith and L. von Smekal, *Monte Carlo simulation of the tight-binding model of graphene with partially screened Coulomb interactions*, *Phys. Rev. B* **89** (19 2014) 195429, URL: <https://link.aps.org/doi/10.1103/PhysRevB.89.195429> (cit. on pp. 55, 86).
- [38] I. H. Lee, H. A. Le and S. -. E. Yang, *Mutual information and correlations across topological phase transitions in topologically ordered graphene zigzag nanoribbons*, 2023, arXiv: 2310.08970 [cond-mat.str-el] (cit. on p. 61).
- [39] A. Honet, L. Henrard and V. Meunier, *Robust correlated magnetic moments in end-modified graphene nanoribbons*, 2023, arXiv: 2310.09057 [cond-mat.mes-hall] (cit. on p. 61).
- [40] H. C. Lee and S. -. E. Yang, *Chiral symmetry breaking and topological charge of graphene nanoribbons*, 2023, arXiv: 2312.05487 [cond-mat.mes-hall] (cit. on p. 61).
- [41] P. R. Wallace, *The Band Theory of Graphite*, *Phys. Rev.* **71** (9 1947) 622 (cit. on p. 63).
- [42] C. R. Group, *Topological Engineering of GNRs*, 2023, URL: <https://crommie.berkeley.edu/research/syngnr/topeng/> (cit. on p. 77).
- [43] M. Le Bellac, *Thermal Field Theory*, Cambridge Monographs on Mathematical Physics, Cambridge University Press, 1996 (cit. on p. 81).
- [44] J. I. Kapusta and C. Gale, *Contents*, Cambridge Monographs on Mathematical Physics, Cambridge University Press, 2023 v (cit. on p. 81).
- [45] A. H. Castro Neto, F. Guinea, N. M. R. Peres, K. S. Novoselov and A. K. Geim, *The electronic properties of graphene*, *Rev. Mod. Phys.* **81** (1 2009) 109, URL: <https://link.aps.org/doi/10.1103/RevModPhys.81.109> (cit. on p. 81).

- 
- [46] R. Scalettar, “Quantum Materials: Experiments and Theory”, ed. by E. Pavarini, E. Koch, J. van den Brink and G. Sawatzky, vol. 6, Schriften des Forschungszentrums Jülich. Reihe modeling and simulation, Jülich: Forschungszentrum Jülich GmbH Zentralbibliothek, Verlag, 2016, chap. An Introduction to the Hubbard Hamiltonian 420 S. ISBN: 978-3-95806-159-0, URL: <https://juser.fz-juelich.de/record/819465> (cit. on p. 86).
- [47] M. V. Ulybyshev, P. V. Buividovich, M. I. Katsnelson and M. I. Polikarpov, *Monte Carlo Study of the Semimetal-Insulator Phase Transition in Monolayer Graphene with a Realistic Interelectron Interaction Potential*, *Phys. Rev. Lett.* **111** (5 2013) 056801, URL: <https://link.aps.org/doi/10.1103/PhysRevLett.111.056801> (cit. on p. 86).